STUDIES OF THE FLUX FLOW RESISTIVITY IN $YBa_2Cu_3O_{6.95}$ BY MICROWAVE TECHNIQUES

By

David Craig Morgan

M.Sc. (Physics), University of British Columbia

B.Sc. (Physics), University of Waterloo

A THESIS SUBMITTED IN PARTIAL FULFILLMENT OF

THE REQUIREMENTS FOR THE DEGREE OF

DOCTOR OF PHILOSOPHY

in

THE FACULTY OF GRADUATE STUDIES

PHYSICS

We accept this thesis as conforming

to the required standard

In presenting this thesis in partial fulfilment of the requirements for an advanced degree at the University of British Columbia, I agree that the Library shall make it freely available for reference and study. I further agree that permission for extensive copying of this thesis for scholarly purposes may be granted by the head of my department or by his or her representatives. It is understood that copying or publication of this thesis for financial gain shall not be allowed without my written permission.

(Signature

Department of __Physics__

The University of British Columbia
Vancouver, Canada

Date __December 21st, 1993.__

Abstract

Measurements of the microwave surface resistance at 5.4, 27 and 35 GHz on a high quality single crystal of $YBa_2Cu_3O_{6.95}$ in magnetic fields up to 8T (applied parallel to the c-axis) and at temperatures from 20K to 100K are presented. The Coffey-Clem expression for the surface impedance of a superconductor in the mixed state is used to fit the data in terms of a pinning frequency and a free flux flow resistivity (thermal hopping of vortices is not included since it is not important for $YBa_2Cu_3O_{6.95}$ at microwave frequencies). A temperature dependent pinning frequency is found that varies from ~ 20 GHz at 20K to effectively zero by 80K. The flux flow resistivity is strongly temperature dependent and consistent, down to at least 50K, with the Bardeen-Stephen expression $\rho_{ff}/\rho_n(T) = H/H_{c_2}(T)$ if an extrapolation of the linear normal state resistivity from above T_c is used for $\rho_n(T)$. This suggests that the traditional picture of a vortex core as a cylinder of normal material may be valid in these materials. In contrast, the normal fluid quasiparticle scattering rate, as determined by zero field microwave measurements on the same single crystals[1], drops precipitously below T_c and, thus, is probably not the relevant scattering rate for the charge carriers in the vortex core.

---

[1]D.A. Bonn et al. Phys. Rev. Lett., **68**:2390, 1992.

Table of Contents

List of Figures

Acknowledgements

Lastly, I'd like to thank Mary Flesher whose love and support I not only cherish but have been able to count on during the course of this Ph.D. project.

Notation

h Plank's constant

e charge of electron

k_B Boltzmann's constant

Φ_0 flux quantum

ω angular frequency of rf fields

m mass of the charge carriers

m_v inertial mass associated with the vortex

$\mathbf{J}$ current density

$\mathbf{J}_n$ normal fluid current density

$\mathbf{J}_s$ superfluid current density

$\mathbf{J}_T$ transport current density

$\mathbf{E}$ electric field

$\mathbf{B}$ magnetic induction

$\mathbf{H}$ magnetic field

H_c thermodynamic critical field

H_{c_1} lower critical field

H_{c_2} upper critical field

l mean free path

ξ_c coherence length in the c-direction

$\xi_{ab} = \xi$ a-b plane coherence length

λ_L London penetration depth

λ penetration depth in a dirty superconductor

$\tilde{\lambda}$ complex penetration depth

δ_n normal state skin depth

T_c superconducting transition temperature

Δ superconducting energy gap

E_F Fermi energy

v_F Fermi velocity

$|\psi|^2$ superconducting order parameter

n_s density of superconducting electrons

x_n normal fluid fraction

Z_s surface impedance

R_s surface resistance

X_s surface reactance

Q qualityfactor

f_0 resonant frequency

$\tilde{\sigma}$ complex conductivity

σ_1 real part of the complex conductivity

σ_2 absolute value of the imaginary part of the conductivity

n number of vortices per unit area

ρ_n resistivity associated transport due to normal carriers

ρ_{ff} flux flow resistivity

η vortex viscosity

f_p/ω_p linear/angular pinning frequency

κ_p pinning force constant

τ scattering time

$\mathbf{v_L}$ vortex velocity

$\mathbf{v_c}$ velocity of charge carriers in the core of the vortex

$\mathbf{v_T}$ velocity of charge carriers in superfluid transport current

$\mathbf{v_s}$ velocity of charge carriers in the superfluid circulating the vortex

P power dissipated per unit volume

W power dissipated per unit length

U_0 barrier height of pinning potential

α coefficient of magnus force term in the vortex equation of motion

θ_H Hall angle

ω_c cyclotron frequency

Chapter 1

Introduction

In the 1960's, during dc transport measurements on conventional type-II superconductors in a magnetic field[1], it was observed that for current densities greater than a so-called depinning critical current density, a finite resistance to current flow developed. Indeed, above this critical current density, the I-V characteristics took on an ohmic character. This finite resistance was attributed to viscous flow of vortices and the slope of the I-V curve was used to define a flux flow resistivity, ρ_{ff} . The superconductor was thus acting like a normal metal with a resistivity given by ρ_{ff} instead of the usual resistivity of a normal metal (which at the low temperatures associated with conventional superconductors would be the temperature independent impurity limited value). The basic picture of the process was that the vortices move in response to a Lorentz force per unit length, $\mathbf{J} \times \Phi_0$, where $\mathbf{J}$ is the transport current density and Φ_0 the magnetic flux quantum that threads through the vortex. The vortices remain immobile until this force exceeds the pinning force (typically due to defects that act to pin the vortices at particular locations). Once they start to move, an electric field is induced along the direction of the applied current causing power dissipation and a finite resistance.

It was postulated that the vortices are subject to a viscous retarding force per unit length, $\mathbf{F} = -\eta \mathbf{v_L}$, where $\mathbf{v_L}$ is the vortex velocity and η a vortex viscosity. It was found from dc transport measurements on a number of superconducting alloys[1, 2, 3] that for low temperatures and magnetic fields the flux flow resistivity obeys a law of

1

corresponding states

$$\frac{\rho_{ff}}{\rho_n} = \frac{H}{H_{c_2}} \tag{1.1}$$

although there there seems to be some confusion as to whether the H_{c_2} factor in the denominator on the RHS should be $H_{c_2}(0)$ or $H_{c_2}(T)$. The flux-flow resistivity was also found to determine the energy dissipation at microwave frequencies[4, 5, 6, 7, 8] even for current densities much less than the depinning critical current densities at dc. The power absorbed was found to exhibit a crossover[4, 5] as a function of frequency from a low dissipation regime at low frequency to a regime at high frequency where the superconductor effectively behaves like a metal with resistivity given by ρ_{ff} . The crossover was characterized by a so-called pinning frequency, f_p, the magnitude of which was typically in the 10 MHz range. Thus the microwave surface resistance could be used to extract the flux flow resistivity and the results were also found to be consistent with equation 1.1 (with $H_{c_2}(0)$ in the denominator) for low temperatures and fields.

Equation 1.1 also comes out of a theory developed by Bardeen and Stephen[9] who calculated the dissipation in the clean limit (mean free path much greater than the coherence length, $l > \xi$) and at zero temperature, to a vortex moving in response to a Lorentz force per unit length, $\mathbf{J} \times \Phi_0$, and retarded by a viscous force per unit length, $-\eta \mathbf{v_L}$. They modelled the vortex in terms of two components: a totally normal core of radius the coherence length, ξ, and a transition region where the order parameter changes over a length scale ξ from zero at the core boundary to its equilibrium value in the bulk of the superconductor. They also found that close to T_c ,

$$\frac{\rho_{ff}}{\rho_n} = \frac{H}{H_{c_2}(T)} \tag{1.2}$$

More rigorous calculations based on time dependent Ginzburg-Landau theory[10, 11, 12, 13, 14, 15] were able to obtain solutions for ρ_{ff} but only in certain limits. In the dirty limit and for $T \ll T_c$ and $H \ll H_{c_2}$ an expression close to equation 1.1 was obtained[16].

One of the interesting aspects of the flux-flow resistivity is that it provides information about the scattering rate of the normal quasiparticles in the core of the vortex. In conventional superconductors, the quasiparticle scattering rate is temperature independent and the same in the normal core as it is in the bulk superconductor. In the high-T_c superconductor, $YBa_2Cu_3O_{6.95}$, the normal state resistivity is strikingly linear over a large temperature range above T_c until the pronounced rounding that occurs due to two dimensional fluctuations near the superconducting transition[17]. Thus the scattering rate of the charge carriers is temperature dependent at T_c and not temperature independent as it is for conventional superconductors. Moreover, the scattering rate for the quasiparticles in the normal fluid in zero field has been observed to drop rapidly as a function of temperature below T_c [18, 19]. However, it is not obvious whether or not this scattering rate is the relevant one for the charge carriers in the core of the vortex. If we retain the picture of a normal core, it is tempting to extrapolate the linearly decreasing scattering rate of the charge carriers from above T_c down to low temperatures. The Bardeen-Stephen[9] picture of moving vortices has a contribution to the dissipation from the transition region outside the completely normal core equal to the one from the normal core itself. This raises the possibility that both of the above scattering rates might be relevant in determining the flux flow resistivity. In addition, the Hall angle, θ_H, in the mixed state is intimately bound up with the lifetime of the quasiparticles in the cores[9, 20]. Due to strong pinning, θ_H in $YBa_2Cu_3O_{6.95}$ has not been measured below about 70K. Thus a possible effect on the measurement of ρ_{ff} due to a non-negligible Hall effect must be kept in mind.

The situation is made more complicated by the possibility that the picture of a cylinder of normal material may not be a very good approximation for vortex cores in high-T_c superconductors. The basis for the idea of a normal core in conventional superconductors (apart from the fact that the order parameter goes to zero at the centre of the core) was

the demonstration that there is a set of low-lying closely spaced energy levels localized in the vortex core that is comparable to a cylinder of normal metal of radius ξ[21]. The level spacing is of order Δ^2/E_F where Δ is the energy gap and E_F the Fermi energy. For low-T_c superconductors, this spacing is $\sim$ 1mK whereas for high-T_c materials it is estimated to be $\sim$10K or more[22, 23]. Thus there is the possibility of the discrete nature of the energy level spectrum playing a role.

Another layer of complexity has become apparent with the growing body of evidence for an unconventional pairing state in the high-T_c superconductors[24]. A possible candidate is d-wave pairing and the effect of such a state, whose gap function has line nodes on the Fermi surface, on the models of vortex motion is unclear. It is thus important to retain a broad view of flux flow resistivity measurements since it is unlikely, given the current state of uncertainty as to the underlying mechanisms involved, that we will be able to arrive at a definitive understanding of flux flow.

The microwave technique is especially helpful in trying to measure the flux flow resistivity of $YBa_2Cu_3O_{6.95}$ because of the very strong pinning of vortices in this material. Extremely high current densities are required to exceed the depinning critical current density. Practically speaking, this limits the dc technique to only a 10–15K temperature range below T_c and, even here, very large current densities ($\sim 10^6 A/cm^2$) are required[25]. Also, to measure ρ_n directly by applying a magnetic field greater than H_{c_2} is only possible close to T_c because of the large H_{c_2} 's in $YBa_2Cu_3O_{6.95}$ (H_{c_2} (0) is estimated to be $\sim$120T[26]). Such strong pinning means that the pinning or crossover frequency might be much higher than that observed for conventional superconductors. We cannot assume, therefore, that frequencies in the range 5–35 GHz will be in the high frequency, flux flow limit. In addition, due to the higher temperature scale associated with high-T_c materials, thermally activated vortex motion[27] plays a more prominent role than in the vortex dynamics of conventional superconductors, although later, we will

argue that for $YBa_2Cu_3O_{6.95}$ at our frequencies, the dynamics are not contaminated by this latter effect.

We will rely mainly on a model derived by Coffey and Clem[28, 29] (but in the limit of no thermally activated flux motion) to fit our microwave data. In this limit their expression for the surface impedance is just a slight generalization of the one used[4, 5] to extract ρ_{ff} in the microwave experiments on conventional superconductors. It should be made clear from the outset that the use of this model in no way assumes a temperature or field dependence of the flux flow resistivity. It is a vehicle to get from the surface resistance data to the flux flow resistivity: we use it to fit the data at three different frequencies (5.4, 27 and 35 GHz) in terms of a vortex viscosity and a pinning frequency. We are principally interested in the viscosity since this gives ρ_{ff} directly; the fit to the pinning frequency removes pinning effects that otherwise might be attributed to the field or temperature dependence of ρ_{ff} . With only three frequencies, we are not able to unequivocally demonstrate the existence of the high frequency, flux flow limit. However, fitting to the Coffey-Clem model shows that the data is consistent with a temperature dependent pinning frequency that is $\sim$20 GHz at 20K and that decreases to zero by $\sim$80K. Thus we believe that the vortex viscosity and flux flow resistivity that we extract from the surface resistance is independent of the effects of pinning. We find a flux flow resistivity that decreases rapidly below T_c and is reasonably well described down to about 50K by

$$\frac{\rho_{ff}}{\rho_n(T)} = \frac{H}{H_{c_2}(T)} \qquad (1.3)$$

where $\rho_n(T)$ is given by the extrapolation of the linear dc resistivity from above T_c and H_{c_2} (T) is given by an estimate based on the measured slope of H_{c_2} (T) near T_c . Below 50K, the extracted ρ_{ff} is higher than what we would have expected from the above equation.

To our knowledge, this is one of the only measurements of the flux flow resistivity down to lower temperatures in high quality single crystals of $YBa_2Cu_3O_{6.95}$. We will discuss some of the possible implications of these measurements but must ultimately leave the questions open until there is a better understanding of vortex motion in the high-T_c superconductors.

Chapter 2

Introduction to $YBa_2Cu_3O_{7-\delta}$

In this chapter, we will introduce some of the essential features of high-T_c superconductors, specifically $YBa_2Cu_3O_{7-\delta}$. It is not meant as a comprehensive review of the current state of research in the field. Rather, it is meant to set the context for the main topic of this thesis: the free flux-flow resistivity in the mixed state.

Before embarking on this discussion, we should briefly mention a matter of convention. The units used in this thesis will be MKS. However, there has been a strong tradition in the literature of using cgs to discuss theory and experiments concerning superconductivity. In particular, the terminology of H_c, H_{c_1} and H_{c_2} as referring to the critical fields instead of B_c, etc. is deeply ingrained. To adhere to this convention while still maintaining consistency with MKS units, we adopt the following compromise: in a general discussion of, say, the upper critical field we use, H_{c_2} , but in formulae we insert the appropriate factors of μ_0; the reader can take for granted that, in this thesis, B can always be obtained from H simply by multiplying by μ_0.

2.1 Some basic features

One of the most basic features of high-T_c superconductors is their anisotropy: conduction occurs primarily in two dimensional CuO_2 layers which are weakly coupled together. We can imagine the superconductor as a stack of such layers in what we label, conventionally, as the c-direction; the CuO_2 layers lie correspondingly in the a-b plane. Figure 2.1 shows the dc electrical resistivity in the a-b plane as a function of temperature measured by

Baar et al[17] on high quality single crystals of YBa$_2$Cu$_3$O$_{6.95}$ made at U.B.C. by Liang et al[30]. ρ_c has also been measured on these crystals and shows the same T_c but has an overall magnitude about fifty times greater than ρ_{ab} and exhibits a slight upturn before T_c - this thesis deals almost exclusively with a-b plane currents and so c-axis transport will not be discussed further. The superconducting transition at $\sim$93K is dramatically evident — T_c's of up to 93.4K have been observed in these crystals.

There are two other features of interest. First is the striking linearity of the resistivity in the normal state above about 120K and that it extrapolates to very close to zero at zero temperature. The Debye temperature in YBa$_2$Cu$_3$O$_{7-\delta}$ is estimated to be $\sim$ 400K[31] and so a linear resistivity in this temperature range is highly anomalous. Indeed, this linear resistivity is a powerful constraint on theories that try to explain high-T_c superconductors. The other interesting feature of the resistive transition is the pronounced rounding starting at about 120K. This rounding has been interpreted in terms of fluctuations associated with the two-dimensional nature of the material. The large temperature range above T_c where these fluctuation effects are observable is characteristic of the CuO$_2$ superconductors. The usual fluctuations associated with deviations from mean field theory near the transition would only be expected to play a role within $\sim$1K of T_c .

Estimates of the coherence lengths in YBa$_2$Cu$_3$O$_{7-\delta}$ can be made by magnetization measurements close to T_c . Welp et al[26] performed such measurements on single crystals of YBa$_2$Cu$_3$O$_{7-\delta}$ down to about 8K below the transition and found their data consistent with a linear dependence of H_{c_2} on temperature with $\mu_0 dH_{c_2}/dT |_{T_c}$ being -1.9T/K and -10.5T/K for the field oriented parallel and perpendicular to the c-axis respectively. They use the Werthamer-Helfand-Hohenberg formula[32, 33]

$$H_{c_2}(0) = 0.7 \left(\frac{\partial H_{c_2}}{\partial T} \right)\Bigg|_{T_c} T_c \qquad (2.1)$$
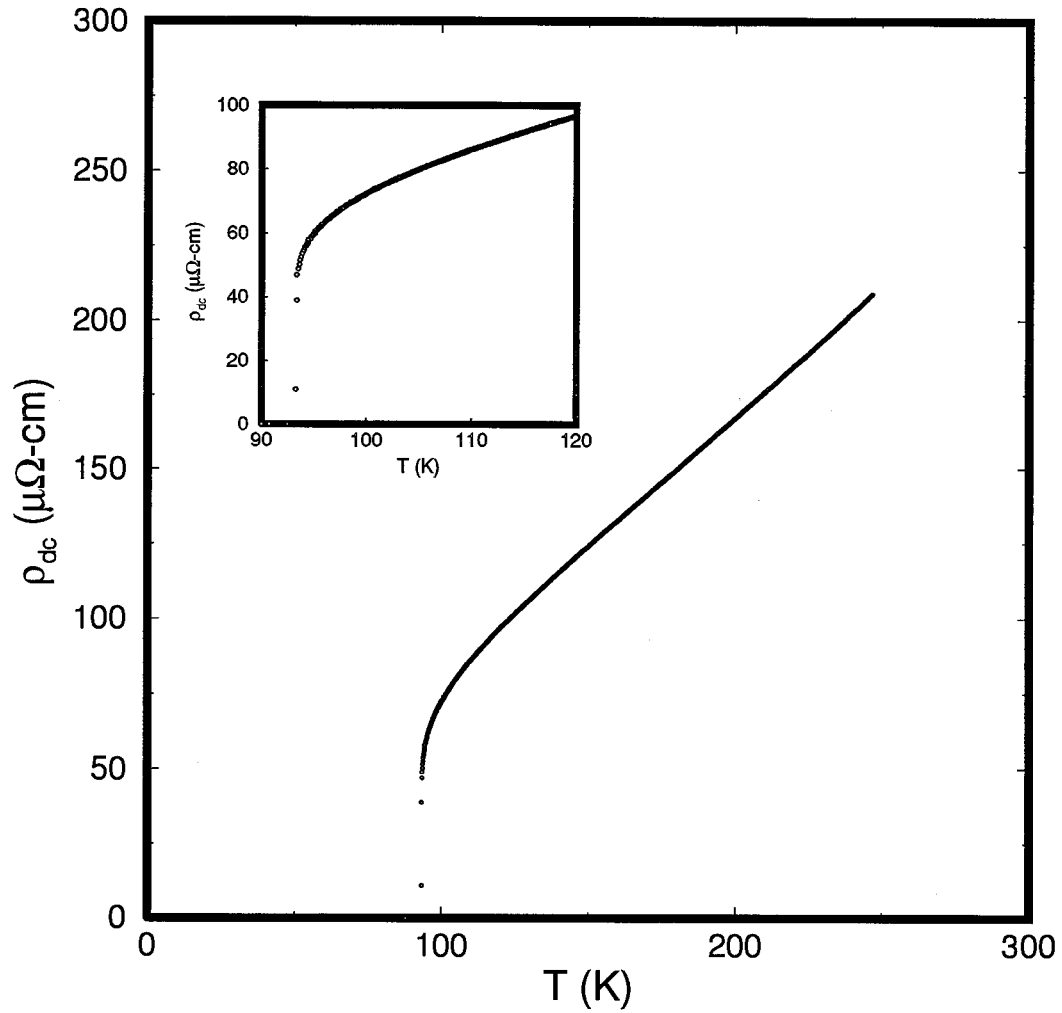
Figure 2.1: Temperature dependence of the a-b plane dc resistivity of YBa$_2$Cu$_3$O$_{6.95}$. Inset: a close-up of the transition. This measurement was made by Baar et al[17] on the U.B.C. single crystals (Liang et al[30]).

to obtain estimates of $\mu_0 H_{c_2}{}^c(0) = 122$T (field parallel to the c-axis) and $\mu_0 H_{c_2}{}^{ab}(0) = 674$T (field parallel to the a-b plane). An empirical formula consistent with $\mu_0 dH_{c_2}/dT \mid_{T_c}$ being -1.9T/K and $H_{c_2}(0)$ being 125T is given by

$$\mu_0 H_{c_2}(T) = 125 \frac{(1 - t^2)}{(1 + t^2)^{1/2}} ,$$
(2.2)

$(t = T/T_c)$ and we will use it for the temperature dependence of $\mu_0 H_{c_2}{}^{ab}(T)$ throughout this thesis. Using the formulae[34]

$$\mu_0 H_{c_2}{}^c = \frac{\Phi_0}{2\pi \xi_{ab}^2} \; ; \; \mu_0 H_{c_2}{}^{ab} = \frac{\Phi_0}{2\pi \xi_c^2}$$
(2.3)

an a-b plane coherence length, ξ_{ab}, of 16.4 Å and a c-axis coherence length, ξ_c, of 3.0Å can be found. Both ξ_c and ξ_{ab} are considerably shorter than the coherence lengths associated with conventional superconductors. In this thesis, we are concerned principally with ξ_{ab}, and so we set $\xi = \xi_{ab}$ for convenience.

The zero temperature value of the London penetration depth, $\lambda_L(0)$, is also of great interest. However, considerable debate still exists about its correct value. Callin and Berlinsky[24] have reviewed and evaluated the experiments that claim to measure this quantity and we follow their discussion here. Typically, microwave experiments measure only the change in the penetration depth and not its absolute value. Nevertheless, Pond et al[35] used a transmission line resonator consisting of a 2000Å thick YBa$_2$Cu$_3$O$_{7-\delta}$ layer and found $\lambda_L(0) = 1300\mathring{A}$; however, they have had difficulty in reproducing the measurement. Muon spin resonance is a bulk probe that measures the distribution of magnetic fields in the mixed state. This can be related to the penetration depth via Ginzburg-Landau theory. Estimates of $\lambda_L(0)$ from this technique on the U.B.C. single crystals give 1400Å although there is still some field and sample dependence in the data. Infrared measurements can also be used to obtain a value for $\lambda_L(0)$. Since the complex

conductivity for frequencies well below the gap is given by

$$\tilde{\sigma} = \sigma_1 - \frac{i}{\mu_0 \, \omega \, \lambda_L{}^2} \qquad (2.4)$$

λ_L can be obtained by measuring the coefficient of the $1/\omega$ divergence in the imaginary part of the conductivity as $\omega \to 0$. It is also possible to measure the missing oscillator strength in $\sigma_1(\omega)$ from above to below T_c to determine λ_L[34]. These two methods were found to give the same value for λ_L. Basov et al[36] found a value of 1440Å for the YBa$_2$Cu$_3$O$_{6.95}$ single crystals from U.B.C. . Measurements of the lower critical field can also be used to obtain a value for λ_L through the expression

$$H_{c_1} = \frac{\Phi_0}{4 \, \pi \, \lambda_L{}^2} \, ln \left(\frac{\lambda_L}{\xi} \right) . \qquad (2.5)$$

Umezawa et al[37] obtained values in the range 900–950Å while Liang et al[38] obtained $\sim 800\mathring{A}$ (on U.B.C. crystals). The significant difference between these numbers and the values obtained using other techniques has not yet been explained.

Clearly YBa$_2$Cu$_3$O$_{7-\delta}$ is an extreme type-II superconductor with $\kappa = \lambda_L/\xi \sim 70$–80 and therefore a system in which a local treatment of the electrodynamics makes sense. Thus, the two London equations

$$\mathbf{E} = \mu_0 \, \lambda_L{}^2 \, \frac{\partial \mathbf{J_s}}{\partial t} \qquad (2.6)$$

and

$$\mathbf{H} = - \, \lambda_L{}^2 \, \nabla \times \mathbf{J_s} \qquad (2.7)$$

might be expected to do a reasonable job of describing the electrodynamics. We should also note that because the coherence lengths are so small, we are almost certainly in the clean limit ($l > \xi$).

Given the linear nature of the temperature dependence of the scattering rate of the charge carriers above T_c , it is natural to wonder about the temperature dependence of

the quasiparticle scattering rate below T_c . The zero-field microwave surface resistance measured by Bonn et al[18, 19] on the U.B.C. single crystals of YBa$_2$Cu$_3$O$_{6.95}$ addresses this issue rather directly. Figure 2.2 shows R_s as a function of temperature on a semi-log scale. (Incidentally, the sharpness of the transition as well as the magnitude of the drop of the surface resistance just below T_c is testimony to the quality of the U.B.C. single crystals). To analyze the data, they used a generalized two-fluid picture with the complex conductivity given by equation 2.4. The surface impedance is given by (see Appendix A)

$$Z_s = \left(\frac{i\,\mu_0\,\omega}{\tilde{\sigma}} \right)^{1/2}. \tag{2.8}$$

When $\sigma_1 \ll \sigma_2$ (which is a good approximation until very close to T_c), we obtain

$$R_s = \frac{1}{2}\, \mu_0^2\, \sigma_1\, \omega^2\, \lambda_L{}^3. \tag{2.9}$$

Taking λ_L from the penetration depth measurements of Hardy et al on the same single crystals, they obtain σ_1 as a function of temperature and this is shown in figure 2.3. Assuming a Drude type form for the conductivity, then

$$\sigma_1 \propto x_n(T)\, \tau(T) \tag{2.10}$$

if $\omega\tau \ll 1$ where $x_n(T)$ is the normal fluid fraction and $\tau(T)$ is the normal quasiparticle lifetime. In this two-fluid approach $x_n(T) = 1 - \lambda_L{}^2(0)/\lambda_L^2(T)$ and so they extract $\tau(T)$. This is given in figure 2.4, which shows a quasiparticle scattering rate that drops precipitously below T_c . The characteristic bump in the temperature dependence of the surface resistance is understood as follows: the initial drop below T_c is due to the onset of enhanced screening as λ_L decreases very quickly; below 77K, the increase in σ_1 due to the rapidly increasing τ wins out as the temperature dependence of λ_L slows down so that R_s starts increasing with decreasing temperature; at about 40K, we reach a peak in the conductivity below which the decreasing normal fluid fraction takes over as $1/\tau$
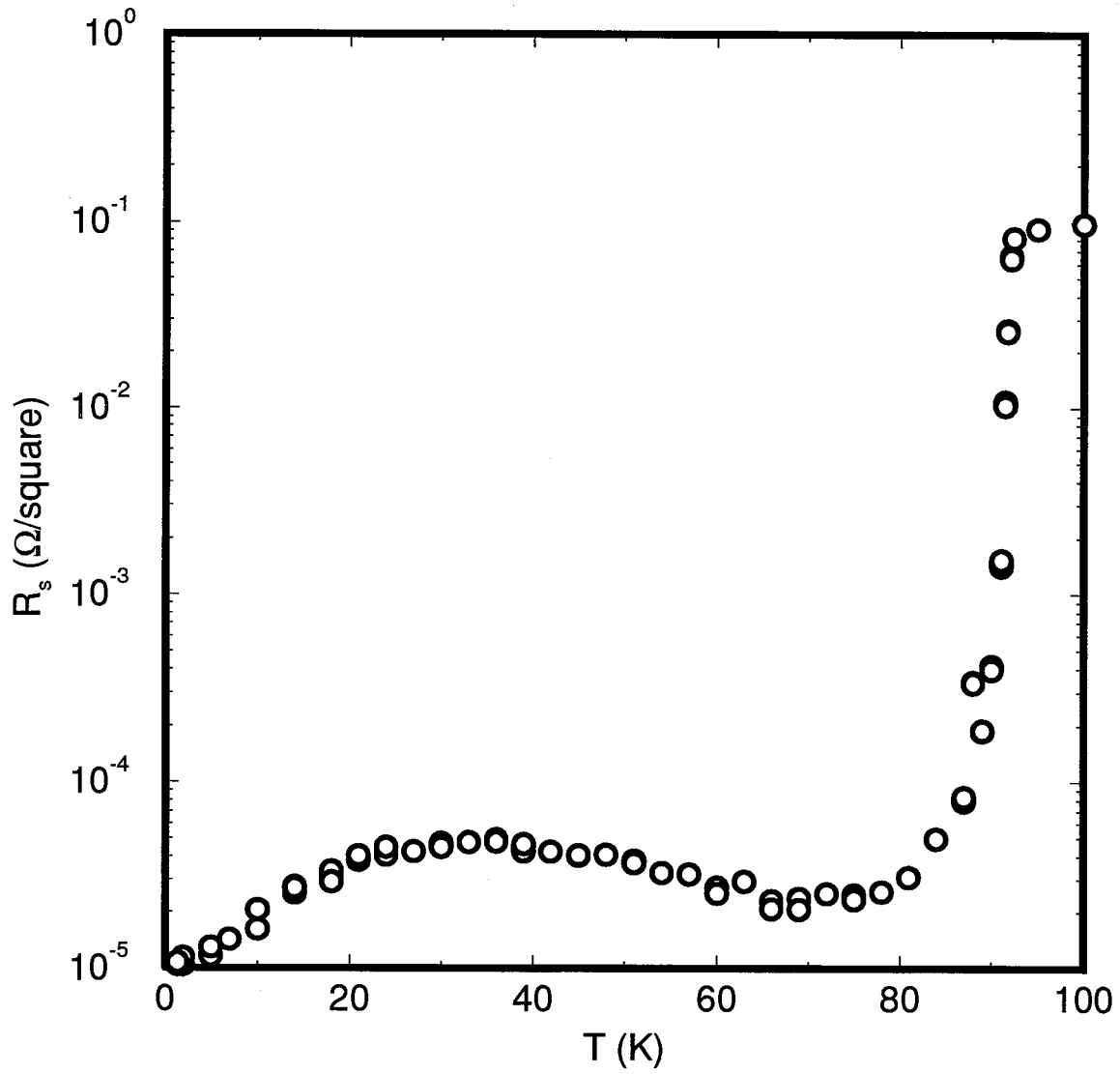
Figure 2.2: Temperature dependence of R_s at 3.9 GHz in zero field for $YBa_2Cu_3O_{6.95}$. This was measured by Bonn[39] on U.B.C. single crystals (Liang et al[30]).
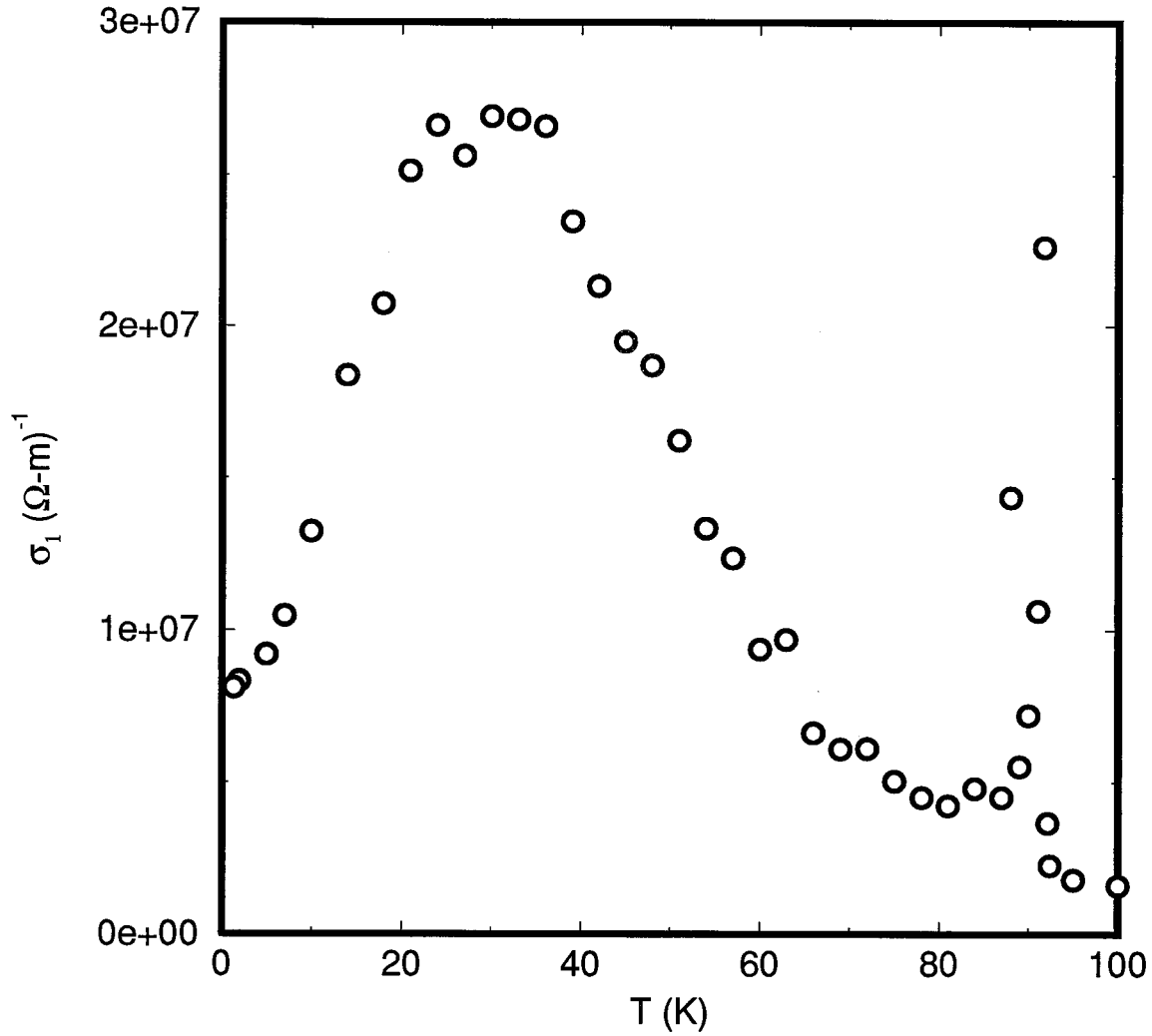
Figure 2.3: Temperature dependence of σ_1 at 3.9 GHz. This is obtained by Bonn[39] from the surface resistance using equation 2.9. The spike near T_c is thought to be due to slight broadening of the transition (the transition width is slightly wider than would be expected on the basis of the width of the specific heat jump at T_c). It is sample dependent and not thought to be part of the intrinsic physics.
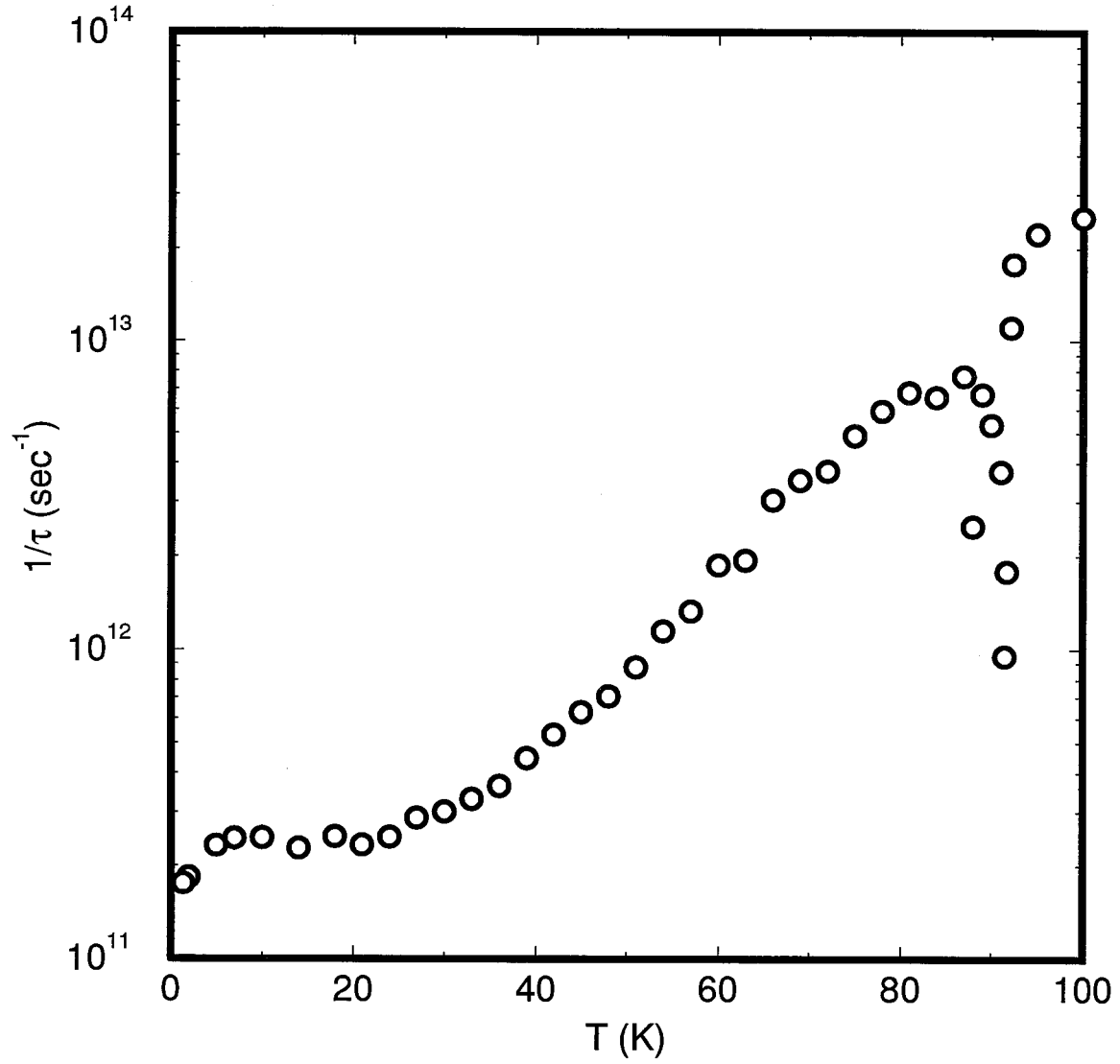
Figure 2.4: Temperature dependence of the quasiparticle scattering rate[39]. The spike at T_c is again due to sample dependent broadening of the transition. Below about 40 K, the scattering runs into an impurity limit and levels off.

begins to run into an impurity limit, and thus R_s starts decreasing again. It should be noted that the broad peak in the real part of the conductivity has nothing to do with a coherence peak. The rapidly decreasing quasiparticle scattering rate with an onset at T_c suggests the dominance of electron-electron scattering above T_c which is rapidly quenched once the charge carriers freeze out into the superconducting condensate. Certainly, an electron-phonon picture for the scattering seems unlikely.

Another aspect of the R_s temperature dependence which has provoked intense interest is its rather slow variation as $T \to 0$ (approximately linear). In a conventional BCS s-wave picture, an exponential temperature dependence is expected. Also suggestive of unconventional superconductivity in YBa$_2$Cu$_3$O$_{7-\delta}$ is the linear temperature dependence of $\Delta\lambda(T)$ at low temperatures measured by Hardy et al[40] (they measure $\Delta\lambda$ and take a value of $\lambda_L(0)$ from the literature to obtain $\lambda_L(T)$). This is shown in figure 2.5. Such a linear temperature dependence is predicted by calculations based on clean d-wave superconductors. For d-wave pairing, the gap function could be of the form

$$\Delta = \Delta_0 \left(\cos k_x - \cos k_y \right) \tag{2.11}$$

and this has line nodes on a cylindrical Fermi surface. Regions of the Fermi surface where the gap vanishes imply sets of low lying energy levels which have dramatic effects on the low temperature variation of a wide variety of properties. There is a growing body of evidence that is consistent with d-wave or at least some sort of effectively gapless superconductivity. For a more complete review of the evidence for and against a d-wave model of the high-T_c superconductors, the reader should consult Kallin et al[24].

2.2 Introduction to vortex motion in YBa$_2$Cu$_3$O$_{7-\delta}$

One of the principal differences in the vortex dynamics between high-T_c and conventional superconductors is the more prominent role of thermal effects. This is a vast subject
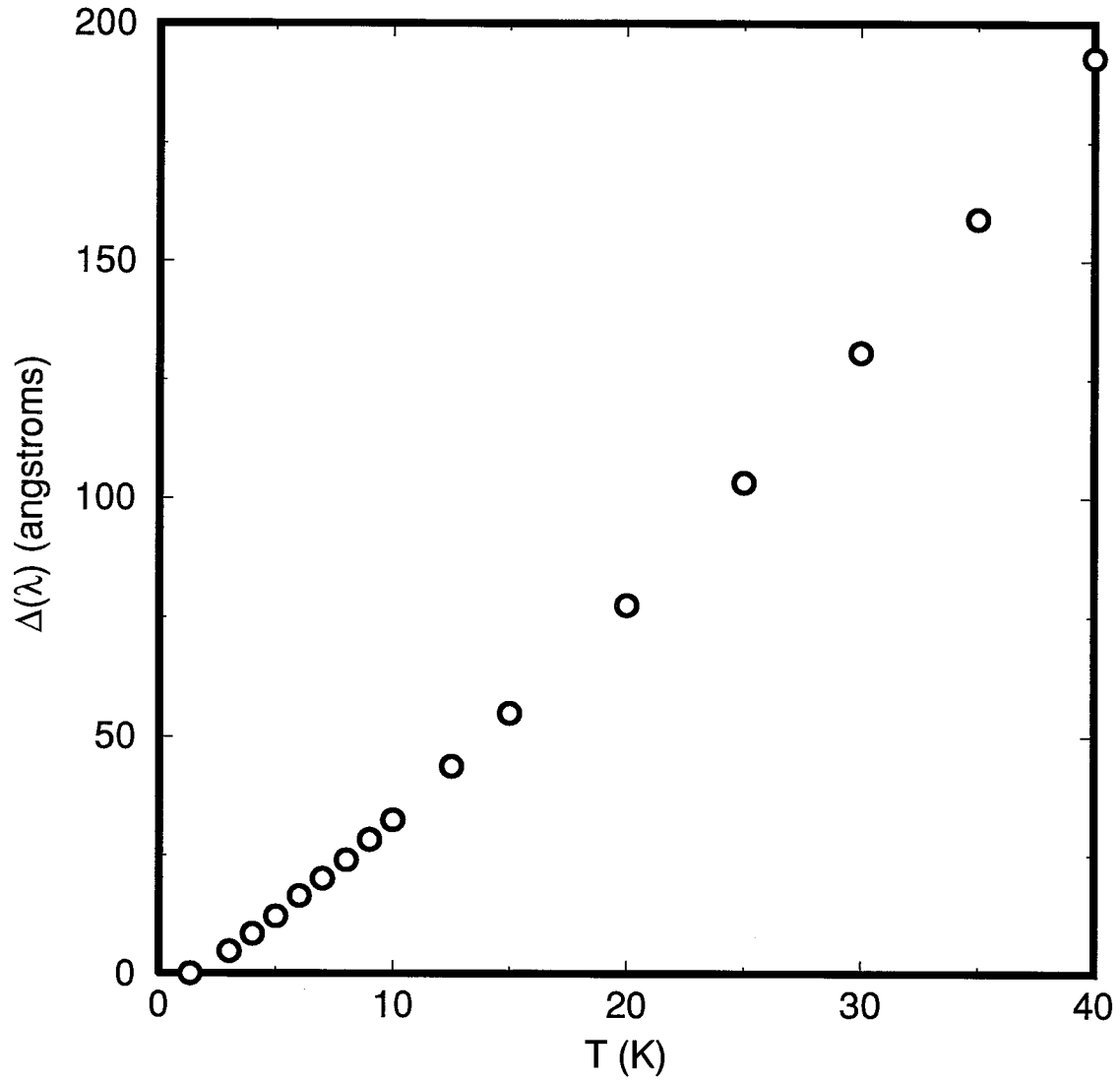
Figure 2.5: Temperature dependence of $\Delta(\lambda) = \lambda(T) - \lambda(1.3K)$ close to $T = 0$ as measured by Hardy et al[40]. This linear behaviour is strikingly different from the exponential decrease observed for conventional superconductors.

about which we give only a very general description, our main concern being to motivate the picture of vortex dynamics which we use in this thesis.

Palstra et al[27] have performed detailed studies of the dc resistivity of $YBa_2Cu_3O_{7-\delta}$ single crystals ($T_c \sim 88K$) in magnetic fields both perpendicular and parallel to the a-b plane. Figure 2.6 shows their measurements of ρ_{dc} as a function of T on a semi-log plot with the applied field perpendicular to the a-b plane. It is immediately apparent that even in fields up to 12T, the resistivity decreases very rapidly below T_c . For example, in a field of 1T, the resistivity has decreased at least five orders of magnitude by $\sim 80K$ ($t = T/T_c = 0.91$). They analyze their data in terms of the Anderson-Kim flux creep theory[41, 42]. In this scenario, vortices are pinned at the minima of a periodic pinning potential. They can move in response to the Lorentz force of the transport current even though the applied current is less than the depinning critical current due to thermal activation over the barrier height, U_0, between the neighbouring pinning sites. Based on this type of analysis, they find that the barrier heights or activation energies have already increased to approximately 500K in $YBa_2Cu_3O_{7-\delta}$ by the time t has dropped to ~ 0.93 (whereas activation energies as high as this are only found at temperatures, $T < 50K$, in $Bi_2Sr_2CaCu_2O_8$).

It is natural to postulate the existence of a boundary in H–T space above which the vortices are thermally depinned and flow freely for any transport current and below which a non-zero depinning critical current density still exists and must be exceeded to achieve flux flow. Such *irreversibility* or depinning lines have indeed been observed in both $YBa_2Cu_3O_{7-\delta}$ and $Bi_2Sr_2CaCu_2O_8$ [43]. There is considerable debate as to whether or not these are in fact 'melting' lines and representative of thermodynamic phase transitions from a vortex solid to a vortex liquid[44]. This is an interesting and complex subject but a discussion of it is beyond the scope of this thesis. The important point for our purposes is that while for $Bi_2Sr_2CaCu_2O_8$ this line (at low frequencies) is at $\sim 30K$ for
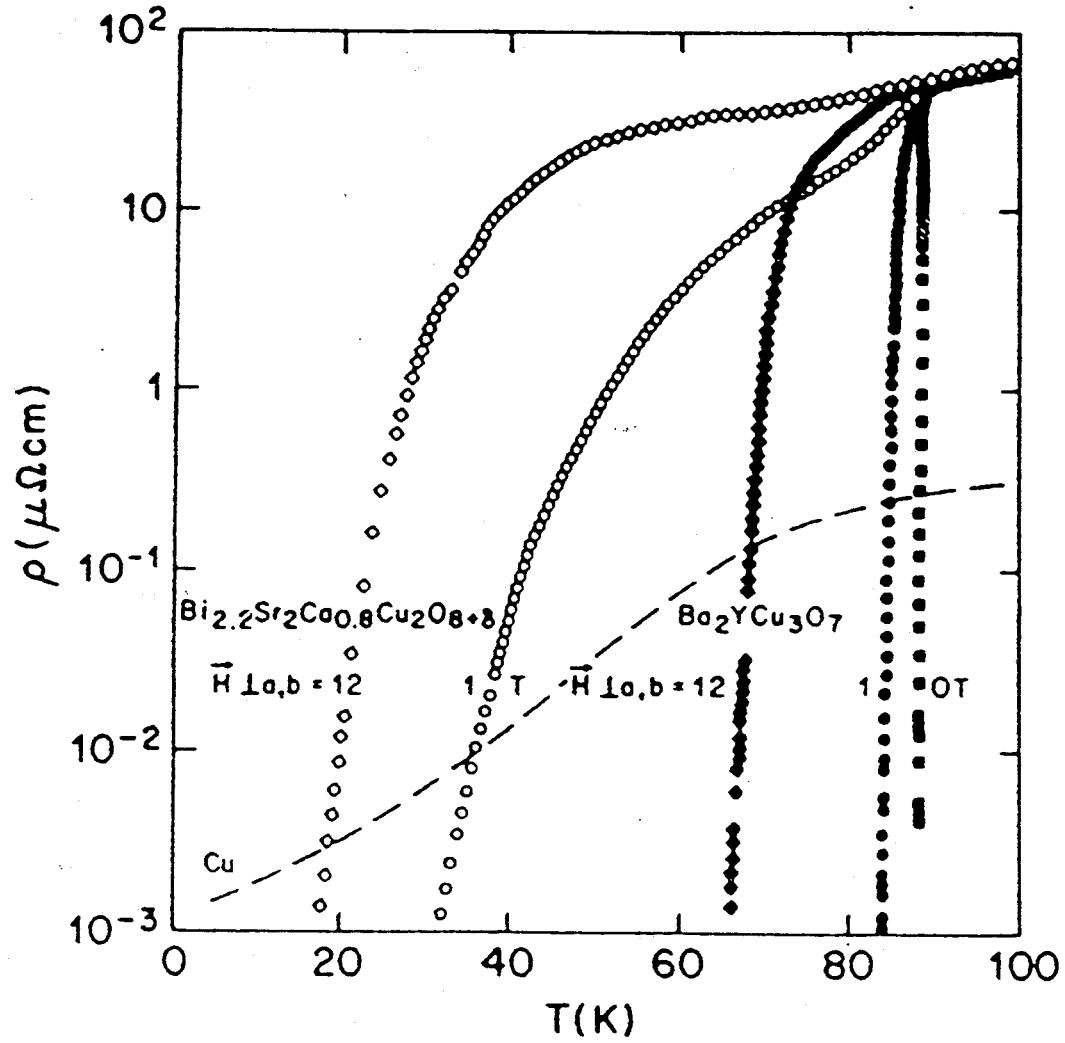
Figure 2.6: a-b plane resistivity of YBa$_2$Cu$_3$O$_{7-\delta}$ in a magnetic field. This is from the paper by Palstra et al[27]. Also shown is the a-b plane resistivity for Bi$_2$Sr$_2$CaCu$_2$O$_8$ which decreases much more slowly than in YBa$_2$Cu$_3$O$_{7-\delta}$

$0 < H < 10T$, for YBa$_2$Cu$_3$O$_{7-\delta}$ it is within a few degrees of T_c [43]. Moreover, this line is frequency dependent[27] and shifts to higher fields and temperatures as the frequency is increased. Palstra et al[27] remark that even for Bi$_2$Sr$_2$CaCu$_2$O$_8$, if the frequency is greater than 1GHz, thermally activated flux motion only plays a role very close to T_c . Within this picture, the reason for this frequency dependence is that at high enough frequencies the vortices never get a chance to wander far enough away from the pinning minima during the rf cycle to thermally hop to the next pinning site. In fact, at such high frequencies we must modify our picture[4, 5] to include explicitly a vortex viscosity, η, and a pinning force constant, κ_p, in our description of the dynamics. Together, they define another frequency scale, $\omega_p = \kappa_p/\eta$, called the *pinning frequency*. We defer a discussion of this until Chapter 3.

We conclude this introductory discussion of YBa$_2$Cu$_3$O$_{7-\delta}$ in the mixed state by briefly mentioning the work of Welp et al[45] who analyzed their magnetization data near T_c on single crystals of YBa$_2$Cu$_3$O$_{7-\delta}$ in terms of thermodynamic fluctuations. They find that in the temperature region corresponding to the upper half of the resistive transition in a magnetic field, their data scales according to Ginzburg–Landau theory for a 3-D superconductor. Thus, they argue that the characteristic shape of these dc transitions in a magnetic field as well as the apparent lack of field dependence on the the onset of superconductivity is a result of fluctuations. This must be kept in mind when we come to look at the surface resistance in a magnetic field close to T_c or H_{c_2} .

Chapter 3

Flux Flow in Conventional and High-T_c Superconductors

In this chapter, we will review the current understanding of flux-flow both in conventional and high-T_c superconductors. We will first describe the basic phenomenology of flux-flow and then summarize the theories that have been suggested to model the dissipation and Hall effect in conventional superconductors. These range from the semi-phenomenological approaches of Bardeen and Stephen[9] and Tinkham[46] to the more rigorous methods based on time dependent Ginzburg-Landau (TDGL) theory[10, 11, 12, 13, 14, 15]. We will then review some of the most important experiments aimed at understanding flux-flow. These experiments basically fall into two categories: dc and high frequency. In the second part of the chapter, we will summarize some of the work done on high-T_c superconductors, both theory and experiment.

3.1 Basic Properties of the Mixed State

In a type-II superconductor, the magnetic flux, instead of being screened out until the thermodynamic critical field, H_c, has been reached, starts to penetrate in the form of vortices once the applied field has exceeded a lower critical field, H_{c_1}. Each vortex is threaded by only one quantum of flux, $\Phi_0 = h/2e$. If the number of vortices per unit area is given by n, then the average magnetic field is given by $B = n\phi_0$. As the applied field is increased, the superconductor is penetrated by greater and greater numbers of vortices until at an applied field $H_{c_2} > H_c$, the superconductivity is quenched and a transition into the normal state occurs.

A vortex consists of a core of radius equal to the coherence length, ξ, in which the order parameter (or equivalently, the density of superconducting electrons) decreases to zero at the centre from its bulk, equilibrium value at the perimeter. The microscopic magnetic field is maximum at the centre of the vortex and decays to zero outside the core due to circulating supercurrents that screen out the field over a length scale characterized by the penetration depth, λ_L. For typical type-II superconductors, $\lambda_L \gg \xi$, and so a typical vortex has an essentially normal inner core where the density of the superconducting electrons goes to zero and a much larger region outside this core where the supercurrents and the field decays. The concept of a 'normal' core was put on a more rigorous footing by Caroli, de Gennes and Matricon[21] who found that although the order parameter is strictly zero only at the centre of the vortex, there is a sea of low lying energy levels with spacing of order Δ^2/E_F ($\sim$ 1 mK for conventional superconductors) centred on the axis of the vortex that acts essentially like a cylinder of normal material with radius ξ.

3.2 Transport Properties

3.2.1 Simple treatment of the viscous flow of vortices

We now consider such a lattice in the presence of a uniform, superfluid, transport current $\mathbf{J} = \mathbf{J}_T$ as shown in figure 3.1. In the presence of the transport current, each vortex is subjected to a Lorentz force per unit length, $\mathbf{J} \times \mathbf{\Phi_0}$ which in the absence of other forces causes them to move in a direction perpendicular to the direction of the transport current[34]. In a real material, there may be defects and other structures which tend to pin the vortices and stop them from moving in response to the Lorentz force. For the moment, we consider an ideal material where there is no pinning and the vortices are thus totally free to move. The moving vortex gives rise to a time dependent magnetic field on a microscopic scale and so we might expect an induced electric field in the direction of
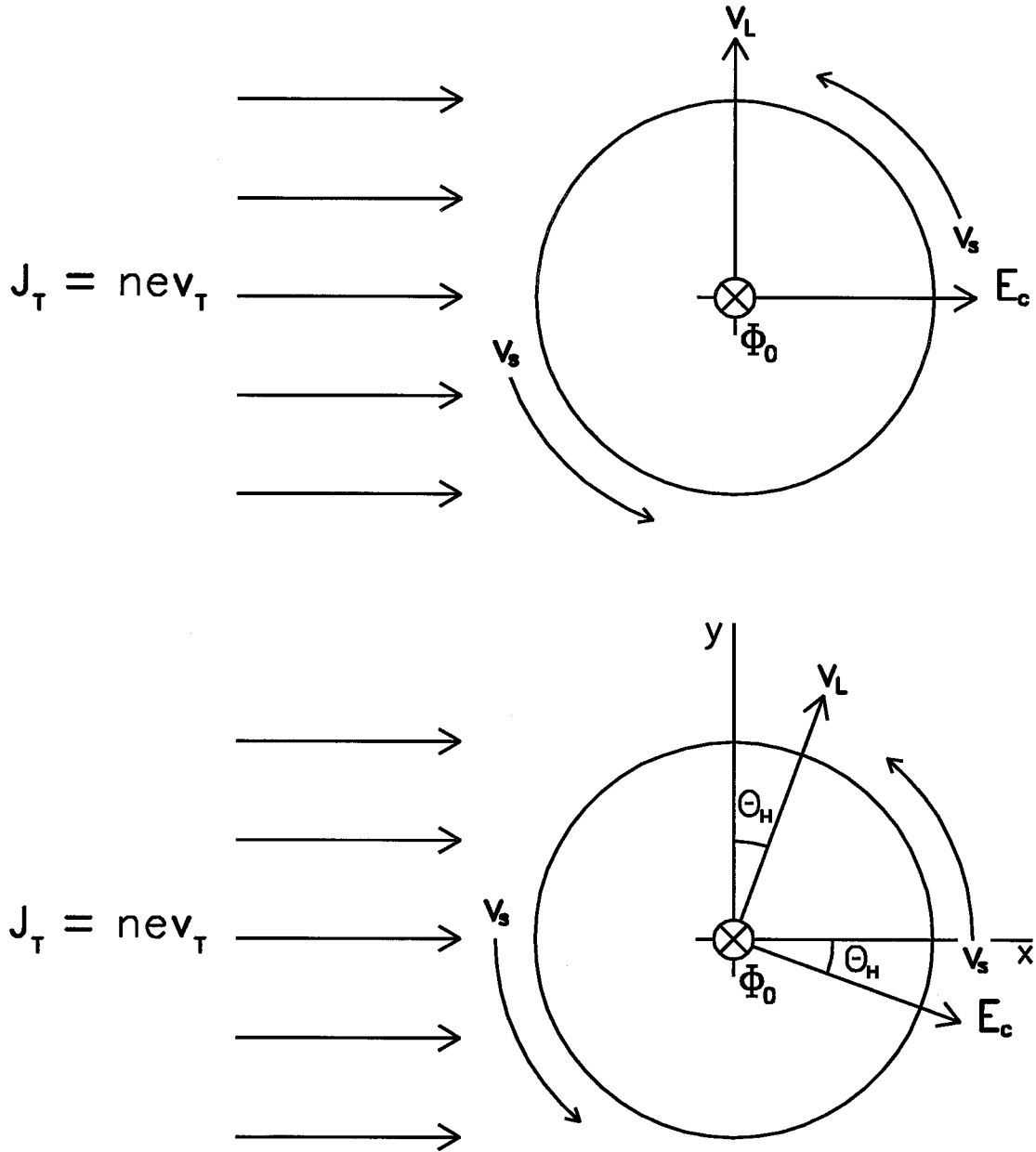
Figure 3.1: Vortex motion in response to a uniform, superfluid, transport current. The upper figure shows the response considering only the conventional Lorentz force. The lower figure includes the magnus force which is thought to be responsible for the Hall effect.

the transport current coming from the Maxwell equation $\nabla \times \mathbf{E} = -\partial \mathbf{B}/\partial t$. It has been argued[47], however, that in a steady state experiment with vortices moving across the sample (perpendicular to the transport current) and leaving on one side while entering on the opposite side at the same rate, there is no net change of flux through a circuit consisting of the superconductor and a voltmeter, and thus there should be no induced electric field. This question was resolved by Josephson[48] who found that the electric field created by moving vortices with velocity $\mathbf{v_L}$ is indeed

$$\mathbf{E} = -\mathbf{v_L} \times \mathbf{B} \tag{3.1}$$

as we might guess based on a simple induction mechanism. The gist of this argument can be gleaned by considering a closed loop, C, consisting of a segment, C_2, that resides entirely in a purely superconducting region and a segment, C_1, that completes the loop in a superconducting region in the mixed state. From Faraday's law[49] we have that

$$\oint_C \mathbf{E} \cdot d\mathbf{l} = -\oint_C \mathbf{v_L} \times \mathbf{B} \cdot d\mathbf{l} \tag{3.2}$$

where $\mathbf{E}$ is the electric field around the loop and $\mathbf{v_L}$ is the velocity at which the magnetic flux crosses the boundary. No flux can cross the boundary, C_2, in the superconducting region and $\mathbf{E}$ is everywhere zero inside the pure superconductor; therefore, equation 3.2 becomes

$$\int_{C_1} \mathbf{E} \cdot d\mathbf{l} = -\int_{C_1} \mathbf{v_L} \times \mathbf{B} \cdot d\mathbf{l} \ . \tag{3.3}$$

If we assume that the field distribution at a point in the mixed state is only determined by the flux lines etc. in the immediate vicinity, then equation 3.3 holds for any path C_1, not just one completed through a purely superconducting region. The differential form of equation 3.3 is given by equation 3.1.

Since there is an electric field parallel to the transport current, there is energy dissipation per unit volume given by

$$P = \mathbf{E} \cdot \mathbf{J} \tag{3.4}$$

The situation is similar to a normal material where a voltage, V, is developed along the path of the current, I, and we get energy dissipation VI. This energy dissipation can be taken into account in a phenomenological fashion by introducing the parameter η, called the vortex viscosity. We imagine that the energy dissipation comes from the work done against a viscous force per unit length of vortex, $\eta \mathbf{v_L}$. Then in the steady state with no pinning, we have

$$J \, \Phi_0 = \eta \, v_L \, . \tag{3.5}$$

Using $E = v_L B$, we get

$$\rho_{ff} = \frac{E}{J} = \frac{\Phi_0 \, B}{\eta} \tag{3.6}$$

where we have defined ρ_{ff} to be the *flux-flow resistivity* — the ratio of the induced electric field to the applied transport current. The work done per unit time per unit length by the viscous force to dissipate energy can be written

$$W = -\mathbf{F} \cdot \mathbf{v_L} = \eta \, v_L{}^2. \tag{3.7}$$

Equivalently, we can write the power per unit volume as

$$P = \mathbf{E} \cdot \mathbf{J} = \rho_{ff} \, J^2 = n(\eta \, v_L{}^2) \tag{3.8}$$

Since n is the density of vortices per unit area, we find again that the energy dissipated per unit length is given by $\eta v_L{}^2$.

3.2.2   Viscous flow including the Hall Effect

Although the treatment given in section 3.2.1 is a good starting point for understanding flux flow and, indeed has been used extensively to model experiments, it ignores the Hall effect where there is a component of vortex velocity not strictly perpendicular to the applied superfluid transport current. It has been argued, originally by de Gennes and

Matricon[50], and subsequently by Nozières and Vinen[20], that this motion is the result of the Magnus force similar to that felt by vortices in a classical uncharged fluid. In this scenario, the force exerted on the vortex is not simply $\mathbf{J} \times \boldsymbol{\Phi_0} = n_s e \mathbf{v_T} \times \boldsymbol{\Phi_0}$ but

$$n_s e \left(\mathbf{v_T} - \mathbf{v_L}\right) \times \boldsymbol{\Phi_0} \tag{3.9}$$

where it is now the relative velocity of the vortex with respect to the applied superfluid velocity that determines the Lorentz force. We can clearly see from this expression that a vortex moving in a direction perpendicular to the transport current will see a force in the direction of the transport current. The force balance equation for the vortex becomes

$$\mathbf{f} + n_s e \left(\mathbf{v_T} - \mathbf{v_L}\right) \times \boldsymbol{\Phi_0} = 0 \tag{3.10}$$

where $\mathbf{f}$ is the frictional drag term. This equation is appealing because in the limit of a pure superconductor, $\mathbf{f} = 0$ and so $\mathbf{v_T} = \mathbf{v_L}$ i.e. the vortices move along with the superfluid as in superfluid helium II. However, writing $\mathbf{f} = -\eta \mathbf{v_L}$ leads to significant disagreement with experiment[51]. It was argued by Bardeen[52] that the term $n_s e \, \mathbf{v_L} \times \boldsymbol{\Phi_0}$ should be dropped while Nozières and Vinen assert that it is the form of the frictional drag force that must be modified. This question has never been entirely resolved (indeed, a complete theory of flux-flow valid in all limits of physical interest has yet to be developed), but as a reasonable compromise we can write a force balance equation in terms of phenomenological parameters to be determined either by experiment or subsequent theory[53]:

$$\eta \, \mathbf{v_L} - \alpha \, \mathbf{v_L} \times \hat{\mathbf{z}} = -\Phi_0 \mathbf{J} \times \hat{\mathbf{z}} \, , \tag{3.11}$$

where we have now taken $\boldsymbol{\Phi_0} = -\Phi_0 \hat{\mathbf{z}}$ in order to be consistent with figure 3.1. $\mathbf{J} = \mathbf{J_T}$ as before is the superfluid transport current density (in the x-direction), $n_s e \mathbf{v_T}$, and α is a parameter that together with η determines the Hall angle (see figure 3.1). The $\alpha \mathbf{v_L} \times \hat{\mathbf{z}}$ term comes from the second term on the LHS of equation 3.10, with its coefficient now

given by α. The $\Phi_0 \mathbf{J} \times \hat{\mathbf{z}}$ term (conventionally thought of as the Lorentz force) is precisely the first term on the LHS of equation 3.10. Since we now have a component of the vortex viscosity in both the x and the y direction, the derivation of the longitudinal flux-flow resistivity is less trivial. Writing down the x and y components of the equation, we have

$$\eta \, v_{Lx} - \alpha \, v_{Ly} = 0 \qquad (3.12)$$

$$\eta \, v_{Ly} + \alpha \, v_{Lx} = \Phi_0 \, J \qquad (3.13)$$

Using equation 3.1 for the induced electric field, we have

$$E_x = v_{Ly} B \quad ; \quad E_y = -v_{Lx} B \qquad (3.14)$$

and since

$$\rho_{ff} = \frac{E_x}{J_x} = \frac{E_x}{J} = \frac{v_{Ly} B}{J} \qquad (3.15)$$

and

$$|\tan\theta_H| = \frac{E_y}{E_x} = -\frac{v_{Lx}}{v_{Ly}} \qquad (3.16)$$

(θ_H is the Hall angle) we find that

$$\rho_{ff} = \frac{\Phi_0 \, B}{\eta \left(1 + \frac{\alpha^2}{\eta^2}\right)} \qquad (3.17)$$

$$\tan\theta_H = \frac{\alpha}{\eta} \qquad (3.18)$$

To first order in α/η, we recover equation 3.6, the previous result for the flux-flow resistivity. We learn from this that for small Hall angle, we get the same flux-flow resistivity that we would get in the absence of Hall fields.

There have been two main approaches[1] to modelling this power dissipation in terms of parameters describing the structure of the vortex. The most widely known approach is

---

[1] There is also the model proposed by Clem[54] who showed that dissipation can arise from irreversible entropy flow. His ideas were used to explain the existence of a flux flow resistivity minimum as a function of temperature that was observed in certain high κ alloys such as Ti-V[1].

the one due to Bardeen and Stephen. The other involves the more rigorous calculations based on time dependent Ginzburg Landau theory originally inspired by Tinkham's ideas on the time relaxation of the order parameter. We consider first the Bardeen-Stephen theory.

3.3 The Bardeen-Stephen Model

Given the picture of a vortex core as a cylinder of normal material, a natural approach to modelling the dissipation due to a moving vortex would be to somehow relate it to joule heating of the normal electrons in the core. This is in essence the approach taken by Bardeen and Stephen in their solution of the problem[9]. They model the vortex in terms of a totally normal core (superconducting order parameter is zero) of radius the coherence length, ξ, and a transition region outside the normal core where the order parameter goes from zero to its equilibrium value in the bulk. Their theory is derived at zero temperature and in the clean limit where the mean free path, l, is greater than the coherence length.

Following Tinkham[34], we can quickly reproduce the calculation of the dissipation due to the electrons in the core (in the slightly more simplified case that, outside the core, the material is completely superconducting). We imagine a vortex at the origin (its magnetic flux directed in the $-z$-direction) with a velocity, $\mathbf{v_L}$, in the y-direction (see upper diagram in figure 3.1). We use the first London equation, equation 2.6, to relate the electric field outside the normal core to the circulating superfluid current density:

$$\mathbf{E} = \frac{\partial}{\partial t} \left(\frac{m\,\mathbf{v_s}}{e} \right) \tag{3.19}$$

where we have used that $\mathbf{J_s}(\mathbf{r} - \mathbf{v_L}t) = n_s e \mathbf{v_s}(\mathbf{r} - \mathbf{v_L}t)$. We have by the chain rule that

$$\frac{\partial \mathbf{v_s}}{\partial t} = -(\mathbf{v_L} \cdot \nabla)\,\mathbf{v_s} \;, \tag{3.20}$$

and so we get that

$$\mathbf{E} = -\mathbf{v_L} \cdot \nabla \left(\frac{m\mathbf{v_s}}{e} \right) . \tag{3.21}$$

For $\lambda_L \gg \xi$ ($\kappa \gg 1$), we have that[34]

$$\mathbf{v_s} = \frac{\hbar}{m\,r} \, \hat{\theta} , \tag{3.22}$$

where θ is measured from the x-direction and $\hat{\theta}$ is a unit vector in the direction of increasing θ. Substituting this into equation 3.21 and recalling that $\mathbf{v_L}$ is in the y-direction

$$\mathbf{E} = - \left(\frac{v_L \, \Phi_0}{2\,\pi} \right) \frac{\partial}{\partial y} \left(\frac{\hat{\theta}}{r} \right) = - \frac{v_l \, \Phi_0}{2\,\pi\,r^2} (\sin\theta \, \hat{\theta} + \cos\theta \, \hat{r}) . \tag{3.23}$$

Requiring continuity of the tangential component of $\mathbf{E}$ at the boundary of the normal core gives a uniform electric field in the core

$$\mathbf{E} = \frac{v_L \, \Phi_0}{2\,\pi\,\xi^2} \, \hat{\mathbf{x}} . \tag{3.24}$$

We can see this because at $r = \xi$ and $\theta = \pi/2, 3\pi/2$, the electric field is given by the above expression, whereas, in the core, we have both $\nabla \cdot \mathbf{E} = 0$ and $\nabla \times \mathbf{E} = 0$, and so a constant field given by equation 3.24 certainly satisfies Maxwell's equations and also satisfies the boundary condition on the tangential component of $\mathbf{E}$. Therefore, it is the unique solution for the electric field in the core. Of course, discontinuity of the normal component of $\mathbf{E}$ implies a surface charge density at the core boundary. This is an unrealistic feature of the model due to the simplified view being taken of the vortex core; in reality, this charge density would be smeared out.

We can now easily calculate the energy dissipation per unit length of vortex in the core. Since the core is normal with a conductivity, σ_n, we have $J = \sigma_n E$ and so the dissipation per unit length is given by

$$W = \pi\,\xi^2\,J\,E = \pi\,\xi^2\,\sigma_n\,E^2 = \frac{\sigma_n\,v_L^2\,\Phi_0^2}{4\,\pi\,\xi^2} . \tag{3.25}$$

This calculation of the dissipation relies on local equilibrium of the electrons in the normal core with the lattice. It was remarked by Nozières and Vinen[20] that this does not make sense for the situation where the mean free path is bigger than the core size ($l > \xi$). However, Bardeen et al[9] argued that even if an individual electron does not suffer a collision in the core, the friction force involves an average over all electrons and so the picture still makes sense on the average.

It turns out that an equal amount of dissipation occurs due to normal currents in the transition region outside the core (where the order parameter rises back up to its bulk, equilibrium value), but this is considerably more complicated to calculate[9]. The total dissipation is therefore

$$W = \frac{\sigma_n \, v_L^2 \, \Phi_0^2}{2 \, \pi \, \xi^2} \,. \tag{3.26}$$

Equating this to $W = \eta v_L^2$, and using

$$\mu_0 \, H_{c_2} = \frac{\Phi_0}{2 \, \pi \, \xi^2} \tag{3.27}$$

we get

$$\eta = \frac{\Phi_0 \, \mu_0 \, H_{c_2}}{\rho_n} \,. \tag{3.28}$$

In terms of the flux-flow resistivity, this becomes

$$\frac{\rho_{ff}}{\rho_n} = \frac{H}{H_{c_2}} \,. \tag{3.29}$$

This is an appealing result because H/H_{c_2} is roughly the fraction of material in the normal cores of the vortices, and so it is as if the current flows right through them. In fact, we can calculate the velocity of the electrons in the cores. If we consider the cores to be normal material with an electron scattering time, τ, then

$$\mathbf{v_c} = (e \, \tau / m) \, \mathbf{E} \,. \tag{3.30}$$

Equating the viscous force with the Lorentz force on the vortices, we get

$$\eta \, v_L = J \, \Phi_0 = n \, e \, v_T \, (h/2\,e) = (n \, h/2) \, v_T \; . \tag{3.31}$$

Combining equations 3.30, 3.24 and 3.31 we find

$$\mathbf{v_c} = \mathbf{v_T} \; . \tag{3.32}$$

In other words, the normal current density in the cores equals the superfluid transport current density and so we see that in this picture the current does indeed flow right through the moving cores. It is important to realize that the motion of the cores is essential otherwise the material in the superconducting bulk would simply short out the normal material in the vortices.

Close to T_c we can explicitly verify that the dissipation due to the normal currents outside the core contributes as much to the total dissipation as the normal currents inside the core. Close to T_c , the real part of the conductivity is approximately equal to the conductivity of the normal material above T_c (see figure 2.3 for example) and so the dissipation can be written

$$P = \int_{\xi}^{\infty} \int_{0}^{2\pi} \sigma_n \, \mathbf{E(r)} \cdot \mathbf{E(r)} \, r \, \mathrm{d}r \, \mathrm{d}\theta \; . \tag{3.33}$$

Using equation 3.23 for the electric field outside the core, we have

$$P = \frac{\sigma_n \, v_L^2 \, \phi_0^2}{4 \, \pi} \int_{\xi}^{\infty} \int_{0}^{2\pi} \frac{1}{r^4} \, r \, \mathrm{d}r \, \mathrm{d}\theta = \frac{\sigma_n \, v_L^2 \, \Phi_0^2}{4 \, \pi \, \xi^2} \tag{3.34}$$

and this is the same as the dissipation from equation 3.25. Thus close to T_c , we have

$$\frac{\rho_{ff}}{\rho_n} = \frac{H}{H_{c_2}(T)} \; . \tag{3.35}$$

In treating the Hall effect, Bardeen and Stephen replace the simple expression for the core velocity, equation 3.30, with

$$\mathbf{v_c} = (e \, \tau/m) \, \mathbf{E} + \frac{e \, \tau}{m} \, (\mathbf{v_c} \times \mathbf{B}) \; . \tag{3.36}$$

This is just the expression we would use for the drift velocity of electrons in a normal material in a field H [2] (and in this model the Hall effect due to the currents in the transition region is the same as that due to the normal currents in the core[55]). Using $\mathbf{v_c} = \mathbf{v_T}$ from equation 3.32 we can write this as

$$\mathbf{v_T} = (e\tau/m)\,\mathbf{E} + \frac{e\tau}{m}\,(\mathbf{v_T} \times \mathbf{B})\ .\tag{3.38}$$

Resolving this equation into x and y-components as we did with equation 3.11, we find

$$\frac{\rho_{ff}}{\rho_n} = \frac{H}{H_{c_2}}\tag{3.39}$$

as before, and

$$\tan\theta_H = \omega_c\,\tau\tag{3.40}$$

where ω_c is the cyclotron frequency, eB/m. For $\omega_c\tau \gg 1$, we find that $v_L = (H/H_{c_2})v_T$ which does not reduce to $v_L = v_T$ as expected for a pure superconductor. Nozières and Vinen[20] suggested a slight modification of the Bardeen-Stephen model which yields the same flux-flow resistivity but

$$\tan\theta_H = \omega_{c_2}\tau\tag{3.41}$$

where $\omega_{c_2} = eB_{c_2}/m$. In the limit $\omega_{c_2}\tau \gg 1$, their equation reduces to $\mathbf{v_L} = \mathbf{v_T}$.

For conventional superconductors, $\omega_c\tau$ and $\omega_{c_2}\tau$ are both small and so only small Hall angles are expected. In any event, the longitudinal flux-flow resistivity is left unchanged.

---

[2]The force acting on a charge carrier of charge e with velocity $\mathbf{v}$ (and scattering time τ) in an electric field $\mathbf{E}$ and magnetic field $\mathbf{B}$ can be written as a differential equation for the momentum $\mathbf{p} = m\mathbf{v}$:

$$\frac{d\mathbf{p}}{dt} = e\,(\mathbf{E} + \mathbf{v} \times \mathbf{B}) - \frac{\mathbf{p}}{\tau}\ .\tag{3.37}$$

In the steady state, $d\mathbf{p}/dt = 0$, and we get equation 3.36.

3.4   Tinkham's time dependent order parameter and TDGL

Tinkham's idea[46] was that there is energy dissipation associated with the time dependence of the order parameter at a particular location in the superconductor due to the passage of a moving vortex through that point. The order parameter, $|\psi|^2$, at this point changes from its equilibrium value, $|\psi_0|^2$, (before the arrival of the vortex) to zero (the axis of the vortex lies on top of the point) back to $|\psi_0|^2$ again (after the vortex has passed through). Following Gor'kov and Kopnin[15], we give a rough calculation of the flux-flow resistivity that we would get due to this mechanism valid for dirty superconductors at low temperature.

We can estimate the time required to reestablish equilibrium in the superconductor after the passage of a vortex as the time taken for an electron to move a distance of the order of the coherence length (for a dirty superconductor $\xi \sim l$) and since $\xi \sim \hbar v_F / \Delta$ (v_F is the Fermi velocity and Δ the energy gap) we get

$$\tau_0 = \frac{\xi}{v_F} \sim \frac{\hbar}{\Delta} \, . \tag{3.42}$$

The time it takes for the vortex to pass through any given point in the superconductor will be of the order

$$t_0 \sim \frac{\xi}{v_L} \, . \tag{3.43}$$

Since $1/\tau_0$ is the gap frequency, $\tau_0/t_0 \ll 1$ for most processes and so, if F is the free energy density, the amount of energy dissipated will be approximately the fraction $(\tau_0/t_0) < F >$ ($< F >$ is the time average of the free energy density). Tinkham interprets this energy dissipation as the result of generation and heating of normal quasiparticles as the electrons leave and condense back into the superconducting condensate during the non-equilibrium situation that causes the finite rate of change of $|\psi|^2$. The power per unit volume in a

superconductor with vortex density, n, and an average flux density $B = n\Phi_0$ is

$$W = \frac{\tau_0}{t_0^2} < F > n\xi^2 .$$ (3.44)

Substituting for t_0 and n and using $< F > \sim H_c^2$ we find

$$W = \frac{\tau_0\, v_L^2\, H_c^2\, B}{\Phi_0} .$$ (3.45)

Since

$$W = (1/\rho_{ff})\, E^2 = \sigma_{ff}\, E^2 = \sigma_{ff}\, v_L^2\, B^2 ,$$ (3.46)

we have using $H_{c_1} \sim \Phi_0/\lambda^2$ (λ is the penetration depth in a dirty superconductor and is different from the London penetration depth) and $H_c^2 = H_{c_1} H_{c_2}$ that

$$\sigma_{ff} = \frac{\tau_0\, H_c^2}{B\, \lambda^2\, H_{c_1}} = \frac{\tau_0\, H_{c_2}}{B\, \lambda^2} .$$ (3.47)

For a dirty superconductor, $\lambda^2 \sim \lambda_L^2 \xi_0/l$ and so we can write

$$\sigma_n = \frac{n\, e^2\, l}{m\, v_F} = \frac{l}{v_F\, \lambda_L^2(0)} = \frac{\hbar}{\Delta(0)\, \lambda^2(0)} .$$ (3.48)

Together with equation 3.47 this gives

$$\frac{\rho_{ff}}{\rho_n} \sim \frac{H}{H_{c_2}}$$ (3.49)

in qualitative agreement with the Bardeen-Stephen result.

A more rigorous approach to the effects of a time dependent order parameter in the context of moving vortices was attempted using the time dependent Ginzburg Landau theory originally formulated by Gor'kov and Eliashberg[56]. The difficulties in solving a time dependent version of the Ginzburg Landau equations are such that the solutions obtained were mostly restricted to gapless superconductors. Following the work of Schmid[57] and of Caroli and Maki[10, 11, 12, 13], Thompson and Hu[14] were able to

obtain expressions for ρ_{ff} in a high κ superconductor with a large number of paramagnetic impurities (to satisfy the condition that the superconductor be gapless). Among other things, their solutions contained supercurrents in the core of the vortex. Tinkham[34] has pointed out how this highlights the oversimplification involved in considering the core to be a cylinder of normal material. Nevertheless, in the limit as $T \to 0$ for a dirty superconductor with no paramagnetic impurities, Gor'kov and Kopnin[16] obtained the expression

$$\frac{\rho_{ff}}{\rho_n} = 1.1 \frac{H}{H_{c_2}(0)} \tag{3.50}$$

which is in good agreement with the simple Bardeen-Stephen result.

3.5 Experiments on Flux Flow

We will discuss first the dc measurements made mostly on superconducting alloys such as PbIn and NbTa. Real materials have defects which tend to pin the vortices and stop them from moving in response to some driving force. Indeed, this is a very desirable feature when fabricating magnets out of superconducting wire. Such magnets are designed to run in the so-called persistent mode where they are disconnected from the power supply after having been charged to the desired current. Because the wires are sitting in their own high magnetic field, they are threaded by many vortices. These vortices will move in response to the Lorentz force and hence cause energy dissipation and degradation of the current unless they are held in position by even stronger pinning forces. However, for doing experiments probing intrinsic physics, it means that a large enough transport current (called the depinning critical current) must be applied to overcome the pinning forces. The I-V characteristics of such an experiment (performed by Kim et al[1]) when a dc current is applied to PbIn alloys is shown in figure 3.2. To define the flux-flow

resistivity under such circumstances requires a slightly different approach from the zero-pinning case. Now we have

$$\eta \, v_L = F_L - F_P \quad \text{for } F_L > F_P \tag{3.51}$$

where F_P is the pinning force and F_L is the Lorentz force $J \, \Phi_0$. Since $E = v_L B$, we get

$$\rho_{ff} = \frac{dE}{dJ} = \frac{\Phi_0 \, B}{\eta} \tag{3.52}$$

and here we have generalized the definition of the ρ_{ff} to be the *derivative* of the electric field with respect to the current. Experimentally, this means that the flux-flow resistivity is obtained from the slope of the I-V characteristic once the depinning critical current has been exceeded. This slope was found to be independent of the critical current as it would have to be for this definition of ρ_{ff} to be consistent. A set of ρ_{ff} curves as a function of field is shown in figure 3.3 for a $Nb_{0.5}Ta_{0.5}$ alloy. For low temperatures and fields, we see that

$$\frac{\rho_{ff}}{\rho_n} = \frac{H}{H_{c_2}(0)}. \tag{3.53}$$

As the temperature gets closer to T_c , this empirical law is violated at lower and lower fields; nevertheless, for small enough fields the slope of the ρ_{ff}/ρ_n is $1/H_{c_2}(0)$ for all temperatures (note that the ρ_n used to scale the ρ_{ff} data is independent of temperature and equal to $\rho_n(T_c)$ since an alloy is in the impurity limit by T_c). This behaviour is claimed to be representative of low-field ($H_{c_2}(0) \sim 1\text{T}$), intermediate ($\kappa \sim 5$) superconducting alloys such as NbTa and PbIn. A similar result was obtained by Vinen and Warren[2] on Nb and NbTa alloys. Thus the data at low fields seem to agree with the zero temperature Bardeen-Stephen result even though this result was derived for a pure, clean-limit superconductor whereas the alloys used in the experiments are in the dirty limit. The result is also in agreement at with the TDGL result, equation 3.50, for dirty superconductors for $T \ll T_c$ and $H \ll H_{c_2}$.
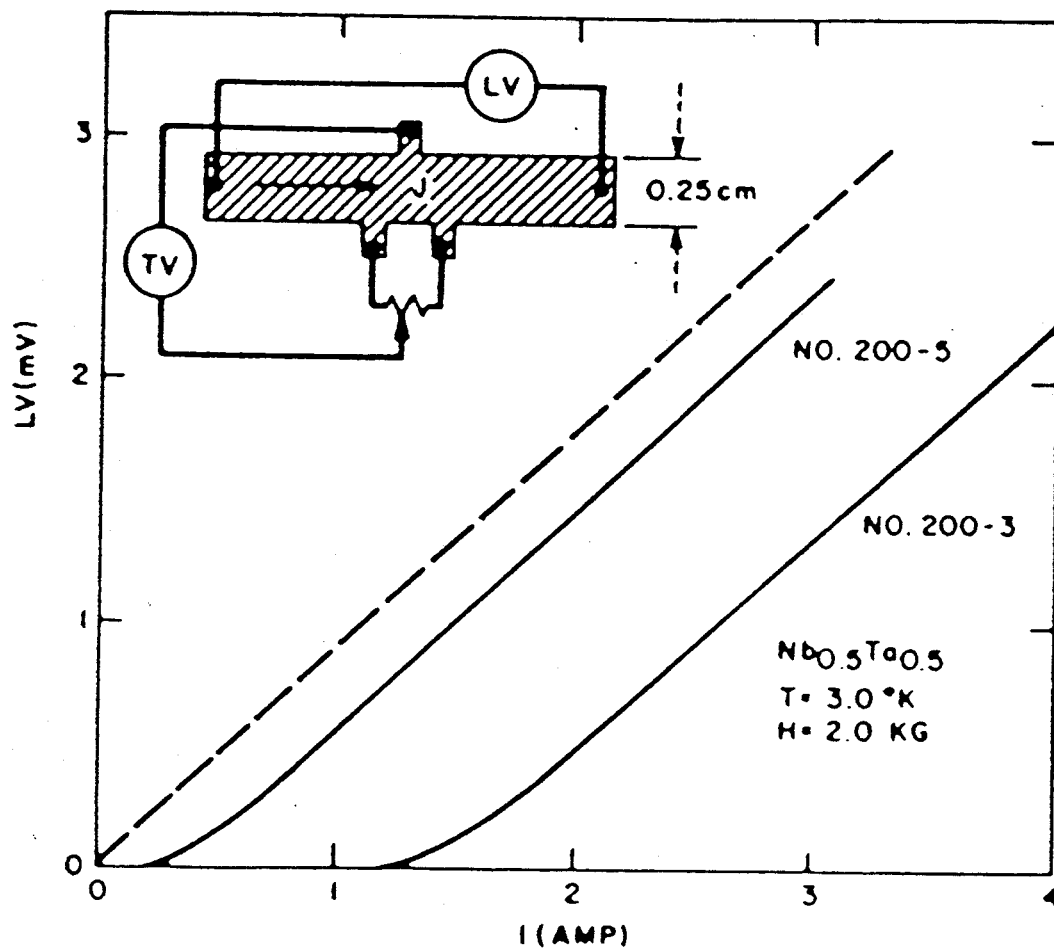
Figure 3.2: I-V characteristics for Nb$_{0.5}$Ta$_{0.5}$ in a magnetic field. This is reprinted from the paper by Kim et al[1]. The Lorentz force must overcome the pinning force before there is any dissipation.
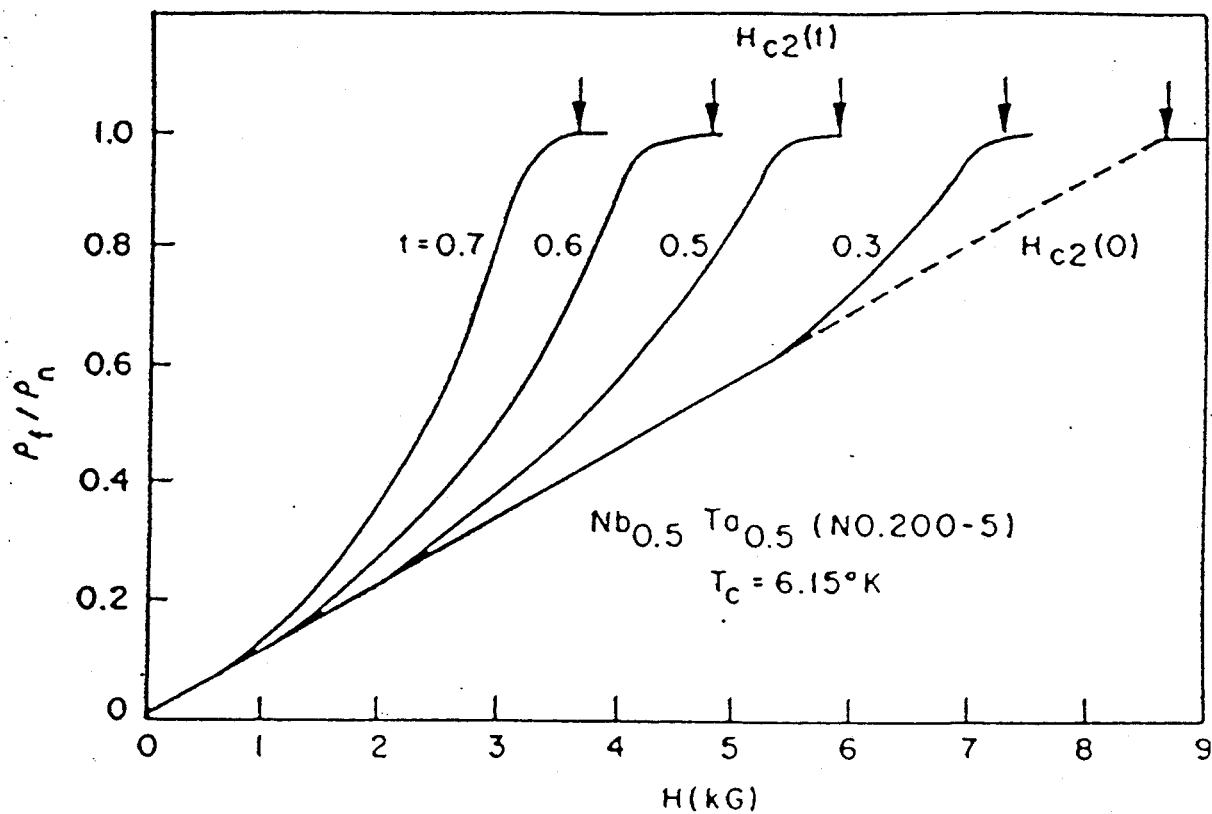
Figure 3.3: Normalized flux-flow resistivity vs. magnetic field for Nb$_{0.5}$Ta$_{0.5}$. This is reprinted from the paper by Kim et al [1]. At low temperatures and fields, the data obeys the empirical law $\rho_{ff}/\rho_n = H/H_{c_2}(0)$.

Another phenomenon observed[1] for high-field superconducting alloys ($\kappa \sim 10-100$) such as NbZr, NbTi and VTi. was the paramagnetic effect on ρ_{ff} . The effect is due to alignment of the electron spins along the direction of the applied magnetic field. This lowers the free energy of the corresponding normal state by $\chi_n H^2/2$ (where χ_n is the normal state susceptibility) and leads to a transition into the normal state as the field is increased even for $H < H_{c_2}$ once this energy reduction becomes comparable to the gap energy. What Kim et al found was that the empirical relation 3.53 holds not for the actual H_{c_2} (0) but rather from the $H_{c_2}{}^*(0)$ that we would calculate based on the Ginzburg-Landau theory in the absence of the paramagnetic effect. Since it is $H/H_{c_2}{}^*(0)$ and not $H/H_{c_2}(0)$ that represents the volume fraction of normal material, it is intuitively appealing that it is the latter ratio which appears in the equation 3.53. However, to be totally consistent, it is $H/H_{c_2}(T)$ (for a given temperature) and not $H/H_{c_2}(0)$ that represent the volume fraction of normal material. Rather, we might have expected

$$\frac{\rho_{ff}}{\rho_n} = \frac{H}{H_{c_2}(T)} \tag{3.54}$$

as can actually be derived from the Bardeen-Stephen model for $T \rightarrow T_c$.

Behaviour more in line with equation 3.54 was actually seen in later dc experiments on a Pb$_{0.76}$In$_{0.24}$ alloy by Fogel et al[3], see figure 3.4. Reasonable agreement with equation 3.54 was seen for $H/H_{c_2}(T) < 0.5$ above which ρ_{ff}/ρ_n increases more rapidly as it crosses over in to the normal state (slightly anomalous behaviour is seen close to the origin, however). In fact, Fogel claims that, based on a re-examination of all existing data at that time, there are departures from the empirical relation of Kim et al[1] for all conventional type-II superconductors!

We now turn to the experiments performed at high frequencies. Central to these experiments was the early work of Gittleman and Rosenblum[4, 5]. They found that the flux-flow state is accessible for high-frequency transport currents even with $J \ll J_c$ as
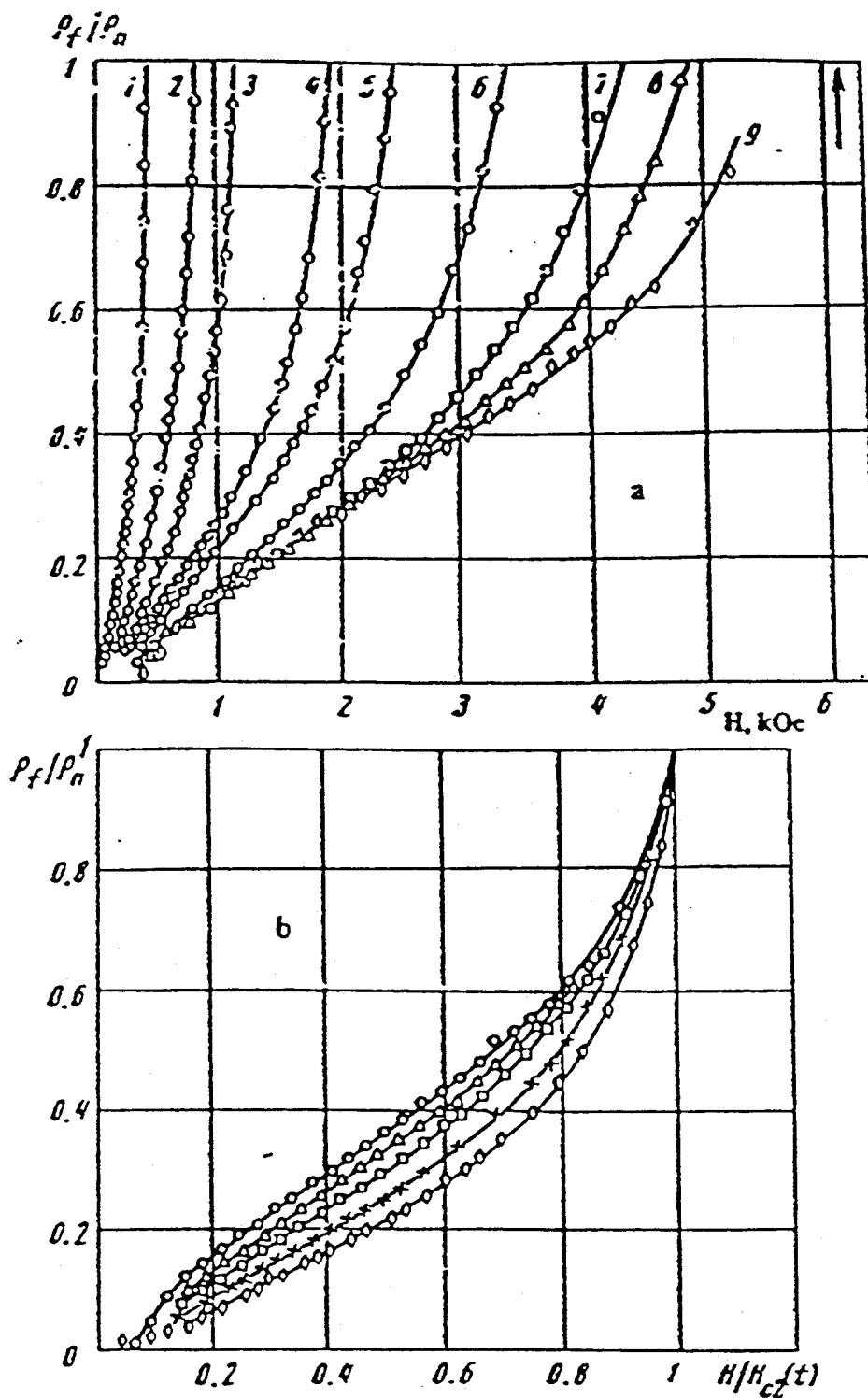
Figure 3.4: Normalized flux-flow resistivity vs. field and reduced field: PbIn. This is reprinted from the paper by Fogel [3]. The different curves represent field sweeps at different temperatures — the higher numbers represent lower temperatures. It is the temperature dependent H_{c_2} that seems to be the relevant parameter for scaling the data.

SAMPLE	f_0 (mcs) MEAS.	f_{oc} (mcs) CALC.	f_{op} (mcs) CALC.
Δ PbIn—1.7°K	3.9	7.0	2.2
O PbIn—1.7°K	5.1	12.0	3.8
X NbTa—4.2°K	15	49	15.6
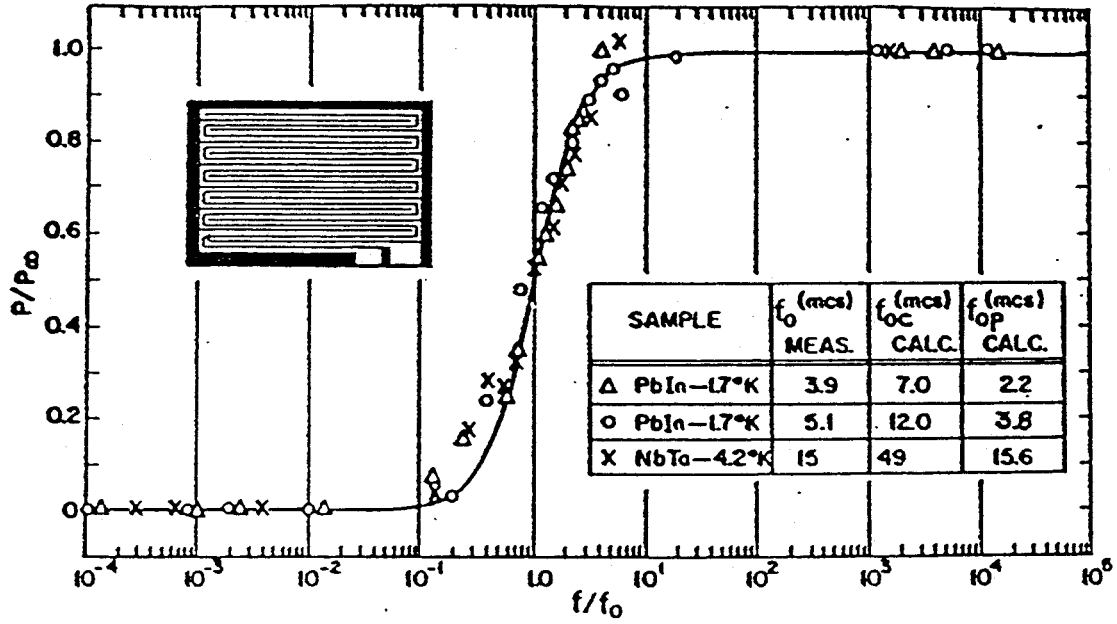
Figure 3.5: Frequency dependent crossover from a flux-pinned to a flux-flow state for some conventional superconducting alloys. This graph is reprinted from the paper by Gittleman and Rosenblum[4, 5]. It shows that above the characteristic pinning frequency, $\omega_p = \kappa_p/\eta$, the superconductor acts as if it were totally unpinned.

long as the frequency is greater than the so-called *pinning frequency*, $\omega_p = \kappa_p/\eta$ where κ_p is an effective pinning force constant, see figure 3.5. For $\omega \gg \omega_p$, the material acts like an ideal, defect-free material with the vortices totally unpinned. Their picture of the dynamics is of a vortex sitting at the minimum of a pinning potential energy well which, close to the minimum, can be thought of as a parabola $\kappa x^2/2$. If the vortex is acted on by the viscous retarding force $\eta v = \eta \dot{x}$ and the Lorentz force $J\Phi_0$ in the opposite direction, we can write down an equation of motion for the vortex

$$m_v \ddot{x} = -\kappa_p x - \eta \dot{x} + J \Phi_0 \qquad (3.55)$$

where m_v is the effective mass of the vortex. This mass term is typically thought to be negligible[58]. If we write $J = J_0 e^{i\omega t}$ and $\dot{x} = \dot{x}_0 e^{i\omega t} = v_0 e^{i\omega t}$, we can solve for J_0 in the

above equation

$$J_0 = \frac{v_0}{\Phi_0}\left(\eta - i\,\frac{\kappa_p}{\omega}\right) \tag{3.56}$$

Since $E_0 = v_0 B$ (see equation 3.1), we get for the effective ac resistivity

$$\rho_{eff} = \frac{E_0}{J_0} = \frac{\Phi_0\,B}{\eta\,(1 - i\,\omega_p/\omega)} \tag{3.57}$$

For $\omega \ll \omega_p$, ρ_{eff} becomes purely imaginary and there is no energy dissipation. For $\omega \gg \omega_p$,

$$\rho_{eff} = \rho_{ff} = \frac{\Phi_0\,B}{\eta} \tag{3.58}$$

the pure flux-flow resistivity that would be measured directly in a dc experiment. An example of the transition from the flux-pinned to the flux-flow regime is shown in figure 3.5. It can be seen from the values of f_0 in this figure (3.9–15 MHz) that at microwave frequencies their samples are well in to the flux-flow limit. This result has been understood as follows: at high enough frequencies, the vortex spends the entire cycle of the rf field in the neighbourhood of the potential minimum (where the restoring force, $\kappa_p x$, is very small); therefore, the vortex only samples that part of the pinning potential which is essentially flat, and thus it responds as if it were totally unpinned. In fact, this argument is flawed in that it implies a dependence upon the amplitude of the motion. We can see from equation 3.55 that this is not so: the effective viscous force increases proportional to the frequency and will eventually dominate the pinning force at high enough frequencies.

These observations about the vortex dynamics were later confirmed and investigated in more detail by Le Gilchrist and Monceau[6, 7, 8] who found that the rf response was virtually unaffected by pinning for frequencies greater than 1 MHz for appropriately prepared samples of PbIn, NbTa and Nb. To relate the flux-flow resistivity to the surface resistance, they used the expression

$$\frac{R_s(B)}{R_n} = \left(\frac{\rho_{ff}}{\rho_n}\right)^{1/2}. \tag{3.59}$$

The reasoning was as follows: if the classical skin effect expression applies to the mixed state as well as the normal state, then

$$R_s(B) = \left(\frac{\rho_{ff}\,\mu_0\,\omega}{2}\right)^{1/2} \tag{3.60}$$

and

$$R_n = \left(\frac{\rho_n\,\mu_0\,\omega}{2}\right)^{1/2}, \tag{3.61}$$

and dividing these two equations, we get equation 3.59. The classical skin effect theory might be expected to apply if the skin depth, δ, of the rf currents in the mixed state are large compared to all the length parameters that characterize the mixed state such as λ, a (the vortex lattice parameter), and ξ (the coherence length). λ is typically the largest of these. If the skin-effect theory is approximately correct and $\rho_{ff}/\rho_n \sim H/H_{c_2}$ then

$$\delta = \sqrt{\frac{2\,\rho_n}{\mu_0\,\omega}\frac{H}{H_{c_2}}} = \sqrt{\frac{H}{H_{c_2}}}\,\delta_n \tag{3.62}$$

Using $\delta_n \sim 3 \times 10^{-4}$ cm and $\lambda \sim 10^{-5}$ cm, then

$$\frac{\lambda}{\delta} = \frac{\lambda}{\delta_n}\sqrt{\frac{H_{c_2}}{H}} = 0.03\sqrt{\frac{H_{c_2}}{H}} \tag{3.63}$$

which is small except for H close to zero. The field dependence of R_s/R_n and ρ_{ff}/ρ_n is shown in figure 3.6. The latter is obtained by squaring the former (in accordance with equation 3.59). As can be seen from the plots, they also made measurements at dc and the results are plotted on the surface resistance plot. The agreement is quite good and confirms that at high frequency, the ideal flux-flow state is recovered. At low fields, the data seem to scale with a temperature independent H_{c_2} in qualitative agreement with Kim et al[1].
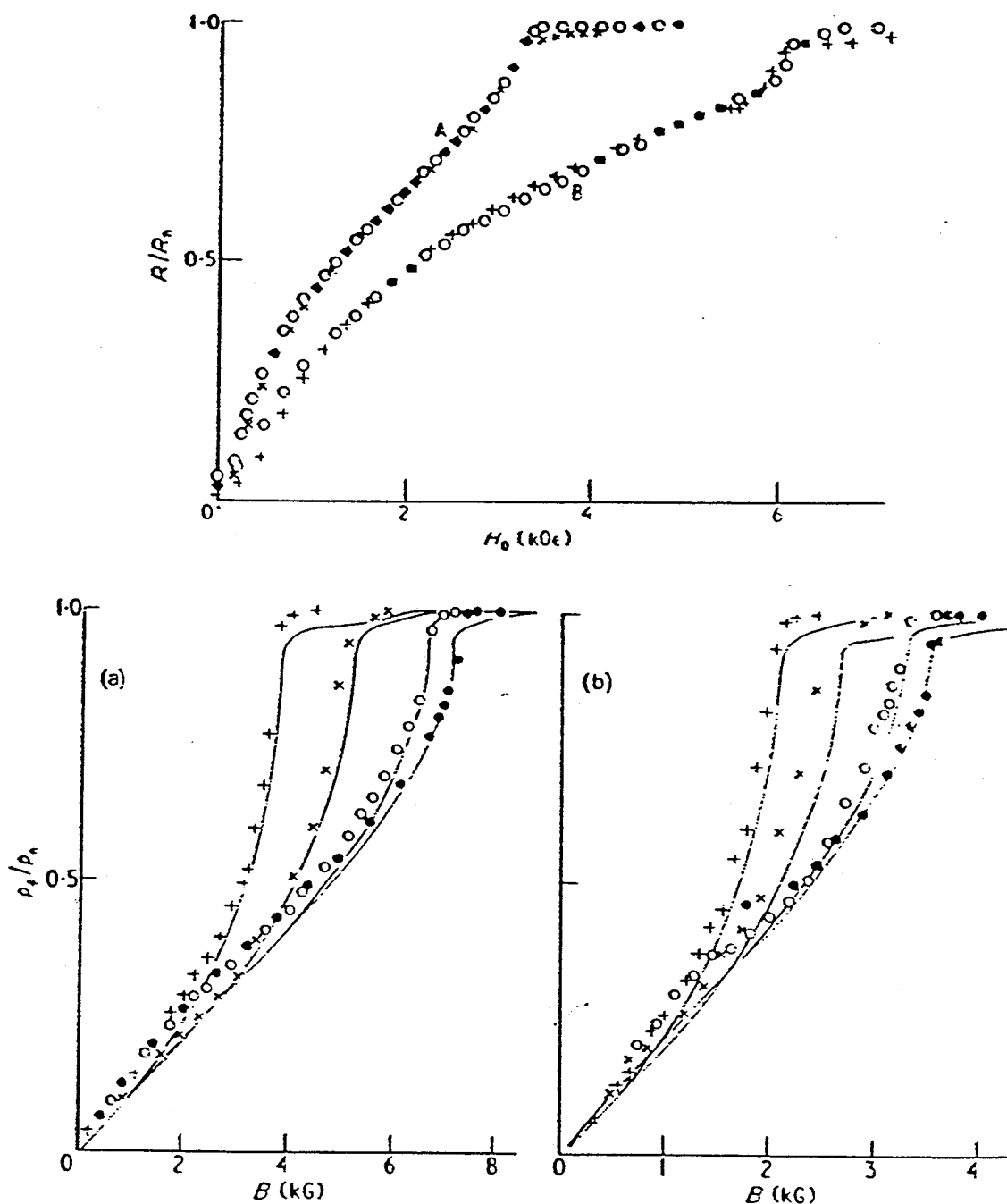
Figure 3.6: Microwave determination of ρ_{ff} in conventional superconductors. These figures are reprinted from the paper by Gilchrist and Monceau[8]. The upper figure shows R_s and the lower figures ρ_{ff} extracted using equation 3.59. In the lower figure, the smooth curves are obtained from the microwave data and the discrete points are from dc measurements of the differential resistivity.

3.6 Theory of Flux Flow Resistivity in High-T$_c$ Superconductors

3.6.1 Surface Impedance in the Mixed State

The advent of high-T_c superconductors has stimulated considerable new work on deriving more general expressions[28, 59] for the surface impedance of a superconductor in the mixed state. Coffey and Clem[28, 29], in particular, propose a solution to the surface impedance problem taking into account the vortex viscosity, pinning, thermally activated flux motion and contribution of the normal fluid from the bulk of the superconductor. They consider the response of the superconductor in the mixed state to an applied ac field, **b**, parallel to the surface along the z-axis. In the simplest version of their theory, the superconductor is taken to occupy the half-space $x > 0$. They treat the problem of a static field $H \gg H_{c_1}$ applied parallel to the z-axis. This establishes the flux lattice corresponding to an average field $B_0 = n\Phi_0 = H/\mu_0$ (where n is the number of vortices per unit area); the amplitude of the rf driving field is small, $b = \mu_0 h \ll B_0$. The theory also assumes $B/\mu_0 \gg H_{c_1}$ which implies that the vortex lattice parameter, a_0, is much less than the penetration depth, λ_L. The surface impedance is given by

$$Z_s = i\,\omega\,\mu_0\,\tilde{\lambda}(\omega, B, T) \tag{3.64}$$

where $\tilde{\lambda}$ is the effective skin depth and is in general complex. The ac **b** field gives rise to oscillating supercurrents that shake the vortices in their pinning potential wells and carry field perturbations farther into the superconductor than, say, simply the London penetration depth. The approach is basically two-fluid in nature with

$$\mathbf{J} = \mathbf{J_n} + \mathbf{J_s} \tag{3.65}$$

where

$$\mathbf{J_n} = \sigma_1\,\mathbf{E} \tag{3.66}$$

(σ_1 is the real part of the conductivity due to the normal fluid) and $\mathbf{J_s}$ is given by a modified second London equation

$$\nabla \times \mathbf{J_s} = -(\mu_0 \, \lambda_L^2)^{-1} \, (\mathbf{B} - \Phi_0 \, n \, \hat{\alpha}) \tag{3.67}$$

($\hat{\alpha}$ is a unit vector in the direction of the field in the core of a vortex). This equation takes into account variations in the flux density from the average, macroscopic value and can be seen as a generalization of the equation for the current and field distribution about a single vortex[34]

$$\mu_0 \, \lambda_L^2 \, \nabla \times \mathbf{J_s} + B = \Phi_0 \, \delta_2(\mathbf{r}) \, \hat{\alpha} \; . \tag{3.68}$$

They supplement these equations by an equation of motion for the vortex identical to the one assumed by Gittleman and Rosenblum

$$\eta \, \dot{\mathbf{u}}(\mathbf{r}, t) + \kappa_p \, \mathbf{u}(\mathbf{r}, t) = \mathbf{J} \times \Phi_0 \, \hat{\alpha} \tag{3.69}$$

(they ignore the possibility of Hall fields here) where the forces in this equation are per unit length of vortex. The vortex displacement from its equilibrium position, $\mathbf{u}(\mathbf{r}, t)$, and its velocity, $\dot{\mathbf{u}}(\mathbf{r}, t)$, are both dependent on position, here, because the ac fields decay inside the superconductor due to screening — deep inside the superconductor, $\mathbf{u} = \dot{\mathbf{u}} = 0$. Using the ansatz,

$$\mathbf{u} = \hat{\mathbf{x}} \, u_0 \, e^{-x/\tilde{\lambda}} \, e^{i\omega t} \tag{3.70}$$

for the vortex displacement and ignoring (for the moment) thermally activated flux motion, they derive the following expression for $\tilde{\lambda}$

$$\tilde{\lambda}(\omega, B, T) = \left[\frac{\lambda_L^2(B, T) - i/2 \, \tilde{\delta}_v^2(\omega, B, T)}{1 + 2 \, i \, \lambda_L^2(B, T)/\delta_{nf}^2(\omega, B, T)} \right]^{1/2} \tag{3.71}$$

$\lambda_L(B, T)$ is the temperature and field dependent London penetration depth, $\tilde{\delta}_v$ is given by

$$\tilde{\delta}_v^2 = \frac{2 \, \tilde{\rho}_v}{\mu_0 \, \omega} \quad ; \quad \tilde{\rho}_v = \frac{\Phi_0 \, B}{\eta \, (1 - i \, \omega_p/\omega)} \tag{3.72}$$

($\omega_p = \kappa_p/\eta$ is the pinning frequency as before) and δ_{nf} is the normal state skin depth coming from the normal fluid

$$\delta_{nf}^2 = \frac{2}{\mu_0 \sigma_1 \omega} \qquad (3.73)$$

They also showed [29] that for the slab geometry, we get the same expression for $\tilde{\lambda}$ whether the static field is strictly perpendicular or parallel to the broad faces of the slab (provided that the rf $\mathbf{f}$ field is parallel to $\mathbf{B_0}$ in the latter case).

As $T \to T_c$ or $H \to H_{c_2}$, $\lambda_L(B,T)$ diverges and $\tilde{\lambda}$ becomes

$$\tilde{\lambda} = \left[\frac{\delta_{nf}^2}{2\,i} \right]^{1/2} = \frac{\delta_{nf}}{2}\,(1 - i) \qquad (3.74)$$

and so for the surface resistance we get

$$R_s = \mathrm{Re}\,(i\,\omega\,\mu_0\,\tilde{\lambda}) = \frac{\omega\,\mu_0\,\delta_{nf}}{2} = \sqrt{\frac{\rho_n\,\mu_0\,\omega}{2}} \qquad (3.75)$$

which is the expression for the surface resistance of a metal in the normal state. In zero field, the δ_{nf} term is an essential part of the physics: setting $\tilde{\delta}_v$ to zero, equation 3.71 becomes

$$\tilde{\lambda} = \left[\frac{1}{1/\lambda_L^2 + i\,\mu_0\,\sigma_{nf}\,\omega} \right]^{1/2} \qquad (3.76)$$

and so the expression for the surface impedance is

$$Z_s = i\,\omega\,\mu_0\,\tilde{\lambda} = \left[\frac{i\,\omega\,\mu_0}{\tilde{\sigma}} \right]^{1/2} = \left[\frac{i\,\omega\,\mu_0}{\sigma_{nf} - \frac{i}{\mu_0\,\omega\,\lambda_L^2}} \right]^{1/2} \qquad (3.77)$$

where $\tilde{\sigma}$ is the previously discussed generalized two-fluid expression for the complex conductivity of a superconductor in zero field.

At finite fields, the term including δ_{nf} in the denominator of the expression in equation 3.71 is, practically speaking, rather unimportant apart from the above limiting behaviour. This is because $(\lambda_L/\delta_{nf})^2 \ll 1$ except very close to H_{c_2} or T_c . Therefore, over most of the range of temperatures and fields of interest

$$\tilde{\lambda} = \left[\lambda_L^2 - \frac{i}{2}\,\tilde{\delta}_v^2 \right]^{1/2} \qquad (3.78)$$

An important observation is that for $\lambda_L^2/\tilde{\delta}_v^2 \ll 1$ (and typically this is a good approximation especially for frequencies of the order of a few GHz) $\tilde{\lambda} \propto B^{1/2}$ and in particular $R_s \propto B^{1/2}$ *no matter how strong the pinning* as long as the η and ω_p are independent of the field. For $\omega \gg \omega_p$ (free flux-flow limit), equation 3.78 becomes

$$\tilde{\lambda} = \left[\lambda_L^2 - i\frac{\Phi_0 B}{\mu_0 \omega \eta}\right]^{1/2} = \left[\lambda_L^2 - \frac{i}{2}\delta_{ff}^2\right]^{1/2} \tag{3.79}$$

where δ_{ff} is the free flux-flow skin depth. If $\lambda_L^2/\delta_{ff} \ll 1$ i.e. flux-flow skin depth much larger than the London penetration depth, then

$$\tilde{\lambda} = \left[-i\frac{\Phi_0 B}{\mu_0 \omega \eta}\right]^{1/2} = \left[-i\frac{\rho_{ff}}{\mu_0 \omega}\right]^{1/2} \tag{3.80}$$

and so proceeding as before, we get

$$R_s = \left(\frac{\rho_{ff}\mu_0\omega}{2}\right)^{1/2} . \tag{3.81}$$

Thus, to the extent that we can ignore the London penetration depth term, the superconductor acts like an effective metal with resistivity ρ_{ff}. We can also see that this is the approximation used in analyzing the flux-flow microwave experiments on conventional superconductors.

Equation 3.71 can be generalized to take into account thermally activated flux motion. This necessitates introducing an additional parameter U_0 which corresponds to an energy barrier height to thermal hopping of vortices between adjacent pinning sites. The modified expression for $\tilde{\rho}_v$ is

$$\frac{\tilde{\rho}_v(\omega)}{\rho_{ff}} = \frac{\epsilon + (\omega\tau)^2 + i(1-\epsilon)\omega\tau}{1 + (\omega\tau)^2} \tag{3.82}$$

where

$$\epsilon = \frac{1}{I_0^2(\nu)} \;,\; \tau = \frac{\eta}{\kappa_p}\frac{I_0^2(\nu) - 1}{I_1(\nu)I_0(\nu)} \;,\; \text{and } \nu = \frac{U_0}{k_B T} \;. \tag{3.83}$$
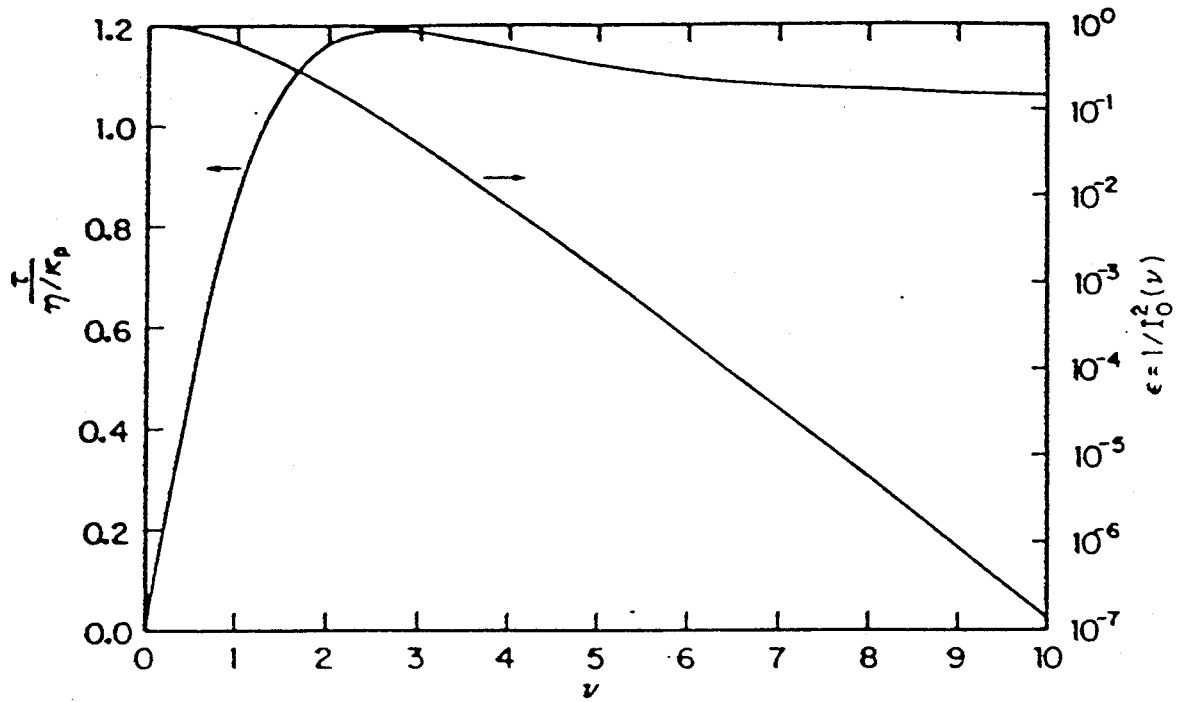
Figure 3.7: ν dependence of parameters in the Coffey-Clem model. This is reprinted from the paper Coffey and Clem[28].

The I_p are modified Bessel functions of the first kind of order p. The ν dependence of ϵ and $\tau\omega_p$ are shown in figure 3.7. For low temperatures or large activation energies, U_0, $\nu \gg 1$ and so $\tau\omega_p \to 1$ and $\epsilon \to 0$ and so equation 3.82 becomes

$$\frac{\tilde{\rho}_v(\omega)}{\rho_{ff}} = \frac{(\omega/\omega_p)^2 + i\,(\omega/\omega_p)}{1 + (\omega/\omega_p)^2} = i\,\frac{\omega}{\omega_p + i\,\omega}\,. \tag{3.84}$$

In the limit, $\omega \gg \omega_p$, the RHS is simply equal to 1 and we recover the result for free flux-flow that we had in the absence of any thermal activation. In the high T or low U_0 limit, $\epsilon \to 1$, and equation 3.82 becomes

$$\frac{\tilde{\rho}_v(\omega)}{\rho_{ff}} = \frac{1 + (\omega\,\tau)^2 + 0}{1 + (\omega\,\tau)^2} = 1 \tag{3.85}$$

and we again recover the free flux-flow result independent of how the operating frequency compares to the pinning frequency. It is important to understand the distinction between these two ways (for small driving currents) of achieving free flux-flow. At low enough frequencies ($\omega \ll \omega_p$), $\tilde{\rho}_v \to \rho_{ff}$ provided $U_0 \ll k_BT$. At high enough frequencies, ($\omega \gg \omega_p$) we get free flux-flow even for $U_0 \gg k_BT$. Thus the shift of the irreversibility line to *higher* fields and temperatures as we *increase* the frequency (see Chapter 2) is undoubtedly related to thermally activated flux motion. At very high frequencies, thermal hopping of vortices is inhibited but we recover free flux-flow again because the vortices are spending all of their time in the essentially flat bottom of the pinning potential well. When we come to use the Coffey-Clem theory, we shall set $U_0/k_BT \gg 1$ and neglect thermal hopping entirely.

Coffey et al[60, 61] have also investigated the size of the vortex inertial mass term (finding results qualitatively similar to those calculated previously by Suhl[58]). They estimate that for T close to T_c

$$m_v(T) = \epsilon_0\,\Phi_0\,B_{c_2}(T)\,. \tag{3.86}$$

Using the expression from Chapter 2 for H_{c_2} , we find that at, say, $t \sim 0.96$, $B_{c_2} = 6.6T$. From equation 3.86, we find that $m_v \sim 10^{-25}$kg/m. If we include a mass term $m_v \ddot{u}$ in the equation of motion for the vortex, the resulting resistivity is

$$\tilde{\rho}_v = \frac{\Phi_0 \, B}{\eta \left(1 - i\,\omega\,m_v/\eta + i\,\omega_p/\omega \right)} \tag{3.87}$$

and so $\eta/m_v = \omega_m$ defines another characteristic frequency. Using the Bardeen-Stephen formula we can estimate η at $t \sim 0.96$ to be $\sim 10^{-7}$. This gives

$$\omega_m = \frac{10^{-7}}{10^{-25}} = 10^{18} \tag{3.88}$$

At microwave frequencies of the order of 30 GHz, $\omega \sim 2 \times 10^{11}$ and so $\omega/\omega_m \sim 10^{-7}$ [3]. It seems likely, therefore, that the effect of the vortex mass is not significant at the frequencies of interest. In the subsequent analysis, we shall ignore it.

3.6.2 Microscopic description of vortex motion in terms of core states

Hsu[22, 23] has modelled vortex motion microscopically in the low temperature, low field, clean, extreme type-II limit in terms of the quasiparticle states inside the vortex. As we have already briefly mentioned, the nature of these states was first elucidated by Caroli, de Gennes and Matricon for conventional type-II superconductors who showed that there is a spectrum of energy levels for quasiparticle excitations localized inside the vortex with a very small energy gap given by[4] $\Omega_0 = \Delta^2/E_F$ ($\sim$1mK for conventional superconductors). For high-T_c materials this is estimated to be $\sim$ 10K and thus it is

---

[3]Coffey and Clem also treat the case of a layered superconductor and are able to derive a low temperature expression for the inertial mass of a vortex parallel to the planes. They find $m_v \sim 3 \times 10^{-22}$kg/m for YBa$_2Cu_3O_{7-\delta}$ — over 100 times bigger than the estimate given above. At low temperature, $\eta \geq 10^{-6}$ (using the Bardeen Stephen formula) and this gives $\omega_m \sim 4 \times 10^{15}$. Thus, $\omega/\omega_m \sim 10^{-4}$ and we still find that the effect of the mass term is not important at frequencies $\sim$ 30 GHz.

[4]This energy gap can be estimated by considering the energy levels of a particle confined to a box of radius ξ. The lowest level has energy $\sim \hbar^2/m\xi^2$. Using $\xi \sim \hbar v_F/\Delta$[34] and $E_F \sim mv_F^2$, we find $\delta E \sim \Delta^2/E_F$.

important to understand what effect such a relatively large spacing might have on the dynamics of moving vortices.

Hsu uses the Bogoliubov-de Gennes equations for s-wave superconductors and supplements them with a local gap equation. He considers the response of a vortex to a uniform time-varying electromagnetic wave and finds that the time evolution of the quasiparticle states in the vortex corresponds to vortex motion provided that the velocity involved is small. A nice feature of the equations is that for a clean system with no pinning and no dissipation the vortex moves along with the background superfluid as we would expect (see section 1.2.2). He is able to derive an equation of motion for the vortex including a dissipation term which is characterized by the lifetime, τ, of the low energy quasiparticle states. The dissipation due to a single moving vortex is calculated and in the limit as $\Omega_0 \to 0$ a core resistivity corresponding to

$$\frac{\rho_{ff}}{\rho_n} = \frac{H}{H_{c_2}} \tag{3.89}$$

is recovered. This is roughly consistent, then, with the experimental work on conventional superconductors where Ω_0 is small. For finite Ω_0 (and for a given polarization of the electromagnetic wave) there is an antiresonance in the dissipation at $\omega = \Omega_0$. The resulting conductivity has a shallow minimum near $\omega \sim \Omega_0$ corresponding to this antiresonance. For high-T_c superconductors, these features are probably located at much higher frequencies than the maximum frequency used for the measurements in this thesis. In the limit as $\omega \to 0$, $\Omega_0 \tau \to \infty$ and $H/H_{c_2} \to 0$ equation 3.89 is again recovered. However, it is not obvious that this clean limit applies to $YBa_2Cu_3O_{6.95}$: in the normal state $\tau \sim 10^{-14}$ sec while $\Omega_0 \sim 2 \times 10^{11}$. Even if we allow for a one hundred fold increase in τ below T_c , the clean limit seems of doubtful validity. This work is sensitive to the nature of pairing and the effects of a gapless superconductor on the microscopic structure of the vortex have yet to be calculated. Nevertheless, it seems that Hsu's approach is the best

starting point for a complete understanding of vortex motion in high-T$_c$ superconductors.

3.7 Experimental work on YBa$_2$Cu$_3$O$_{7-\delta}$

There has not been a great deal of experimental work done that directly addresses the question of the temperature and field dependence of the flux-flow resistivity. The common tendency is simply to assume that $\rho_{ff}/\rho_n = H/H_{c_2}(T)$ or $\rho_{ff}/\rho_n = H/H_{c_2}(0)$ and ignore the question of what is the most appropriate value for ρ_n below T_c . To our knowledge, the only real attempt to directly measure this quantity in high quality samples has been by Kunchur et al[25] who worked with c-axis oriented epitaxial films of YBa$_2$Cu$_3$O$_{7-\delta}$. They take a novel approach by supplying a pulsed transport current density comparable to the depinning critical current density (10^6A/cm^2). Nevertheless, they were still restricted to measurements close to the irreversibility line and above. The films had T$_c$'s of 88.5K and 91.1K and the lowest temperature measured was 76K. Lower temperatures required excessively high current densities. They found good agreement with the Bardeen-Stephen formula

$$\frac{\rho_{ff}}{\rho_n(T)} = \frac{H}{H_{c_2}(T)} \tag{3.90}$$

with $\rho_n(T)$ obtained by a linear extrapolation of the linear resistivity from above T_c and

$$H_{c_2}(T) = \frac{dH_{c_2}}{dT}(T_c - T) \tag{3.91}$$

was obtained as a fitting parameter. Values for $dH_{c_2}/dT|_{T_c}$ were 1.85T/K and 2.2T/K in good agreement with values obtained from the literature[26]. They argue that this result points to the conventional nature of flux-flow in the high-T$_c$ materials. However, they have only checked the Bardeen-Stephen formula down to $t \sim 0.84$ which leaves open the question of the low temperature behaviour. Also there is some question as to how much YBa$_2$Cu$_3$O$_{7-\delta}$ films are affected by intrinsic defects such as grain boundaries

which might create superconducting weak links, i.e. it is unclear how meaningful it is to compare thin-film and single crystal data.

Owliaei et al[62] have studied YBa$_2$Cu$_3$O$_{7-\delta}$ epitaxial films at microwave frequencies. Figure 3.8 shows their surface resistance data at 10 GHz in magnetic fields up to 7T. It is clear that by 65K the surface resistance has decreased to a value close to zero. They claim to see a crossover as a function of magnetic field and extract η and κ_p within the framework of the Coffey-Clem theory from the field profiles in the temperature range 78K to 85K. They find a pinning frequency that increases from 3 to 15GHz from 85K to 78K and a viscosity that increases rapidly in this temperature range. They assume equation 3.90 with $\mu_0 H_{c_2}(T) = 115(1 - t)$ T and find a $\rho_n(T)$ that decreases roughly linearly with temperature but which extrapolates to 0 by about 75K. Again, it is unclear what effect the defect structure has on the surface resistance in a magnetic field.

Marcon et al[63] have performed even higher frequency measurements (23 and 48 GHz) in an attempt to deduce information about the vortex viscosity. Unfortunately, the samples used were not single crystals or films but ceramic samples. The microwave response of such materials are usually dominated by grain boundary effects such as superconducting weak links and other sources of anomalous loss associated with the granular nature of the material.

That a single pinning frequency model governed by an equation of motion such as equation 3.55 (the Gittleman and Rosenblum or Coffey-Clem models for example) is probably not true in detail is indicated by the swept frequency measurements (1–600 MHz) of the impedance of c-axis oriented epitaxial thin films of YBa$_2$Cu$_3$O$_{7-\delta}$ by Wu et al[64]. Their technique allows them to extract the complex resistivity very simply from the impedance data in a model independent way. They found in the field range (0.5–8T) and the temperature range (80–86K) that their data was consistent with a vortex glass to vortex liquid transition[65, 66] characterized by a critical field H_g. Away from
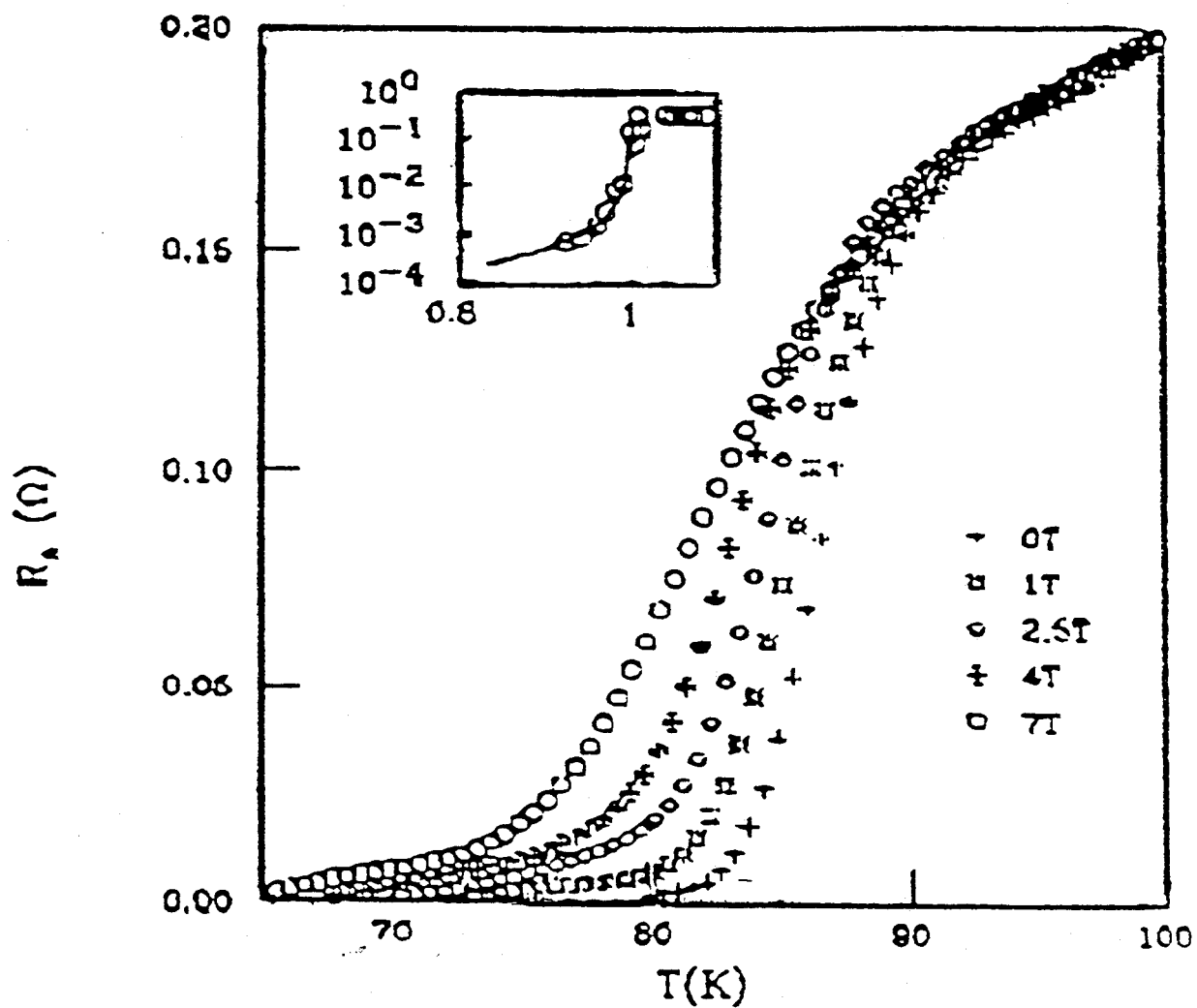
Figure 3.8: R_s at 10 GHz in a magnetic field in a $YBa_2Cu_3O_{7-\delta}$ thin film. This is reprinted from the paper by Owliaei et al[62].

the transition line, the frequency dependence of the phase angle was consistent with the scaling model of Fisher, Fisher and Huse[67, 68] rather than the more simple behaviour predicted by an equation such as 3.55.

Chapter 4

The Microwave Experiment

In this chapter, we describe in some detail the experimental apparatus used to make the surface resistance measurements on the single crystals of $YBa_2Cu_3O_{6.95}$. We first quickly review the basics of resonant cavities and then describe the principles of cavity perturbation. Since, the data presented later in this work was taken at three distinct frequencies, we describe in detail the so-called split-ring resonator used to make the 5.4 GHz measurements and the right circular cylindrical cavities used to make the higher frequency measurements at 27 and 35 GHz. Finally, we discuss the overall design of the two cryostats used to house the low and higher frequency resonators. The heart of the design is the *probe* at the end of which the sample is mounted; this piece of apparatus is common to both the low and high frequency cryostats.

4.1 The Resonant Cavity / Cavity Perturbation

A resonant cavity is often modelled as an RLC circuit, the resonant frequency of a mode in the cavity being thought of as the resonant frequency of the corresponding circuit. Just as for the circuit, if we sweep through the resonant frequency in the cavity, the absorbed power has a Lorentzian line shape. The resonant frequency, f_0, and the quality factor, Q, can both be determined from the Lorentzian line shape, f_0 being the frequency at the peak of the line shape and

$$Q = \frac{f_0}{\Delta f} \qquad (4.1)$$

where Δf if the full width at half maximum power. The Q of the mode is also given by

$$Q = 2\pi \left(\frac{\text{energy stored}}{\text{energy dissipated per cycle}} \right). \tag{4.2}$$

It is clear from this equation that $1/Q$ is proportional to the power dissipated in the cavity.

A real cavity has many resonant modes some of which are degenerate. Consider a single non-degenerate mode far enough in frequency from all other modes so as to be unaffected by them. As we have already seen, $1/Q$ is a measure of the power dissipation inside the cavity; in an empty cavity, it will be due to the energy losses in the walls of the cavity plus the losses due to the coupling holes which are needed to couple microwave power into and out of the cavity. Thus, the Q of the cavity can be written as

$$\frac{1}{Q} = \frac{1}{Q_0} + \frac{1}{Q_c} \tag{4.3}$$

where Q_0 is the intrinsic Q of the cavity and Q_c is the coupling Q. It is clear that if we introduce a sample into the cavity, then we will get another term in the above equation due to the power dissipation in the sample,

$$\frac{1}{Q} = \frac{1}{Q_0} + \frac{1}{Q_c} + \frac{1}{Q_s}. \tag{4.4}$$

We can therefore measure the loss in the sample by measuring the change in the $1/Q$ after inserting the sample

$$\Delta(1/Q) = \frac{1}{Q_s} \propto \text{power dissipation in the sample.} \tag{4.5}$$

The proviso here is that the sample is only a small perturbation of the rf fields in the cavity. If the change in the geometry of the fields due to the insertion of the sample is not small then the modified fields at the walls and at the coupling holes will give rise to different wall and coupling losses. Consequently, the terms $1/Q_0$ and $1/Q_c$ in equations

4.3 and 4.4 can no longer be considered constant when we perform the subtraction to get $1/Q_s$. The net effect is to introduce systematic error into the measurement of the sample losses. The essence of the cavity perturbation technique, therefore, is to introduce a sample whose losses are large enough to be measurable but whose effect on the overall field configuration is negligible.

From Appendix A, we know that the surface resistance, R_s, of a sample is proportional to the power dissipated per unit area, or explicitly

$$P_A = \frac{1}{2} R_s |H_0|^2. \qquad (4.6)$$

Therefore, we know that

$$R_s \propto P_A \propto \Delta(1/Q) \quad \text{or} \quad R_s = C\,\Delta(1/Q) \qquad (4.7)$$

where C is a calibration constant. Once we have measured $\Delta(1/Q)$, the task of finding R_s is reduced to determining the calibration constant. For some standard cavities and samples of particularly convenient shape, C can be calculated. However, much of the time this is not possible, and we are left with two options: we can set the sample at a temperature where we know the dc resistivity and (providing the sample is metallic and sufficiently thick) use the expression

$$R_s = \left(\frac{\rho_{\mathrm{dc}}\,\mu_0\,\omega}{2}\right)^{1/2} \qquad (4.8)$$

to find R_s at that temperature. If the dc resistivity of the high-T_c sample is not known, or, if for any reason, the simple skin effect formula is not applicable, we can measure $\Delta(1/Q)$ for an appropriate reference sample of the same dimensions as the sample of interest.
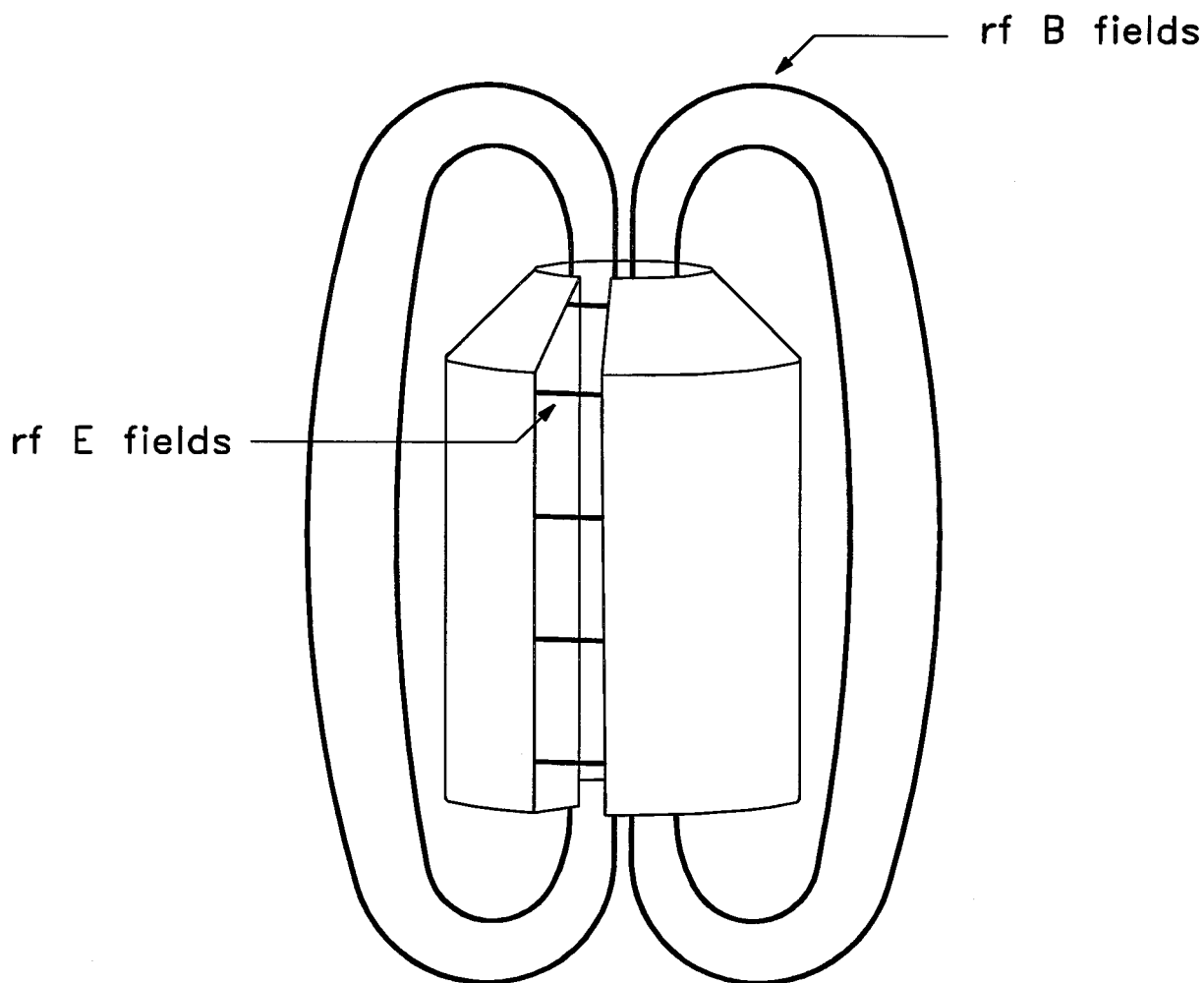
Figure 4.1: Split-ring resonator and field geometry.

4.2 The Split-Ring Resonator

The measurements at 5.4 GHz were made with a so-called *split-ring resonator*[69, 70] shown in figure 4.1. In principle, it is a single-turn inductor tuned by the capacitance of the gap. The mode of interest is shown in the figure. It consists of axial B fields (except where the field lines turn around at the ends of the resonator) and E fields everywhere perpendicular to the resonator axis and for the most part confined to the gap. The resonant frequency of this mode depends primarily on the gap thickness and the radius

of the central bore of the resonator. It is a relatively simple procedure to machine the resonator from oxygen free high conductivity (OFHC) copper and then use a spark erosion machine to cut the gap to the desired thickness. Typically, the resonator sits on a support structure within an outer cylinder which is beyond cutoff for the mode of interest. Figure 4.2 shows the arrangement used in the 5.4 GHz measurements. Particularly for high frequencies, this outer cylinder helps to confine the fields and to maintain a high Q. The main advantage of the split-ring resonator over a conventional cavity (a rectangular or cylindrical cavity, for example) at frequencies ~ 1 GHz is that it is considerably less bulky (the dimensions of the conventional cavity are proportional to the wavelength — at 5 GHz, $\lambda = 6$ cm), and that the filling factor (magnetic energy stored in the sample/total stored magnetic energy) is typically much higher.

The sample is moved in towards the resonator from above as shown in figure 4.2. As it begins to interact with the B fields emerging from the central bore of the resonator (these are roughly perpendicular to the broad surface of the sample), screening currents are induced in the plane of the sample and dissipate energy thus reducing the Q. For a metallic sample, this will also have the effect of increasing the resonant frequency. In this geometry, this is due to the sample reducing the effective size of the cavity (a metallic sample acts so as to confine the B fields in the space below it) and thus increasing the resonant frequency. This increase in frequency effectively measures the position of the sample with respect to the resonator and can be used to set the position of the sample in a reproducible manner. A change in skin depth of the currents in the sample also has the effect of changing the resonant frequency; indeed, this is the principle by which we can make surface *reactance* or skin depth measurements using cavity perturbation. However, in this setup, the frequency shift due to a change in the skin depth is very small compared to the frequency shift due to a change in the overall position of the sample. Since this position is affected by thermal length contraction and expansion effects, it is clear that
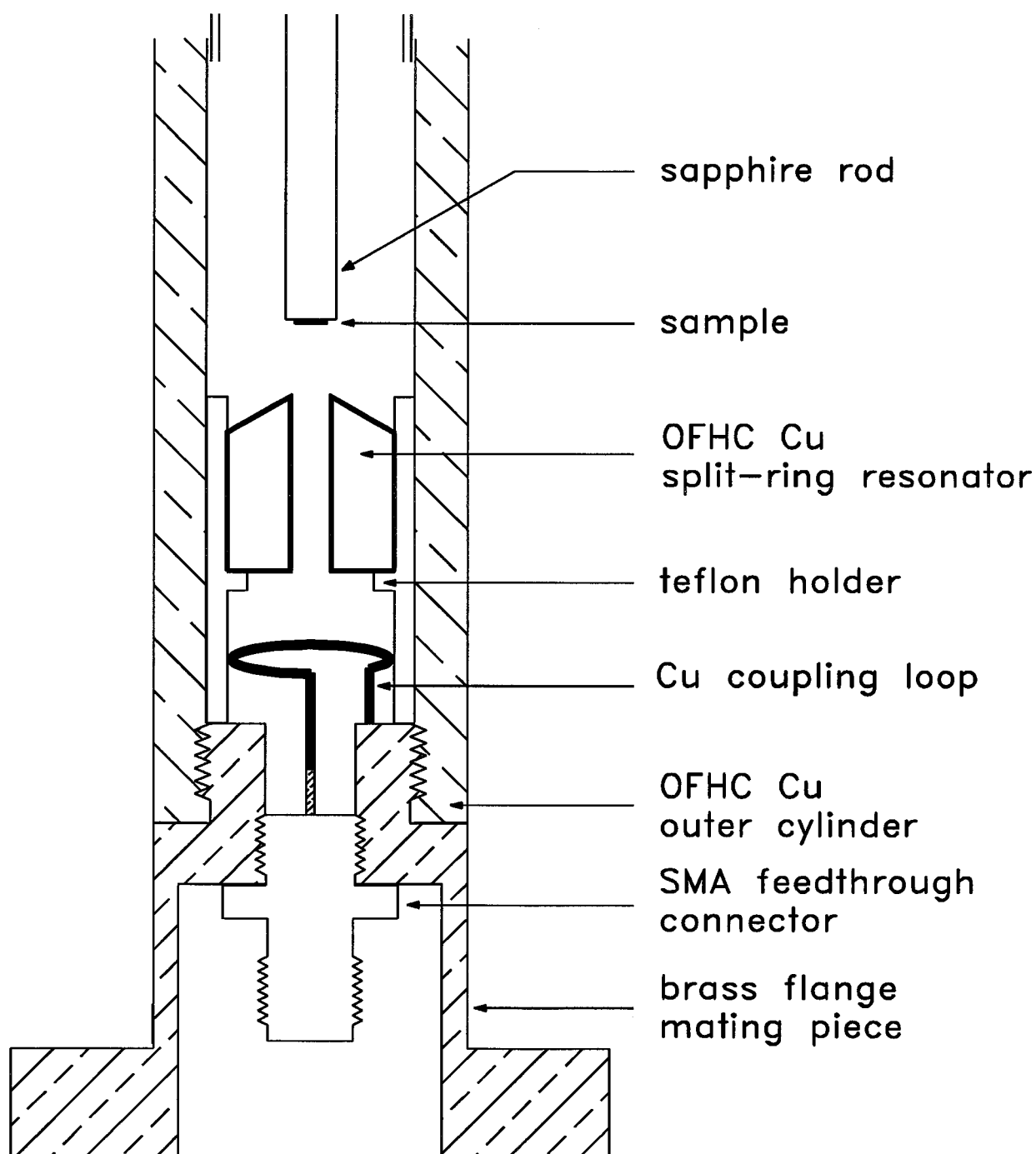
Figure 4.2: 5.4 GHz split-ring resonator and field geometry. During a measurement, the sample is positioned in the axial B fields that emerge from the central bore of the resonator.

this arrangement is not well suited to measuring surface reactance. By moving the sample closer to the top of the resonator, we increase the filling factor because we have moved the sample in to a region where the B fields are more concentrated (equivalently, a region where the energy density is higher). The fact that we can increase the sensitivity merely by moving the sample closer to the resonator is a considerable advantage of the split-ring resonator. As already mentioned, the currents are induced in the sample principally by screening the B fields from the metal or superconducting sample. The E fields are confined to the region of the gap and do not play a significant role in generating currents in the sample (the bevelling of the top of the resonator shown in figure 4.1 and 4.2 helps keep electric fields away from the sample — this is not so important for single crystals, but it can be for thin films having dielectric substrates).

Figure 4.3 shows a schematic diagram of the circuit used for reflectance measurements at 5.4 GHz. A Hewlett-Packard 83620A frequency synthesizer is the source and delivers power to the cavity through the main arm of a 20 dB directional coupler. The signal is then transmitted by semi-rigid co-axial cable to the cavity. The coupling to the cavity is made inductively with a loop of wire beneath the resonator and co-axial with its central bore (see figure 4.2). The coupling strength is set by adjusting the position of the coupling loop beneath the resonator. This must be done at room temperature during assembly and cannot be changed once the apparatus is cooled. Care must be taken in choosing the length of this wire to avoid $\lambda/4$ self resonances. One percent of the reflected signal is coupled to the crystal diode detector. Operation of the calibrated detector within its square-law region yields a dc output voltage proportional to the power in the reflected signal. The output from the detector is then amplified before being sent to an analog–to–digital converter for storage and subsequent analysis on the computer.

The resonant frequency, f_0, and the quality factor, Q, are determined by sweeping through the resonance with the synthesizer and recording the reflected power at each
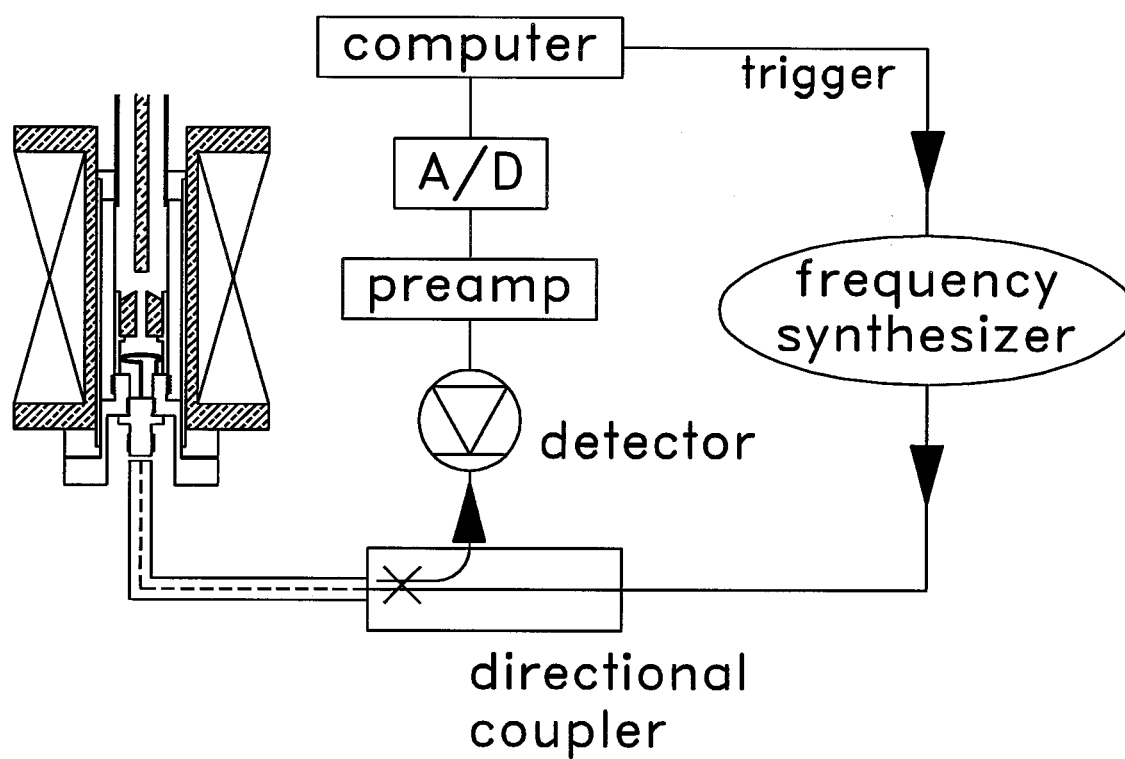
Figure 4.3: Schematic of circuit used for the 5.4 GHz reflectance measurements.

of a discrete number of frequency points (100, for example). The line shape of the reflected signal is fit to a Lorentzian plus a third order polynomial to allow for background variations. The latter is due to standing waves that are created in the circuit between the cavity and the directional coupler. These result from constructive and destructive interference between the incoming and outgoing signals. The power in any part of the circuit becomes position and frequency dependent. The problem tends to get worse as the overall frequency is increased, the net result sometimes being a background signal which can be a significant fraction of the power variation associated with the real signal of interest — the amount of power absorbed at the resonant frequency in the cavity and sample. This affects our ability to reliably extract the Lorentzian from the background in the fitting procedure and introduces an uncertainty in the fitted values of f_0 and Q.

4.3 The 27 and 35 GHz Cavities

The measurements at 27 and 35 GHz were obtained by moving the sample into the centre of right circular cylindrical cavities. In this frequency range, conventional cylindrical cavities work well because, since the cavities are smaller, the filling factor is much larger than at low-frequency (also, the losses in the sample have typically increased with the square root of the frequency or even faster). The TE_{011} mode was used, the field configuration of which is shown in figure 4.4. During the measurement, the sample is positioned at the centre of the cavity which corresponds to a node in the E field and a maximum in the B field. Just as for the split-ring resonator, the sample is placed in an rf B field that is perpendicular to the broad face of the sample, inducing screening currents in the plane of the sample. Thus for a $YBa_2Cu_3O_{6.95}$ single crystal, we induce only a-b plane screening currents. This field geometry is slightly different from that of the split-ring resonator in that there are strong B fields at both top and bottom surfaces of the crystal thus
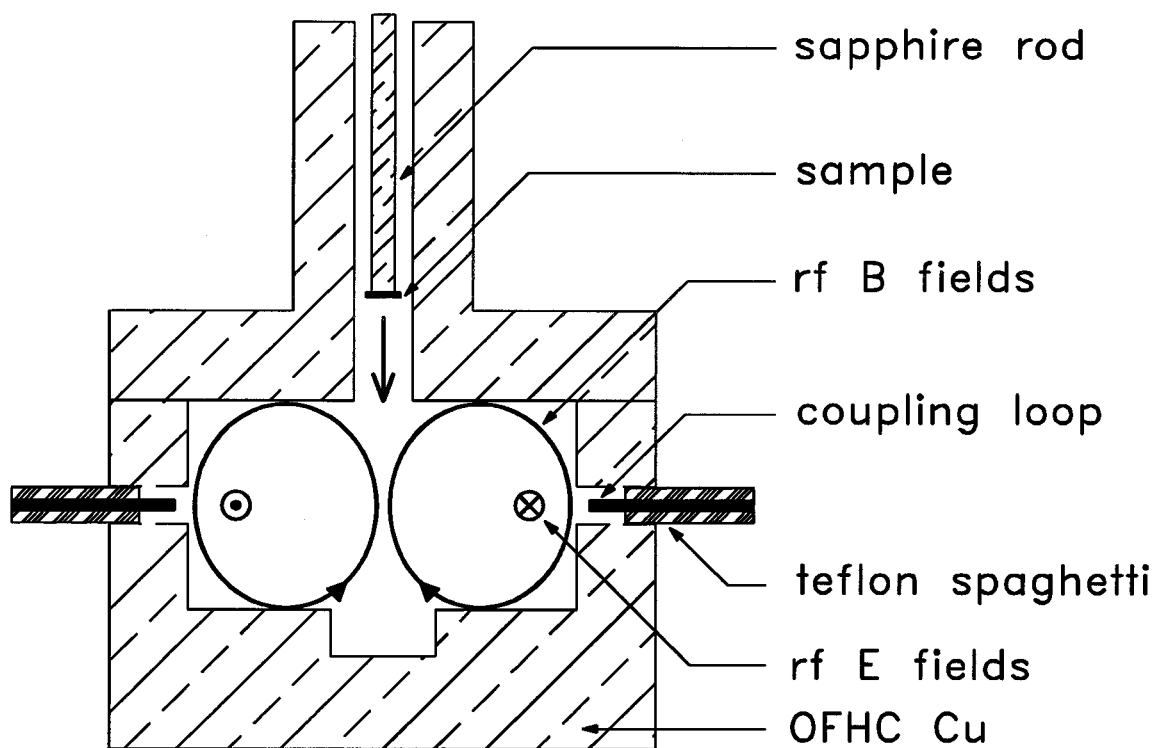
Figure 4.4: 27/35 GHz cylindrical cavity showing the geometry of the E and B fields. The well machined into the bottom surface of the cavity is to remove the degenerate TM_{111} modes.

sampling both sides equally; in the split-ring resonator experiment, more of the current runs on the bottom side of the sample (the side closest to the resonator). It turns out (see Appendix B) that most of the current runs near the edges of the sample, and so the difference in current distribution for the two geometries is not thought to be significant.

A separate cavity was built for each frequency in order to have good isolation between the mode of interest and all other modes. By fine-tuning the radius and height of the cavity, we can locate the TE_{011} mode at the desired frequency and place all other modes far enough away to avoid any mode-crossing when the sample is moved to the centre of the cavity. Special precaution must be taken to remove the two degenerate TM_{111} modes from the vicinity of the TE_{011} mode. This was achieved by machining out an on-axis well at the bottom surface of the cavity (see figure 4.4). The axial B fields of the TE_{011} mode have a node at the top and bottom surfaces of the cavity (while the E fields have a node along the central axis), and thus, it is not shifted much in frequency. The TM_{111} modes on the other hand have high field density on the bottom surface. The well is therefore very efficient in increasing the effective size of the cavity for these modes and shifting their resonant frequency down and out of the neighbourhood of the TE_{011} mode.

The electronic circuit for making measurements using either of the two cavities is shown in figure 4.5. In contrast to the 5.4 GHz measurements, these higher frequency measurements were made in transmission. The 83620A synthesizer was again used as the microwave source, but since the unit can generate frequencies no higher than 20 GHz, the output is amplified (HP 8349B) and doubled (HP 83554A) to give frequencies in the 26.5 GHz – 40 GHz range. The signal is again coupled into the cavity inductively using a loop of wire to link the H-fields from the TE_{011} mode. Another loop and coupling hole is used to couple the signal to a separate output waveguide. This waveguide takes the transmitted signal to a microwave detector. The voltage signal is then amplified and sent to an A/D converter and computer, as for the reflectance measurement.
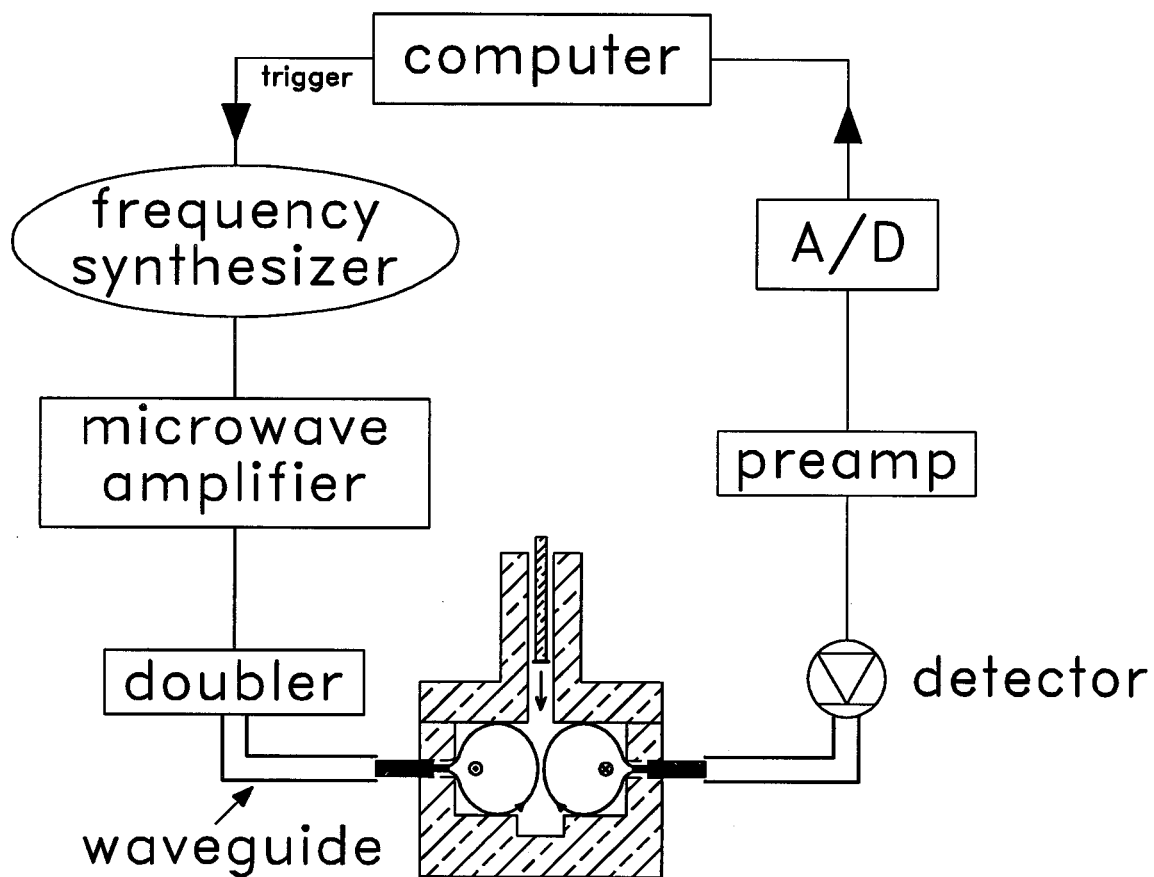
Figure 4.5: Schematic of circuit used for the 27 and 35 GHz transmission measurements.

In transmission, the non-trivial problem of the standing waves manifests itself differently from the sloping background signal observed in reflectance. Away from resonance, no signal is transmitted through the cavity and so there is not a sloping background. Instead, the standing waves present in the input and output waveguide circuits will tend to distort the line shape, and this again introduces uncertainty into the fitted values of f_0 and Q.

4.4 Probe Design

Figure 4.6 shows the design of the lower end of the probe. Both the low (100 MHz – 6 GHz) and high (26.5 - 40 GHz) frequency inserts use this design. The sample is mounted on the end of a rod made from sapphire, which has two important properties in the the temperature range of interest: it has a very high thermal conductivity and extremely low loss at microwave frequencies. When the cavity is loaded with the sample, only the sample itself and the sapphire rod are exposed to the high frequency E and B fields. This is ensured by having a sapphire rod long enough to keep the copper housing assembly for the thermometer and heater away from the fields. Since the sapphire has negligible loss, it is thus only the losses in the sample itself that are measured. In good thermal contact with the sapphire rod is a Lakeshore Cryogenics carbon-glass thermometer (a tiny amount of silicone grease is used to ensure good thermal contact between the thermometer and the copper housing). Thus, because the thermal conductivity of the sapphire is so high, this thermometer accurately measures the temperature of the sample. At typical operating temperatures, a gradient of no more than a few tenths of a kelvin was observed between the two ends of the rod.

Evanohm heater wire of total resistance approximately 200 Ω is wrapped around the top part of the copper heater/thermometer assembly. It is this heater that is used to

thin—wall
stainless steel tube

outer view
of brass
spring

brass spring

sample heater

Cu thermom./heater
housing assembly

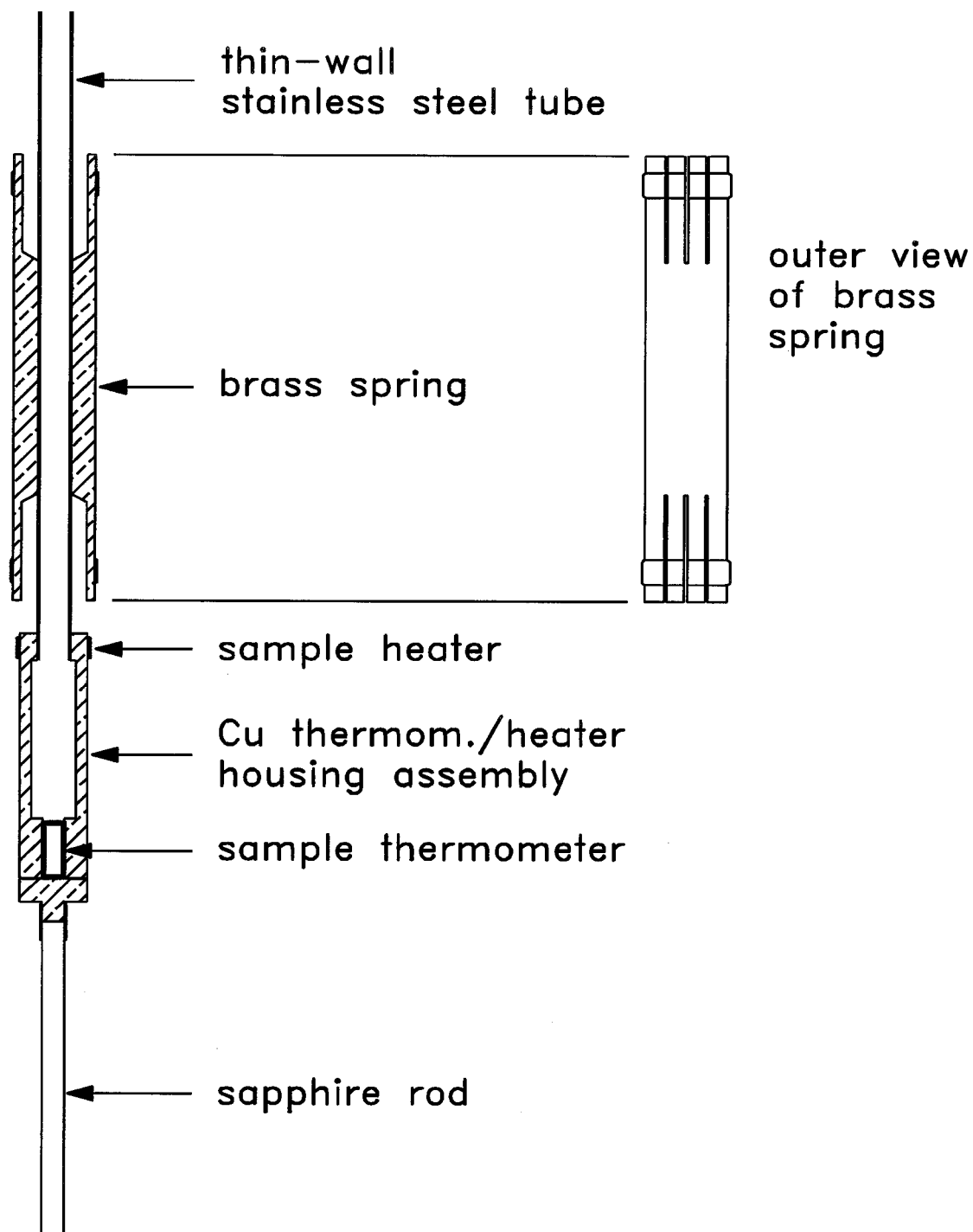sample thermometer

sapphire rod

Figure 4.6: Detail of the lower end of the probe. There is another brass spring positioned approximately halfway between this end of the probe and the room-temperature end. There are two brass radiation baffles placed along this length as well.

adjust the temperature of the sample from its low temperature value of approximately 20K up to temperatures of the order of 100K. This copper assembly is connected via a thin wall stainless steel tube to a brass "spring" (see figure 4.6) through which a central hole has been drilled. The stainless steel tube is soldered to this brass spring and also to another identical brass spring farther up the probe. Both outer and cross-sectional views of the brass spring are given in figure 4.6. There are eight spring-like fingers on each end of the piece. The probe is designed to slide inside a 0.5" O.D. stainless steel tube which connects the microwave cavity assembly to the top of the cryostat and forms the vacuum chamber. Figure 4.7, for example, shows the probe inserted into the apparatus used for the 5.4 GHz experiments. The brass springs have two important functions: they hold the probe in alignment with the vertical axis of the experiment; and, since the outer 0.5" tube is in good thermal contact with the helium bath, they provide the main thermal connection between the sample and 4.2K. The length of the stainless steel tube between the copper housing assembly and the solder joint at the lower brass spring sets the time constant for cooling of the sample. In choosing the length of this piece, a compromise has to be reached between the power needed to raise the temperature of the sample to its upper limit and the thermal time constant. In the present apparatus, approximately 100 mW is required to heat the sample above 100K and the cooling time is about two hours.

The two wires from the heater and the four wires from the thermometer are enclosed within teflon spaghetti which is threaded through the stainless steel tubing on its way to the top of the probe. Connection to a four-lead resistance bridge and a temperature controller is made via the electrical feedthrough. The six brass wires are heat sunk at each of the brass springs to reduce the heat leak down the wires. Small baffles are also used on the outside of the stainless steel tubing to reduce thermal radiation down the 0.5" stainless steel tube.
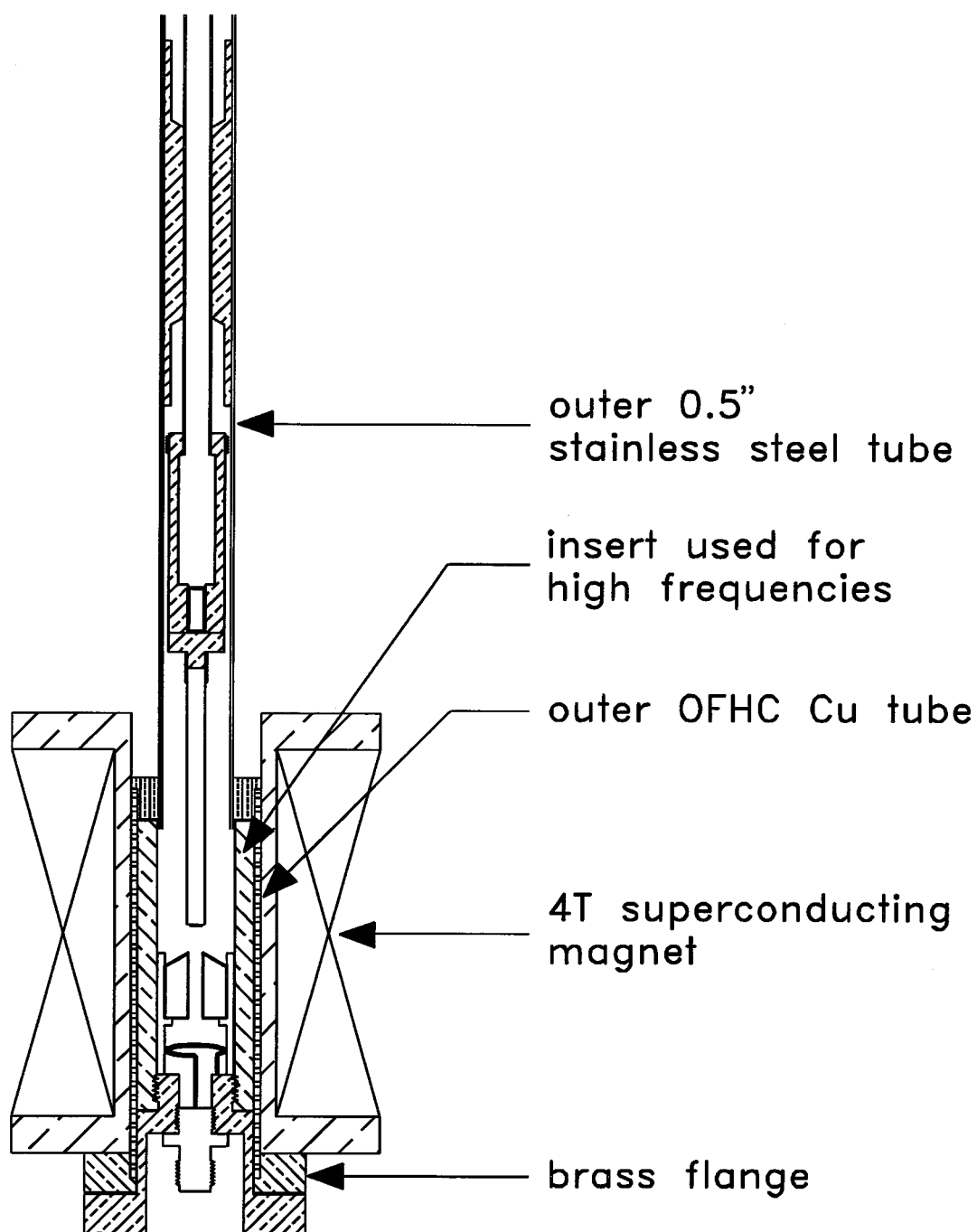
outer 0.5"
stainless steel tube

insert used for
high frequencies

outer OFHC Cu tube

4T superconducting
magnet

brass flange

Figure 4.7: Overview of the apparatus used in the 5.4 GHz experiments.

4.5 The Low Frequency Cryostat

Because of the modular design, the cryostat used for the 5.4 GHz measurements could be used (with the appropriate insertion of a particular resonator) anywhere in the range from a few hundred MHz up to about 6 GHz. In fact, over most of this frequency range, all that is required is the fabrication of a split-ring resonator with appropriate inner bore and gap to obtain the desired resonant frequency. At the higher frequencies (e.g. 5.4 GHz) a special insert was used (see figure 4.2) to reduce the diameter of the outer shield and so keep it well beyond cut-off. Otherwise, there was the possibility of the microwave fields reaching the copper thermometer/heater housing assembly. Figure 4.7 gives an overall picture of the 5.4 GHz experiment. The resonator sits in a teflon holder which must be screwed down on to the flange piece. An indium O-ring is used to make a vacuum seal at the lower flange. An hermetically sealed SMA feedthrough connector is used on the insert piece to allow the microwave signal in to the cavity. The feedthrough connector is screwed into the insert piece during construction and then sealed around the threads with black 2850 FT epoxy. One end of the coupling loop wire is soldered to the inner conductor on the feedthrough while the other end is screwed down onto the insert piece itself to provide a path to ground.

The outer copper cylinder that houses the resonator assembly sits within the bore of a superconducting magnet that is able to generate a field of up to 4T (corresponding to a current of 40A). The magnet was home-made using NbTi wire with provision for persistent mode operation. The two ends of the NbTi wire that emerge from the magnet are joined together using a technique[71] to give a high critical current. Evanohm heater wire is wound around a 6cm stretch of the NbTi wire. This section of wire is then potted in Emerson and Cummings Stycast 1266 epoxy to form the persistent switch. Connection to two tinned brass shimstock magnet leads are made via short stretches of tinned copper

wire. These are joined to the superconducting magnet wire via simple soft solder joints. These joints are not critical as they are only important during charging and discharging of the magnet. In persistent mode (after the external power supply is switched off) the current only runs through the loop of superconducting wire and the high critical current joint. When a current is applied to the heater wire in the persistent switch, the stretch of NbTi wire potted in epoxy is driven normal, thus allowing the magnet to be charged or discharged. Two protection diodes on the top of the cryostat at room temperature provide a safe, dissipative current path in case of a quench of the magnet during charging or while in persistent mode.

4.6   The 27 and 35 GHz Cryostat

A detailed discussion of the cryostat used for the 27 and 35 GHz measurements will be given in the Ph.D. thesis of Kuan Zhang. Here, we shall discuss only its most important features and any conceptual differences from the low-frequency cryostat. Modularity of design is a convenient feature of this high frequency cryostat as is evidenced by the ease with which we can switch between the 27 and 35 GHz measurement. All that is required is to replace the 35 GHz cavity block (made from OFHC copper) with the 27 GHz cavity block. The frequency limits are set by the $26.5 - 40$ GHz waveguide, two sections of which run from each side of the cavity up to the top plate of the cryostat. Unlike the split-ring resonator set-up, there is variable coupling (on both input and output) and this allows coupling adjustment at low temperature. This is an absolute necessity if the OFHC cavity is plated with a superconducting PbSn alloy for high-Q ($> 10^6$) usage at low temperature. The Q of the cavity increases so dramatically, once its temperature drops below the T_c of the PbSn, that it is very difficult to set a coupling at room temperature that is suitable for the high Q at low temperature. The high field measurements of the present study

preclude the use of PbSn plating (since the field would destroy the superconductivity in the PbSn); however, variable coupling is still of considerable practical convenience.

A high homogeneity, 8T superconducting magnet is used to generate the static magnetic fields for the 27 and 35 GHz measurements. It is mounted on a separate support in which the entire high frequency cryostat can be inserted.

The other important difference in this cryostat is that the main stainless steel tube in which the probe is situated is not in direct contact with the helium bath. The coupling holes through which the coupling wires must be free to move while adjusting the coupling are not leak-tight. Therefore, everything is enclosed within a large stainless steel tube closed at the low temperature end and sealed to the top-plate of the cryostat with a rubber O-ring seal at the room temperature end. It is this tube that is immersed directly in the helium bath, the main apparatus itself is in vacuum. In order to provide increased thermal contact between the cavity and the bath, two large copper braids join the cavity to the bottom of the outer tube. To use the PbSn superconducting cavity, it is important to lower the temperature of the cavity to well below the $\sim$ 7K transition temperature. For this purpose, an open stainless steel tube, the lower end of which sits directly in the liquid helium, is placed in good thermal contact with the cavity. By pumping on the top end of this tube, cold helium can be drawn up into the tube and used to cool the cavity to the temperature of the helium bath.

Chapter 5

The Experimental Procedure

In this chapter we first present some of the general characteristics of the $YBa_2Cu_3O_{6.95}$ single crystal sample used in the experiments and then describe the experimental procedure used for collecting the data. Since the low-frequency 5.4 GHz measurements and the high frequency 27 and 35 GHz measurements were made in two totally different cryostats, they each had their own specific set of problems and are described separately.

5.1 The $YBa_2Cu_3O_{6.95}$ single crystal sample

The $YBa_2Cu_3O_{6.95}$ sample used in the measurements at all frequencies was a very high quality single crystal grown at U.B.C.[30]. Crystals from all batches have T_c's greater than 93K. The transitions can be characterized by techniques such as dc resistivity, magnetization, specific heat and microwave surface resistance. All show extremely sharp transitions; in particular, the specific heat jump at T_c has a width of less than 0.25K - the narrowest yet reported. The crystals are typically of uniform thickness and the best ones have optically smooth surfaces and clean, unfractured edges. The crystals can be cleaved in the a–b plane quite easily and so often it is possible to cleave away parts of a crystal that are contaminated by flux or that include a damaged edge. The latter is important for the microwave technique described in this thesis since the highest current density exists near the edges of the sample and a crack can cause anomalously high losses. Microwave surface resistance in zero field indeed provides a stringest test of sample quality. R_s data measured at 3.8 GHz on one of the single crystals is shown

in figure 2.2. The sharpness of the transition and the low residual loss are indicative of very high sample quality. Although the occasional crystal can be found with no twin boundaries, the majority of the crystals are not twin-free. The single crystal used in the experiments described in this thesis was of dimensions $1.5\text{mm} \times 1.5\text{mm} \times 10\mu\text{m}$ and was typical of the best crystals; however, twin boundaries were observed to be present.

5.2   5.4 GHz Measurements

An important characteristic of the split-ring resonator is how $\Delta(1/Q)$ depends on $\Delta(f)$ as the sample is moved towards the top of the resonator. Such a curve for the $\text{YBa}_2\text{Cu}_3\text{O}_{6.95}$ single crystal at a temperature of 100K (this is in the normal state where the losses are high) is shown in figure 5.1. It is basically linear through the origin with a small vertical offset. The linear behaviour is to be expected since both the loss in the sample and the frequency shift measure the overall perturbation to the cavity. The slight offset is due to a small negative dielectric shift from the sapphire rod which quickly becomes overwhelmed by the positive shift due to the sample. This is only observed for small samples; larger samples not only screen the sapphire more effectively but also give rise to larger positive frequency shifts (for such samples, the $\Delta(1/Q)$ versus $\Delta(f)$ curve extrapolates through the origin). The $\Delta(1/Q)$ versus $\Delta(f)$ curve is universal for a given sample in the sense that no matter what the loss, the negative offset is always the same and the behaviour is linear. It is the *slope* that changes, the line having a steeper slope when there is more loss. Clearly, the slope of this line is proportional to the loss in the sample. However, since the curve is always linear with the same negative frequency shift offset, we don't need to measure the whole curve but only one point. This is in fact how the measurements were made: an operating $\Delta(f)$ was chosen, 7 MHz for example, the sample was moved in towards the resonator until a frequency shift of 7 MHz was achieved, and then measurements
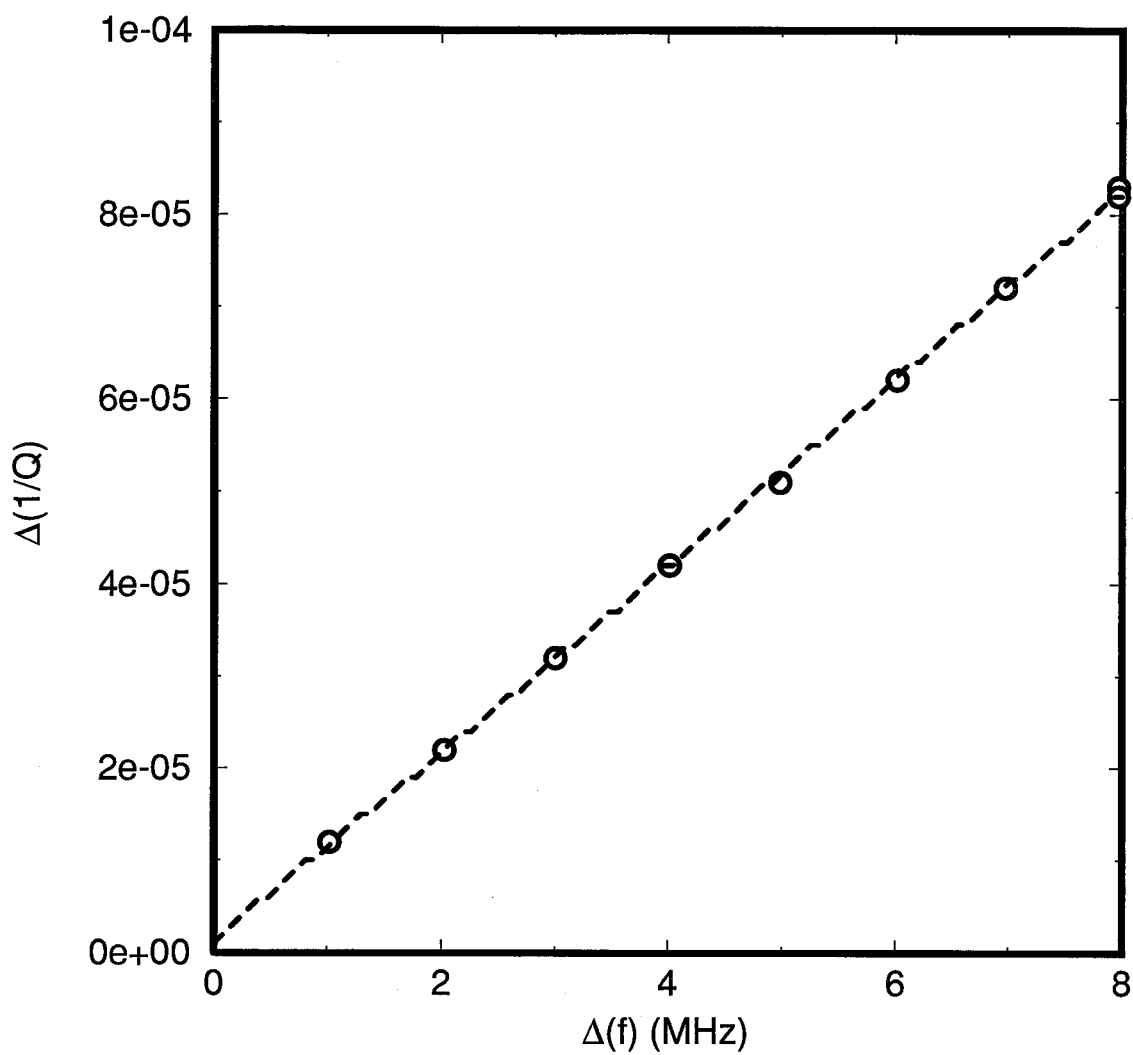
Figure 5.1: Dependence of $\Delta(1/Q)$ on $\Delta(f)$ at 100 K for the 5.4 GHz copper split-ring resonator. The dashed line is a linear fit. The data is fit well by a line with a small vertical offset.

were made by varying the temperature while leaving the sample in this position. Due to thermal expansion and contraction of the sapphire rod (and to a lesser extent, the entire probe), the position of the sample with respect to the resonator can change slightly and the resonant frequency wanders away from the nominal value. However, this is simply corrected for by moving along the universal curve. For example, if the nominal frequency shift is given by $\Delta(f)^{\mathrm{nom}}$ and the measurement gives the pair of values $(\Delta(f), \Delta(1/Q))$, then we can calculate $\Delta(1/Q)^{\mathrm{nom}}$ as follows: the universal curve is

$$\Delta(1/Q) = a\,\Delta(f) + b \tag{5.1}$$

and so we get

$$\Delta(1/Q)^{\mathrm{nom}} = \left(\frac{\Delta(1/Q) - b}{\Delta(f)}\right)\,\Delta(f)^{\mathrm{nom}} + b. \tag{5.2}$$

It is clearly important for the the operating point for the measurements to be on a linear portion of this curve. If the operating point corresponds to a physical position too close to the top of the resonator, it is possible to introduce non-linearity due to the fringing electric fields from the gap interacting with the sapphire and causing anomalous negative frequency shifts. This may be accentuated if the sapphire rod is not perfectly centrally aligned and descends towards the resonator on the side where the gap is. Care must be taken before a series of measurements is started to ensure that the $\Delta(1/Q)$ versus $\Delta(f)$ curve is linear over the frequency range of interest.

Another important check to be made is the $\Delta(1/Q)$ versus $\Delta(f)$ curve for the sample in the superconducting state in zero field. At 5.4 GHz, the loss in zero field of $YBa_2Cu_3O_{6.95}$ is orders of magnitude below the sensitivity of the OFHC copper resonator. The $\Delta(1/Q)$ versus $\Delta(f)$ curve should therefore be a line of zero slope along the $\Delta(f)$ axis (within the noise). Figure 5.2 shows what was actually measured for the $YBa_2Cu_3O_{6.95}$ single crystal. It is a line with negative slope meaning that the Q increases as we move the sample in towards the resonator! This type of non-perturbative effect was discussed in section 4.1.
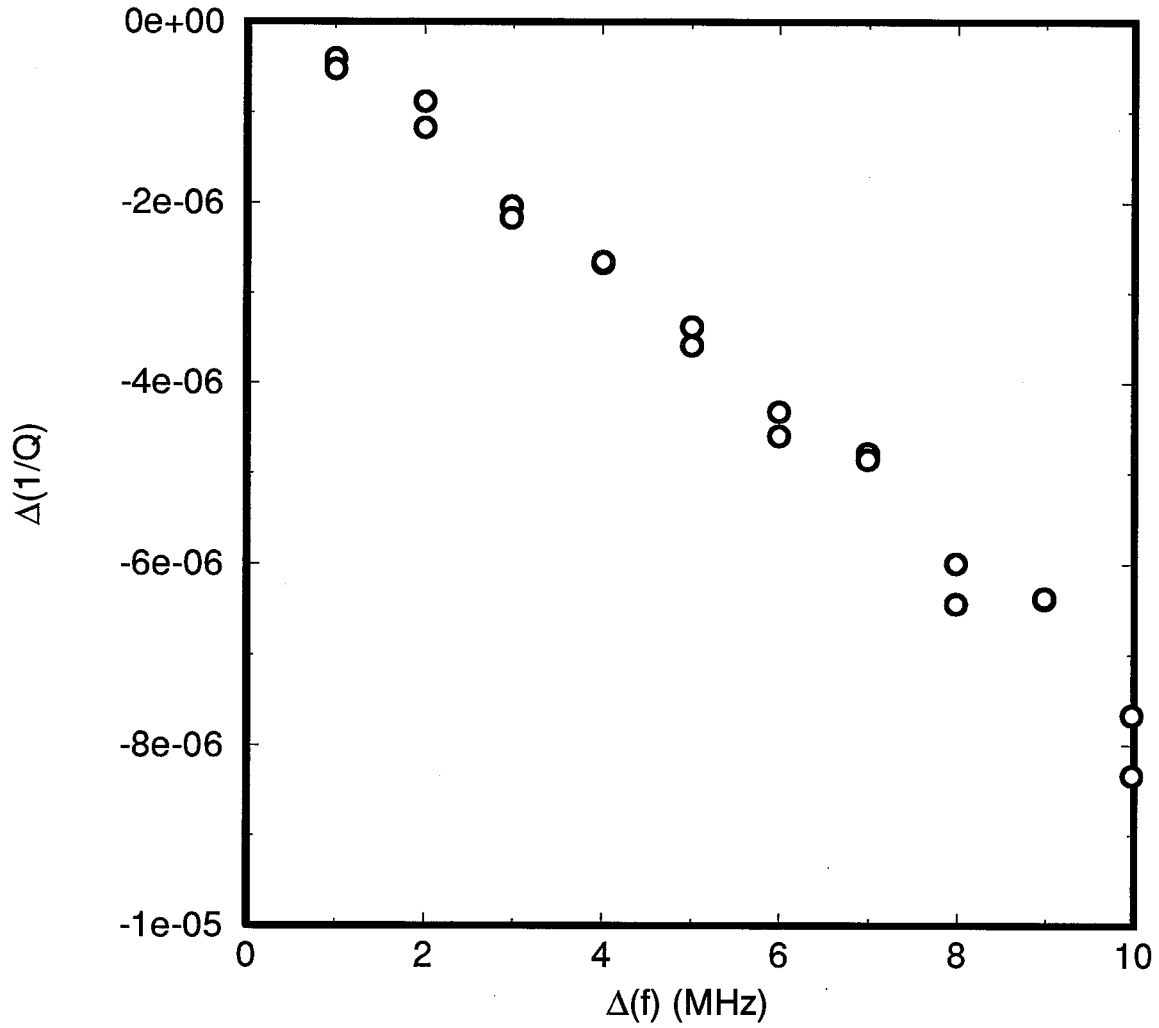
Figure 5.2: Dependence of $\Delta(1/Q)$ on $\Delta(f)$ for zero-loss sample in the 5.4 GHz copper split-ring resonator. The Q of the cavity *increases* when we insert a sample with effectively no loss. This is due to the rearrangement of the fields as the sample is moved towards the resonator. The two points at each value of $\Delta(f)$ reflects the fact that two measurements were made at each nominal frequency shift.

It is due to a rearrangement of the rf fields when the sample and sapphire rod are moved close to the resonator (the rearrangement of the fields is insensitive to any temperature dependent changes in the sample since these are dwarfed by the effect caused by just its physical position). This background systematic effect will be independent of temperature and present in all of the data tending to give an apparent loss less than the actual loss. Therefore, we must be careful to correct for this in the raw $\Delta(1/Q)$ data. This is done as follows: if the systematic effect is described by

$$\Delta(1/Q)^{\text{sys}} = -a'\,\Delta(f) - c'$$ (5.3)

then the $\Delta(1/Q)$ corrected for the systematic effect will be

$$\Delta(1/Q)^{\text{C}} = (a + a')\,\Delta(f) + (c + c'),$$ (5.4)

and we then get the $\Delta(1/Q)^{\text{C,nom}}$ corresponding to the nominal frequency shift as in equation 5.2

$$\Delta(1/Q)^{\text{C,nom}} = \left(\frac{(a + a')\,\Delta(f) + c'}{\Delta(f)}\right)\Delta(f)^{\text{nom}} + (c + c').$$ (5.5)

We thus have all the ingredients to convert the raw data into a set of $\Delta(1/Q)$ values corrected for the negative background loss and any small changes in the position of the sample during the course of the temperature sweep. The following was the step by step procedure used to measure the $\Delta(1/Q)$ as a function of temperature for a given field:

- the $\Delta(1/Q)$ versus $\Delta(f)$ curves for the sample in the normal and superconducting state in zero field were measured to ensure a linear dependence of $\Delta(1/Q)$ on $\Delta(f)$ and to measure the background systematic effect.

- an operating point (or nominal frequency shift) was chosen. A $\Delta(f)^{\text{nom}}$ was chosen large enough to produce easily measurable $\Delta(1/Q)$ values but not so large so as to be out of the linear portion of the $\Delta(1/Q)$ versus $\Delta(f)$ curve.

- the sample was heated above T_c .

- the static magnetic field was applied.

- with the sample pulled completely away from the resonator, the unloaded f_0 and Q_0 were measured.

- the sample was moved in to the nominal frequency shift position chosen.

- the heater was turned off and the sample cooled to low temperature.

- the resonant frequency and Q of the cavity were measured as a function of temperature right up through T_c . The highest temperature measured was typically 100K.

- at the highest temperature, the sample was again pulled back from the cavity, and the unloaded f_0 and Q_0 were measured again.

- the $\Delta(1/Q)$ (T) and Δ(f) (T) data were corrected for the negative background loss and any change in position of the sample using equation 5.5.

In the above procedure, great care was taken not to change the field or move the sample unless $T > T_c$. The point is that very strong pinning forces can result when the flux density in the sample is changed. In an earlier experiment, a large $YBa_2Cu_3O_{6.95}$ crystal was totally shattered by moving it in the inhomogeneous part of the magnetic field when T was below T_c.

Once the corrected $\Delta(1/Q)$ values have been obtained, the data was calibrated by using the $\Delta(1/Q)(100K)$, taking ρ_{dc} =77.8 $\mu\Omega$–cm, and using the classical skin effect formula for the surface resistance of a metal. Although the dc resistivity on this particular crystal was not measured, this value for $\rho_{dc}(100K)$ was typical of other crystals made

with the same technique. It is probably good to $\pm 10\%$. This gives a calibration factor

$$C = \frac{\sqrt{\rho_{\mathrm{dc}}(100K)\,\mu_0\,\omega/2}}{\Delta(1/Q)(100K)} = 1686. \tag{5.6}$$

However, because the crystal had a thickness of only 10–12 μm and the microwave skin depth at 5.4 GHz with a dc resistivity of 77.8 $\mu\Omega$–cm is $\sim 6\mu$m, it was not clear whether or not the sample was accurately in the classical skin depth limit. For this reason, a PbSn calibration sample was cut[1] to close to the same dimensions as the single crystal sample. The resistivity of the PbSn was taken from the literature for Pb and has been found (by Bonn, in independent measurements with a superconducting split-ring resonator at 3 GHz) to reproduce the temperature dependence of the PbSn to $\pm 1\%$. Using the copper split-ring at 5.4 GHz the temperature dependences were found to agree to $\pm 5\%$. The calibration constant determined using the reference sample was found to be 1898. As expected, this number was greater than that obtained using the classical skin effect formula (a sample comparable in thickness to the skin depth, gives enhanced losses), but considering the uncertainty in the PbSn calibration procedure, the difference is not large. It was the latter number that was used to convert the $\Delta(1/Q)$ values to surface resistance, R_s. The temperature dependence of R_s for applied static magnetic fields ranging between 0.5T and 4T is shown in figure 5.3.

5.3 The 27 and 35 GHz measurements

The high frequency measurements made in the circular cylindrical cavities are slightly less complicated in practice because the sample is located at a maximum in the microwave field strength (see Chapter 4) rather than at a steep gradient as is the case with the split-ring resonator. Thus, if we introduce a lossy sample into the cavity and measure the Q as a function of position, it exhibits a broad maximum at the centre of the cavity where we
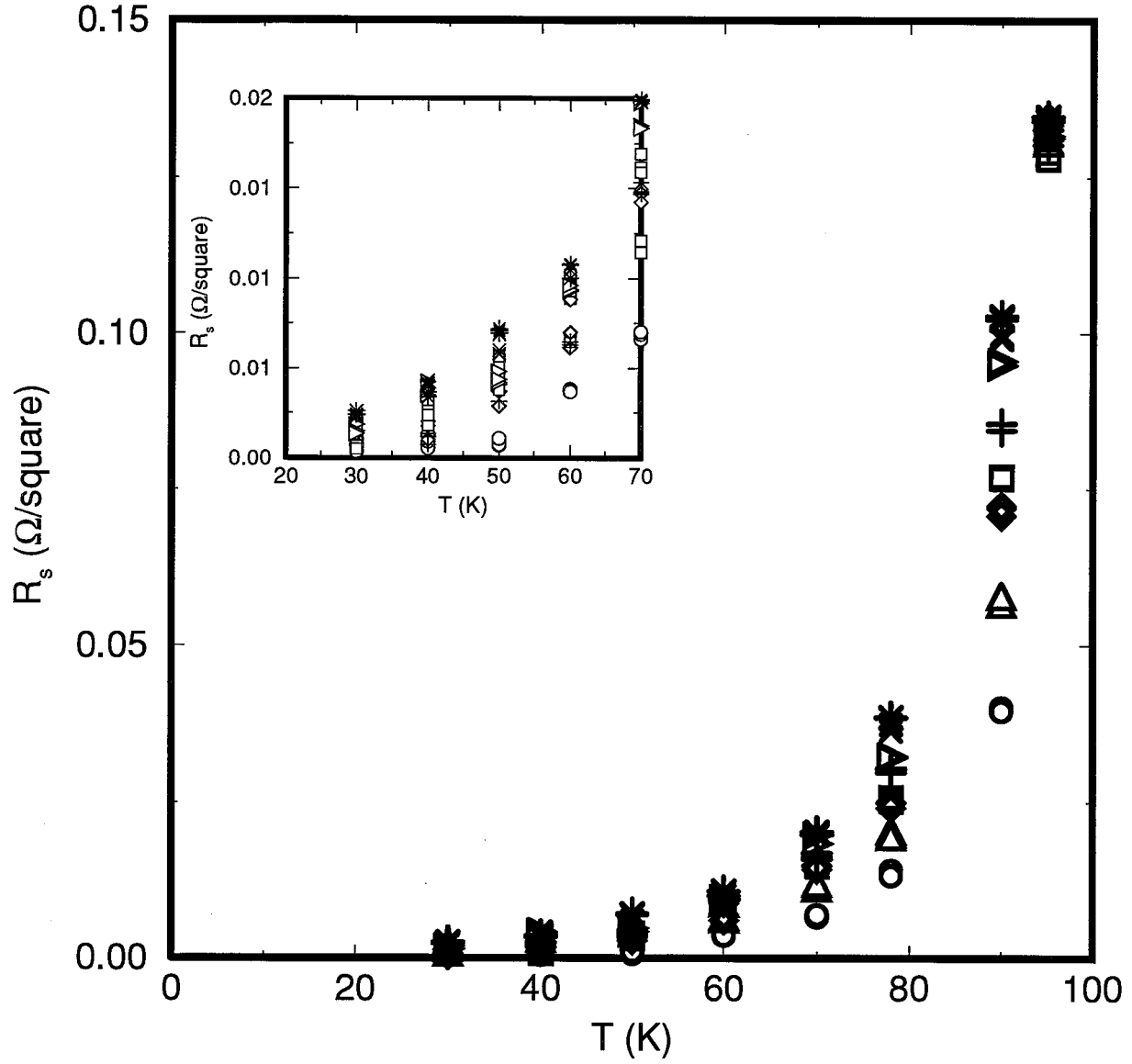
---

[1] This was done by D.A. Bonn

Figure 5.3: R_s in fields up to 4T at 5.4 GHz. ◯ 0.5T; △ 1.0T; ◇ 1.5T; □ 2.0T; + 2.5T; ▷ 3.0T; × 3.5T; ∗ 4.0T. Inset: close-up of the lower temperatures. R_s begins to become difficult to measure below about 60K.

locate the sample for measurements. This means that the sample is insensitive to small changes in its position during the course of a temperature sweep. However, systematic, non-perturbative effects on the Q are more difficult to correct for because the zero-field loss in the sample is not negligible as it was at 5.4 GHz. The reason is that the zero-field losses in the sample have increased by a factor close to ω^2 and are therefore measurable at 35 and 27 GHz even with copper cavities. We thus have no 'zero-loss' sample to easily identify the changes in Q that result from rearrangement of the field pattern.

This problem was solved in the 35 GHz measurements by making an identical measurement of the zero-field $\Delta(1/Q)$ as a function of temperature in the copper cavity and also in an identical but PbSn plated, superconducting, high-Q, cavity. The two $\Delta(1/Q)$ curves are shown in figure 5.4. Subtracting off a temperature independent constant from the curve obtained using the copper cavity, causes the two curves to be essentially identical. This constant was then subtracted off all the data taken with the copper 35 GHz cavity to correct for this systematic effect. The reasoning here is that when the sample is inserted into the centre of the cavity, it perturbs the ac fields enough so that extra loss is generated either in the walls of the cavity or most likely in the coupling loops and holes. The effect of this will be much less in the superconducting cavity because of the greatly reduced loss in all current-carrying surfaces. Thus, we take the superconducting cavity as the zero-loss reference; certainly, on the scale of the losses measured in a finite magnetic field, any further corrections are negligible. Once we have determined this constant for measurements in the copper cavity for a certain coupling strength on the input and output, we must not adjust the coupling throughout the rest of the experiment.

As far as acquiring all of the magnetic field data was concerned, the same basic steps were used as for the split-ring measurements. Only the subsequent corrections for systematic effects and changes in sample position were different.

Calibration of the 35 GHz data was done using the classical skin effect formula and
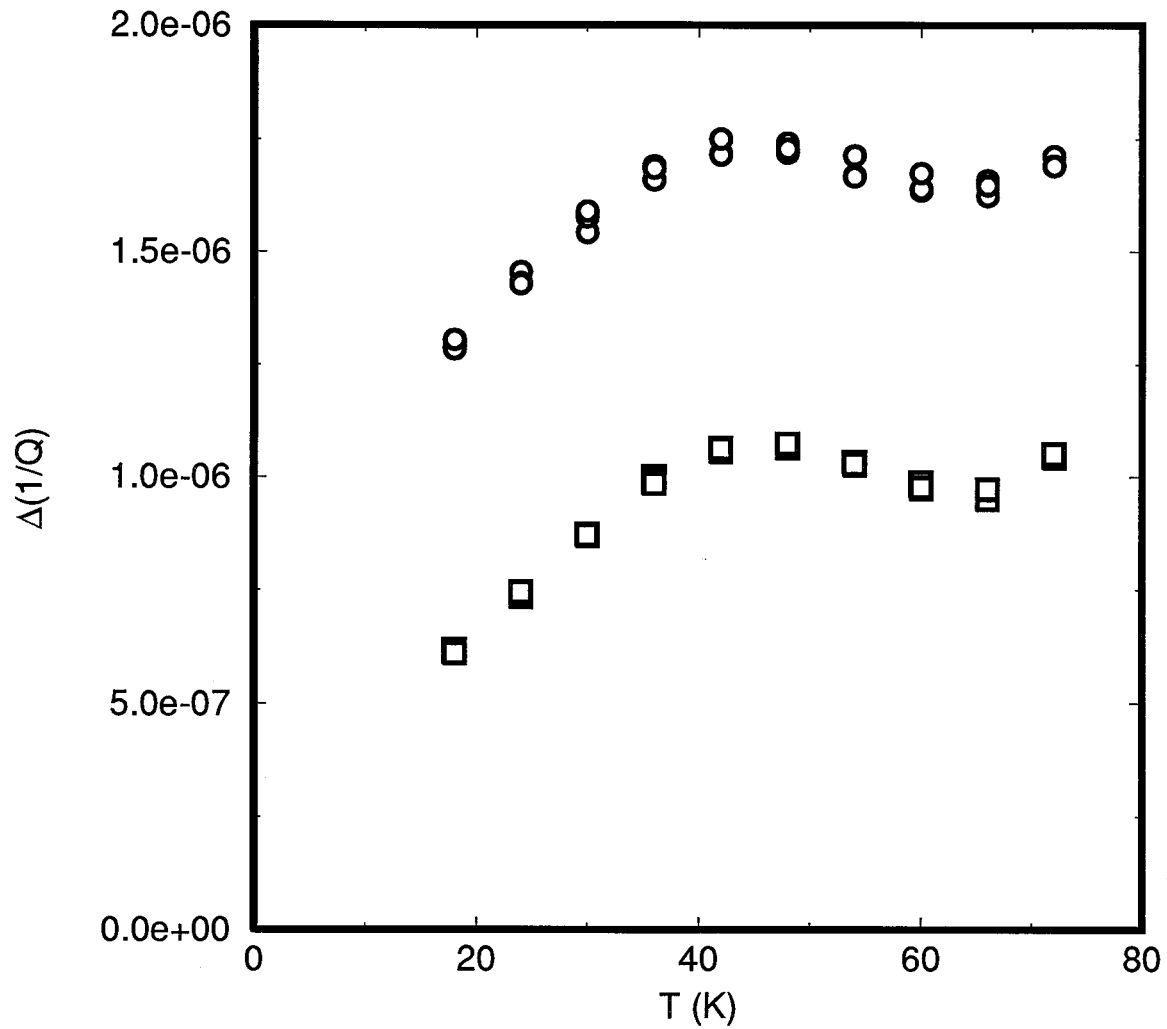
Figure 5.4: Systematic error in 35 GHz copper cylindrical cavity. The circles are the data obtained with the Cu cavity and the squares are the same sample measured in an identical cavity plated with PbSn.

$\rho_{\rm dc} = 77.8\mu\Omega$–cm. The skin depth at 100 K is approximately 2 μm at 35 GHz — well into the bulk limit. R_s versus T for fields ranging from 0 to 6T is shown in figure 5.5.

The 27 GHz R_s data was obtained in the same manner as the 35 GHz measurements apart from the correction for the non-perturbative change in the Q upon insertion of the sample. Since a PbSn plated version of the 27 GHz cavity was not available, the following procedure was adopted as the next best alternative: the 27 GHz data was first calibrated ignoring the possibility of a systematic error; zero-field measurements by Doug Bonn and Kuan Zhang on $YBa_2Cu_3O_{6.95}$ single crystals suggest a $\omega^{1.9}$ scaling of the surface resistance at 70K, and so a constant was subtracted from the 70K, 0-field point at 27 GHz to make it consistent with the 35 GHz zero-field data and the above scaling relation; this constant was then used to subtract from all the R_s data measured at 27 GHz.

The resulting R_s data plotted versus temperature for fields ranging from 0 to 8T are shown in figure 5.6.
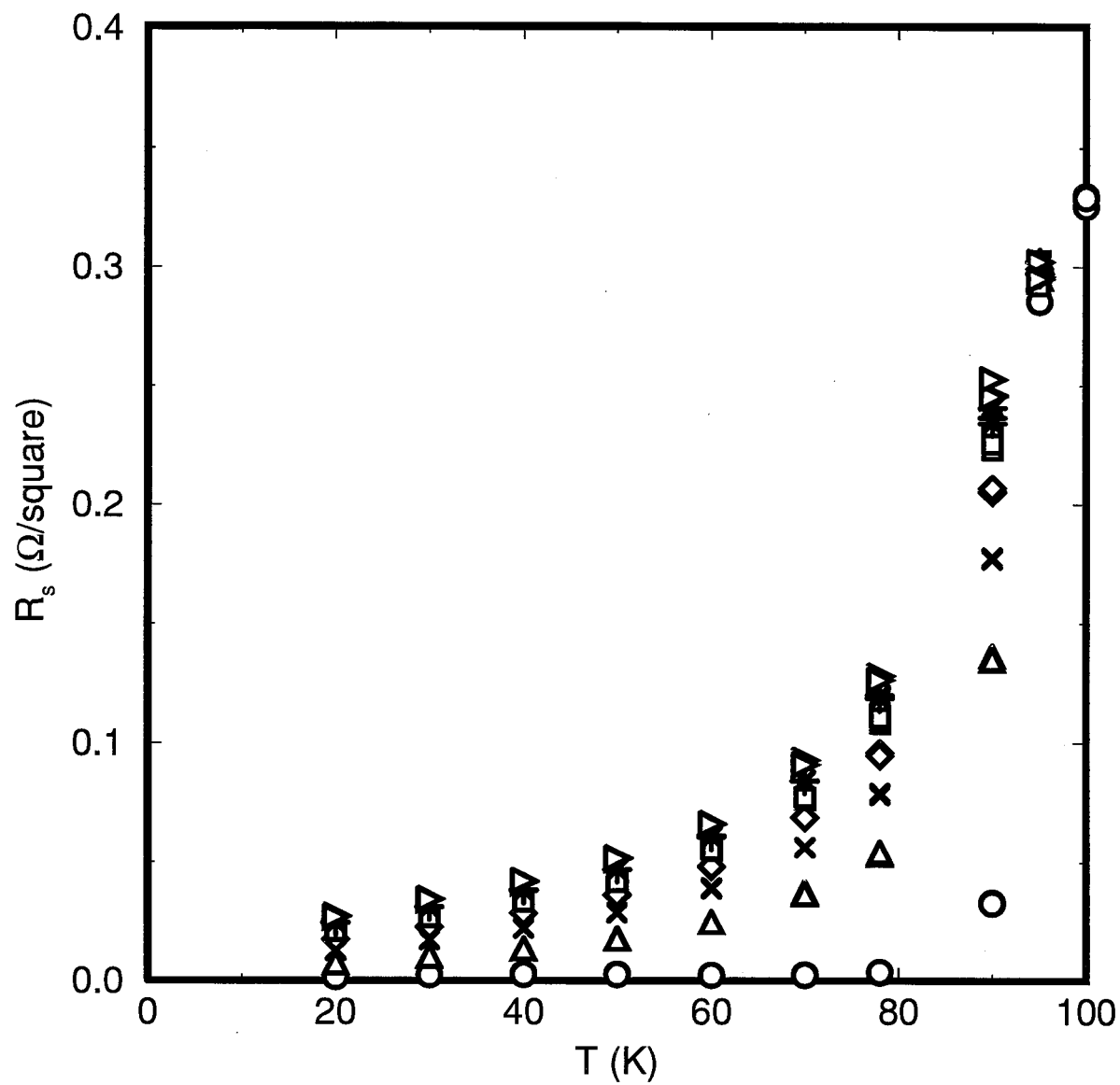
Figure 5.5: Temperature dependence of R_s in a magnetic field at 35 GHz. ○ 0T; △ 1T; × 2T; ◇ 3T; □ 4T; * 5T; ▷ 6T.
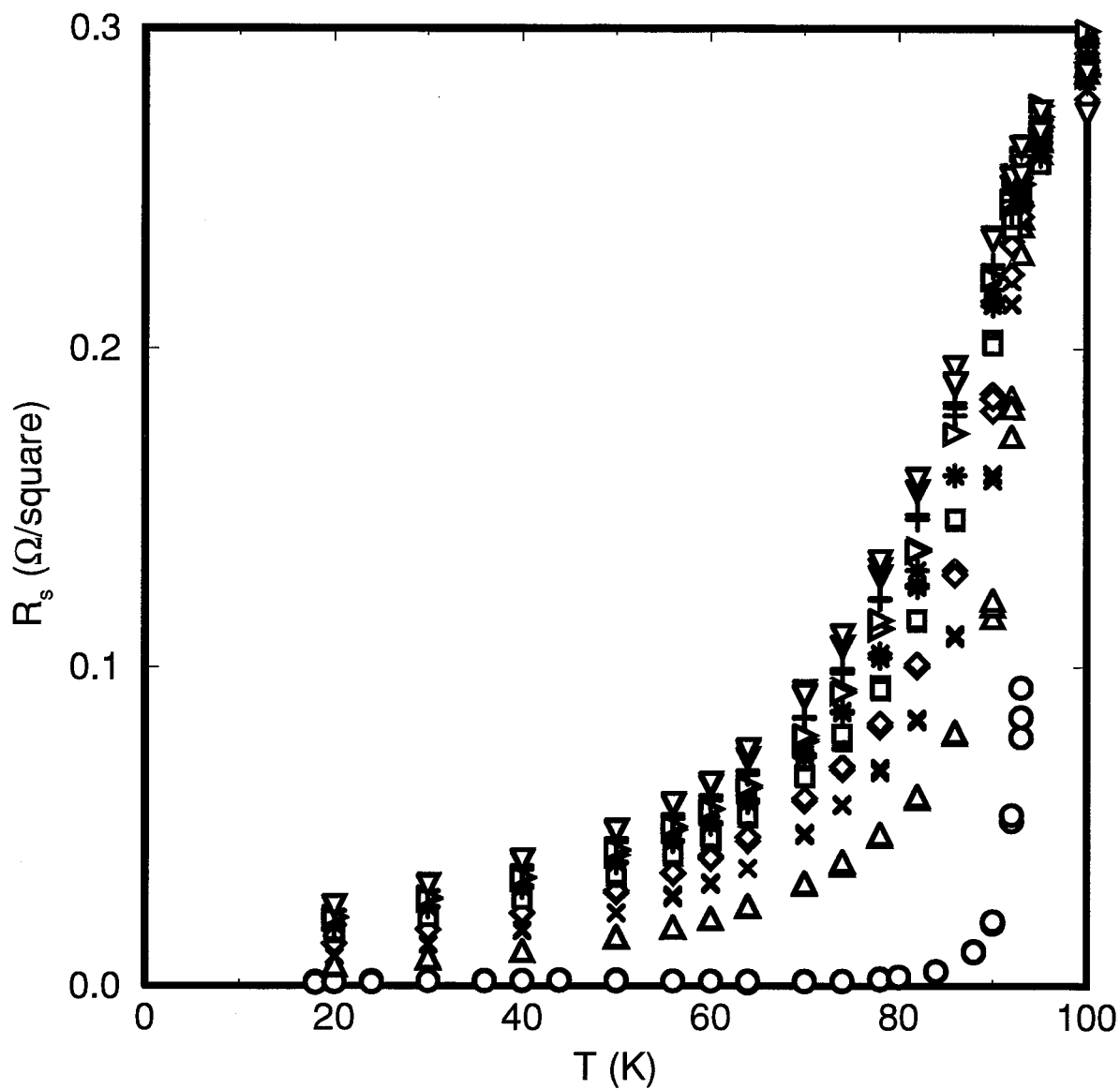
Figure 5.6: Temperature dependence of R_s in a magnetic field at 27 GHz. $\bigcirc$ 0T; $\triangle$ 1T; $\times$ 2T; $\diamondsuit$ 3T; $\square$ 4T; $*$ 5T; $\triangleright$ 6T; $+$ 7T; $\triangledown$ 8T.

Chapter 6

The Analysis

6.1 Overview of the Data

Figure 6.1 shows the measured surface resistance as a function of temperature in a magnetic field of 4T for all three frequencies. The 27 and 35 GHz data have been scaled by factors of $(5.4/27)^{1/2}$ and $(5.4/35)^{1/2}$ respectively to facilitate the comparison. Since for a metal in the classical skin-effect limit R_s is proportional to $\omega^{1/2}$, this operation should result in the curves being brought into coincidence above T_c . However, at 5.4 GHz the sample is not much thicker than the normal state skin depth, and so above T_c there are enhanced losses as is evidenced in the figure. Below T_c , however, and certainly below 78K, the skin depth is much reduced and we can therefore directly compare the 5.4 GHz data and the 27 and 35 GHz data. It is immediately apparent that below 70K, the 5.4 GHz surface resistance is greatly suppressed compared to the 27 and 35 GHz surface resistance. The two higher frequencies scale reasonably well with the square root of the frequency although at low temperatures the 27 GHz data begins to drop below the 35 GHz result. This behaviour suggests the picture of flux-flow at high temperatures where the data at all three frequencies scale roughly as $\omega^{1/2}$ like an effective metal. It also suggests temperature dependent pinning frequencies in the range of 5 - 35 GHz which are large at low temperatures and which decrease with increasing temperature.

This basic picture is reinforced by looking at the data in a slightly different way. Figure 6.2 shows R_s versus B at all three frequencies at low and high temperature.
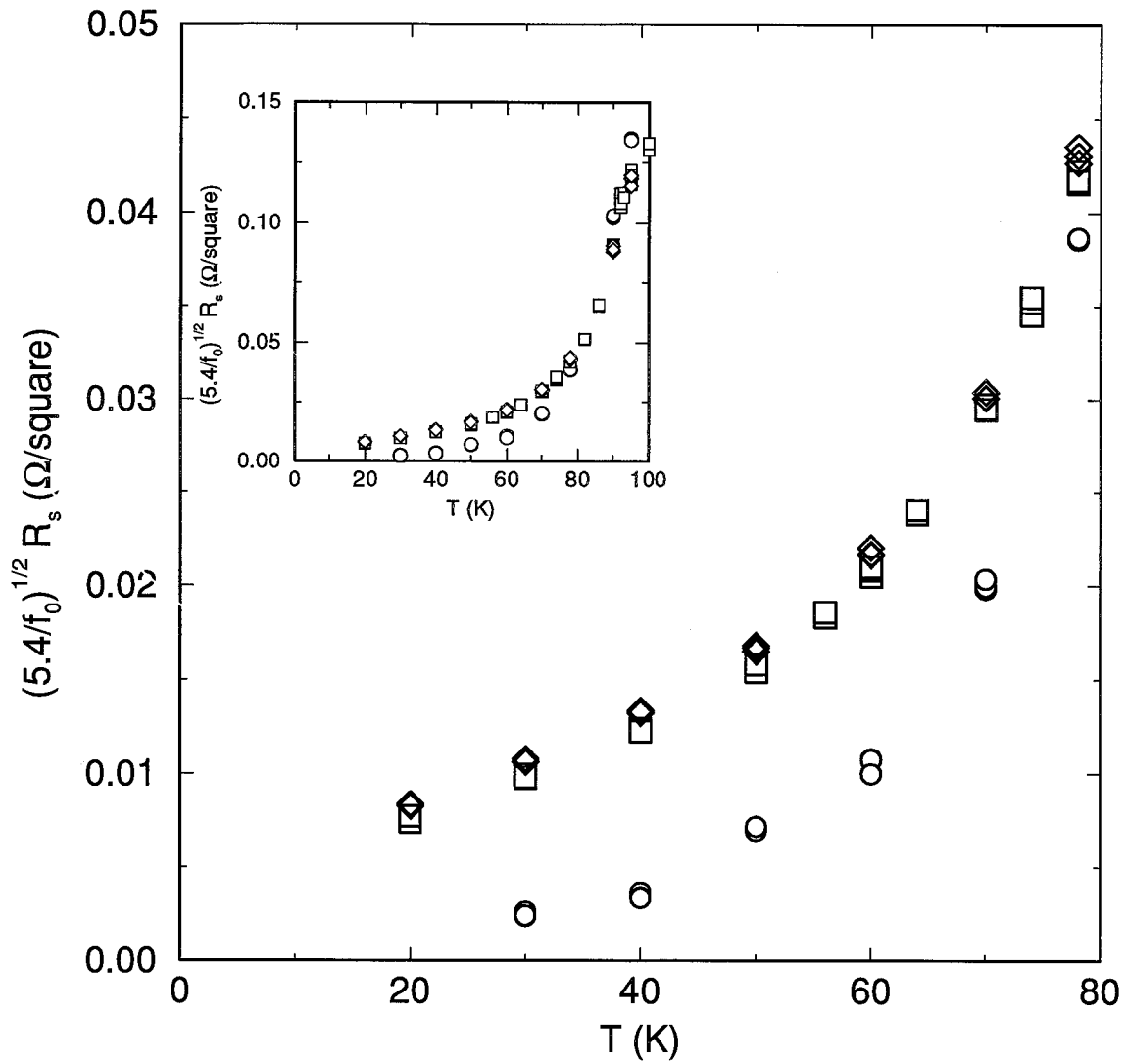
Figure 6.1: $(5.4/\text{frequency})^{1/2}R_s$ at 4T for 5.4, 27 and 35 GHz. ◯: 5.4 GHz; □: 27 GHz; ◇: 35 GHz. The 5.4 GHz data drops clearly below the higher frequency data at low temperatures indicating that pinning is playing a role at this frequency.
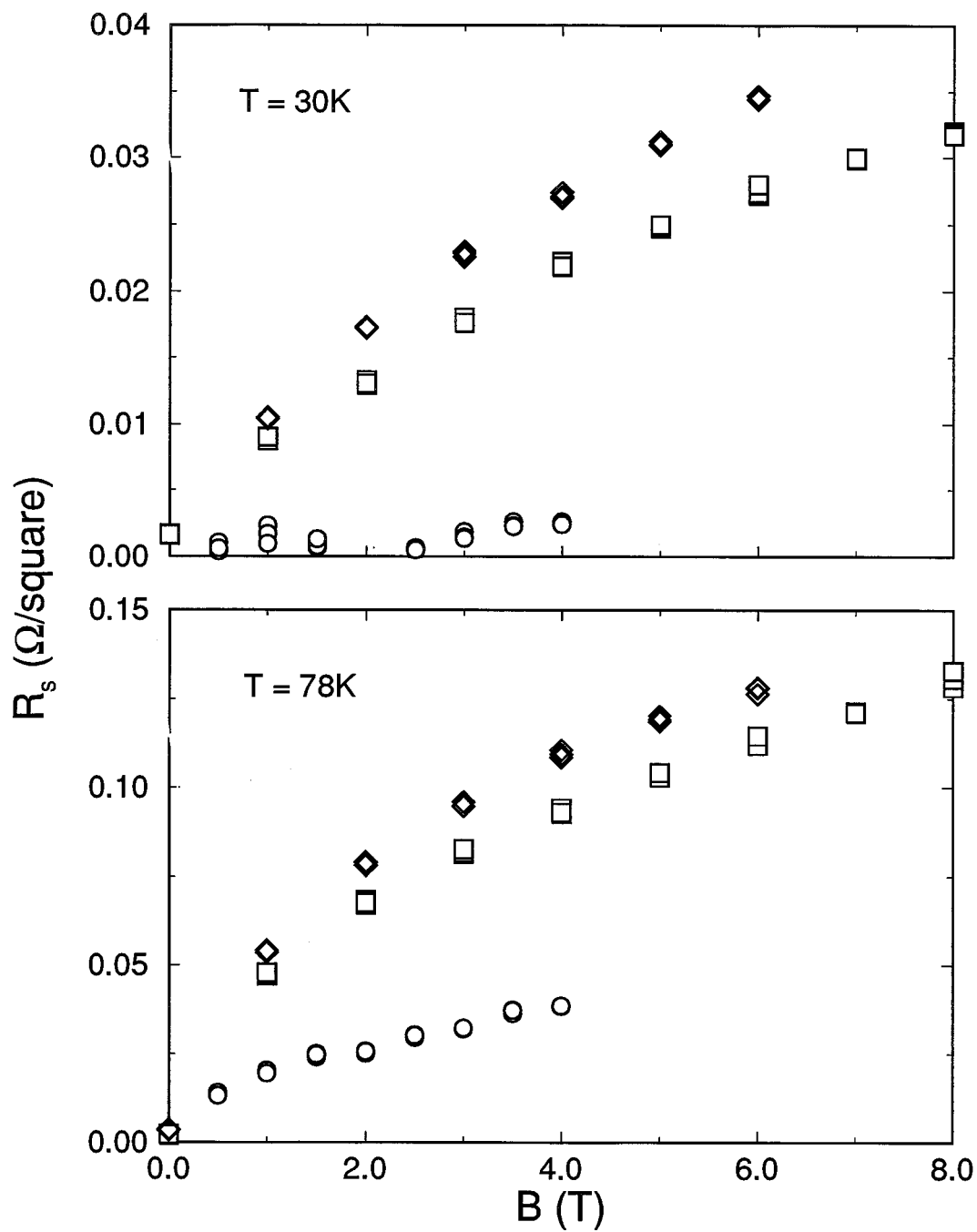
Figure 6.2: Magnetic field dependence of R_s for all three frequencies at 30 K and 78 K. ◯: 5.4 GHz; □: 27 GHz; ◇: 35 GHz. Clearly, at 30K, the loss at 5.4 GHz is greatly suppressed with respect to the higher frequency data.

Again, we see that at 30K, the 5.4 GHz data is greatly suppressed with respect to the 27 GHz and 35 GHz data while at 78K it has increased to the point that it is scaling roughly as $\omega^{1/2}$ with the two higher frequencies. Again, this suggests a temperature dependent pinning frequency that is probably larger than 5.4 GHz at 30K and probably less than 5.4 GHz at high temperature.

Another way of seeing the difference at low and high temperature is to plot R_s against ω for a given field and temperature. Figure 6.3 shows this for low and high temperature on a log-log plot. At low temperature, the low frequency point is well below the line of slope 1/2 which represents $\sqrt{\omega}$ scaling, whereas at high temperature, the scaling is approximately square-root like.

In figure 6.4, R_s^2 versus B at 27 GHz has been plotted and indicates that R_s has a roughly square-root dependence on the magnetic field. Ignoring the λ_L^2 term in the Coffey-Clem expression (which we reproduce here for convenience)

$$\tilde{\lambda} = \left[\frac{\lambda_L^2 - i\,\tilde{\rho}_v/\mu_0\,\omega}{1 + 2\,i\,\lambda_L^2/\delta_{nf}^2} \right]^{1/2} \quad ; \quad \tilde{\rho}_v = \frac{\Phi_0\,B}{\eta\,(1 - i\,\omega_p/\omega)} \tag{6.1}$$

we showed in Chapter 3 that $R_s \propto \sqrt{B}$ in both the flux-flow and flux-pinned regime (ignoring any field dependence in κ_p and η). Thus, the field dependence is consistent with this. However, it is not clear that the λ_L^2 term is completely negligible especially at the higher frequencies where the mixed state skin depth decreases. Thus the non-linear portions at low temperature in the R_s^2 curves for low fields could be due to the λ_L^2 in the numerator of the Coffey-Clem expression 6.1 The λ_L^2 term increases in importance for low fields and low temperatures where B is small and ρ_{ff} is likely to be small also.

Another feature of the data is the role played by fluctuations in determining R_s as $H \rightarrow H_{c_2}$. We have already discussed the pronounced rounding of the dc resistive transition starting at about 20K above T_c . Thus as $H \rightarrow H_{c_2}$, R_s takes on a value given by the fluctuation dominated ρ_{dc}. This fact must be kept in mind when we look
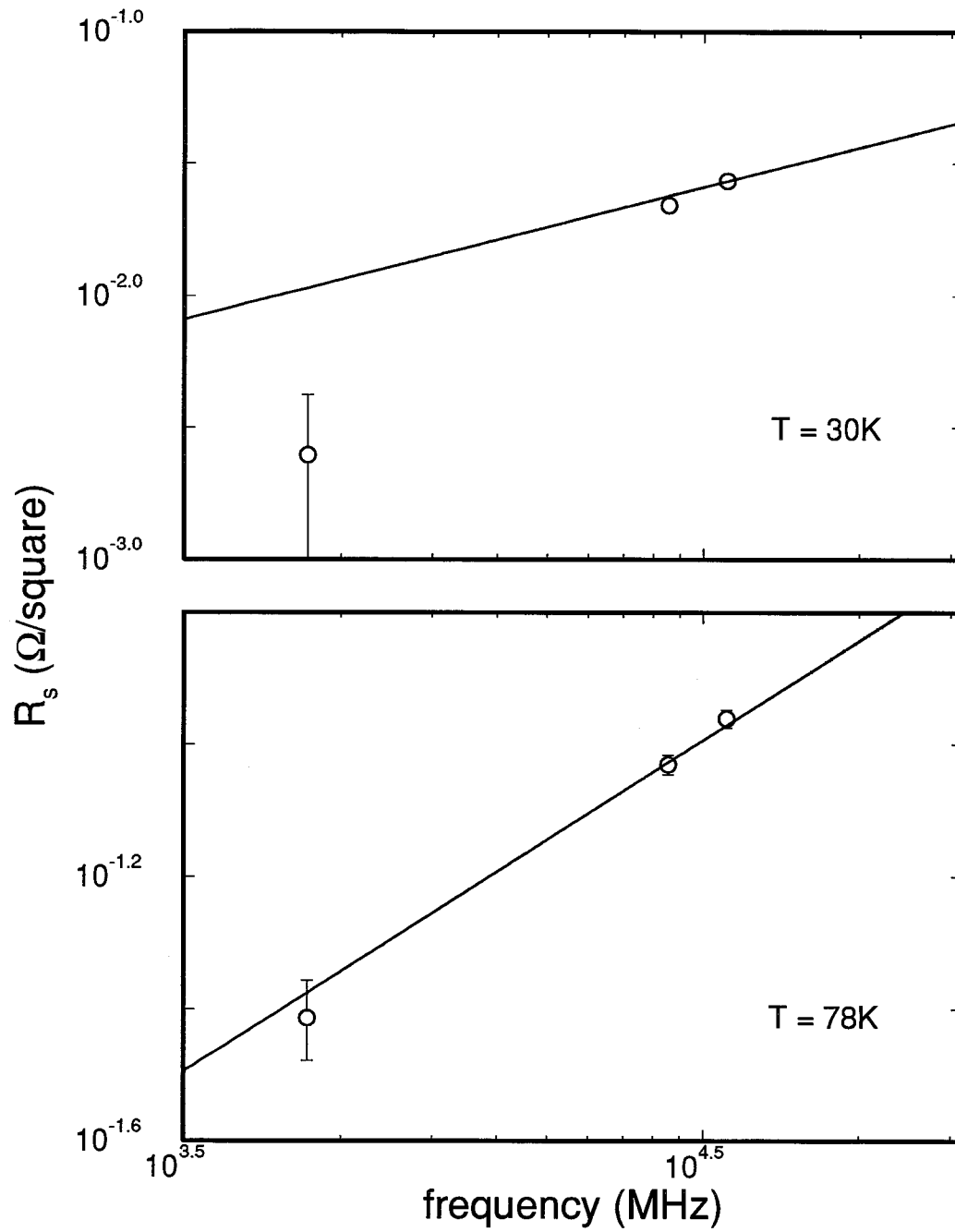
Figure 6.3: Frequency dependence of R_s at low and high temperature at 4T. At low temperature, the 5.4 GHz point is well below a square-root frequency dependence.
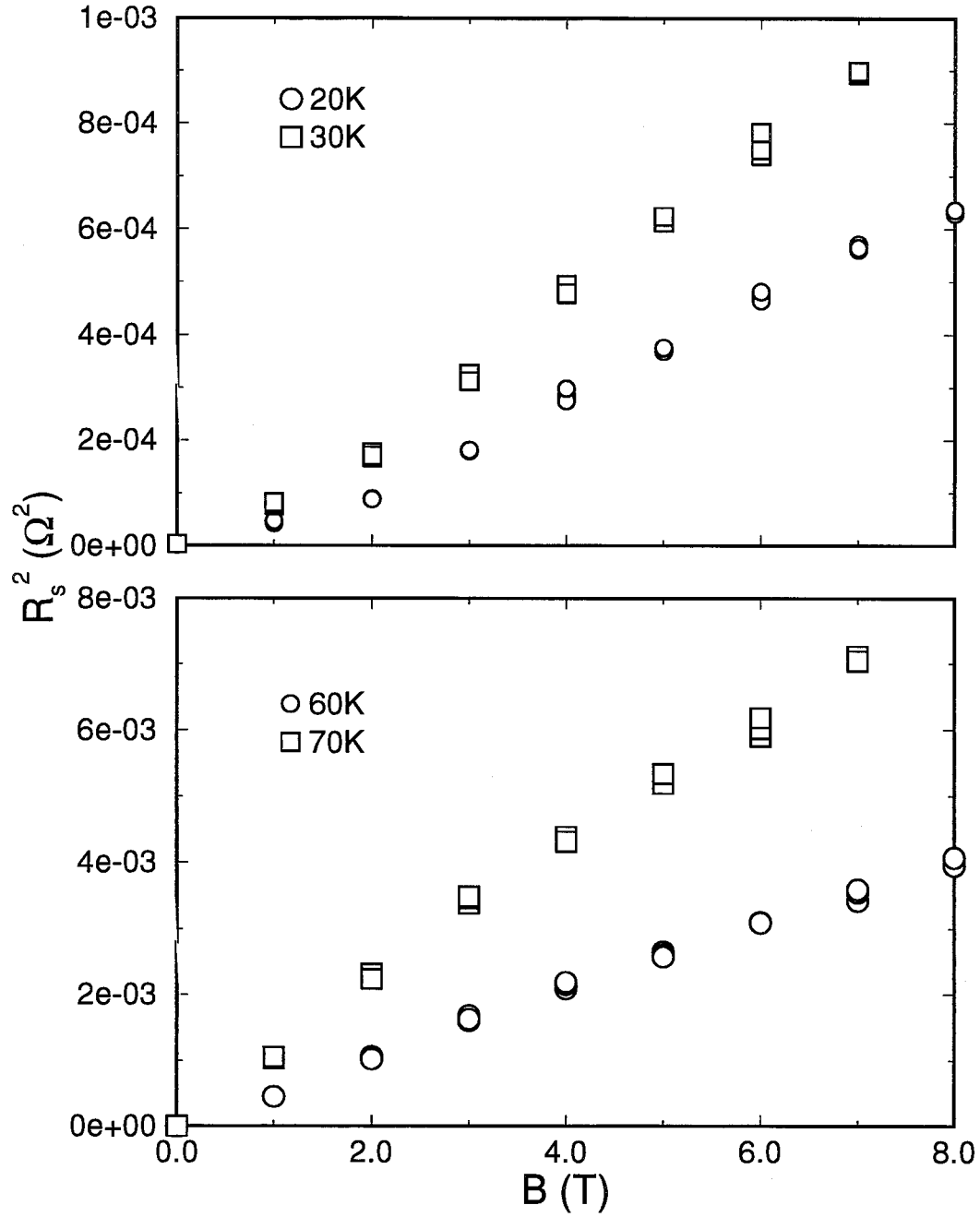
Figure 6.4: Magnetic field dependence of R_s^2 at 27 GHz. At low temperatures the curvature for small fields is due, presumably, to the presence of the λ_L^2 term. At higher temperatures, R_s is looking more square-root like.

at the field dependence of R_s and related quantities when H is not small compared to H_{c_2} . For example, figure 6.5 shows R_s at 27 GHz scaled by a normal state surface resistance obtained using a resistivity extrapolated from the linear portion of the normal state resistivity from above T_c and plotted as a function of $H/H_{c_2}(T)$ where $H_{c_2}(T)$ is given by the empirical expression in Chapter 2. It seems reasonable (we will discuss this in greater detail in section 6.3) to use the linear resistivity to set the scale for the surface resistance for temperatures away from T_c and H_{c_2}. Indeed, for temperatures above 70K, scaling the data in this way does a good job of mapping the field sweeps onto a universal curve (for temperatures 70K and below, we are presumably seeing suppressed loss and surface resistance due to pinning). However, R_s/R_n does not go to 1 as H/H_{c_2} goes to 1 nor should we expect it to, because as $H/H_{c_2} \to 1$, fluctuation effects start to enter. This can also be seen in the $(R_s/R_n)^2$ versus H/H_{c_2} plot (inset in figure 6.5) where the data looks roughly linear for low fields but begins to curve over at higher fields as fluctuations take over.

Clearly, we would like to get a view of the data uncontaminated by pinning effects. What we are really interested in, after all, is the flux-flow resistivity or equivalently the vortex viscosity. This process will be described in the next section.

6.2 Extraction of the pure flux-flow resistivity

6.2.1 Preliminary discussion

We will be using the Coffey-Clem expression for the surface impedance from equation 6.1. However, before we do, we must address an important issue: Does it make sense to use this expression given the geometry of the sample and the rf fields in our experimental setup? The Coffey-Clem expression is derived with the boundary condition $\mathbf{h}_{rf}$ parallel to the surface of the sample. However, in both the 5.4 GHz split-ring resonator and the
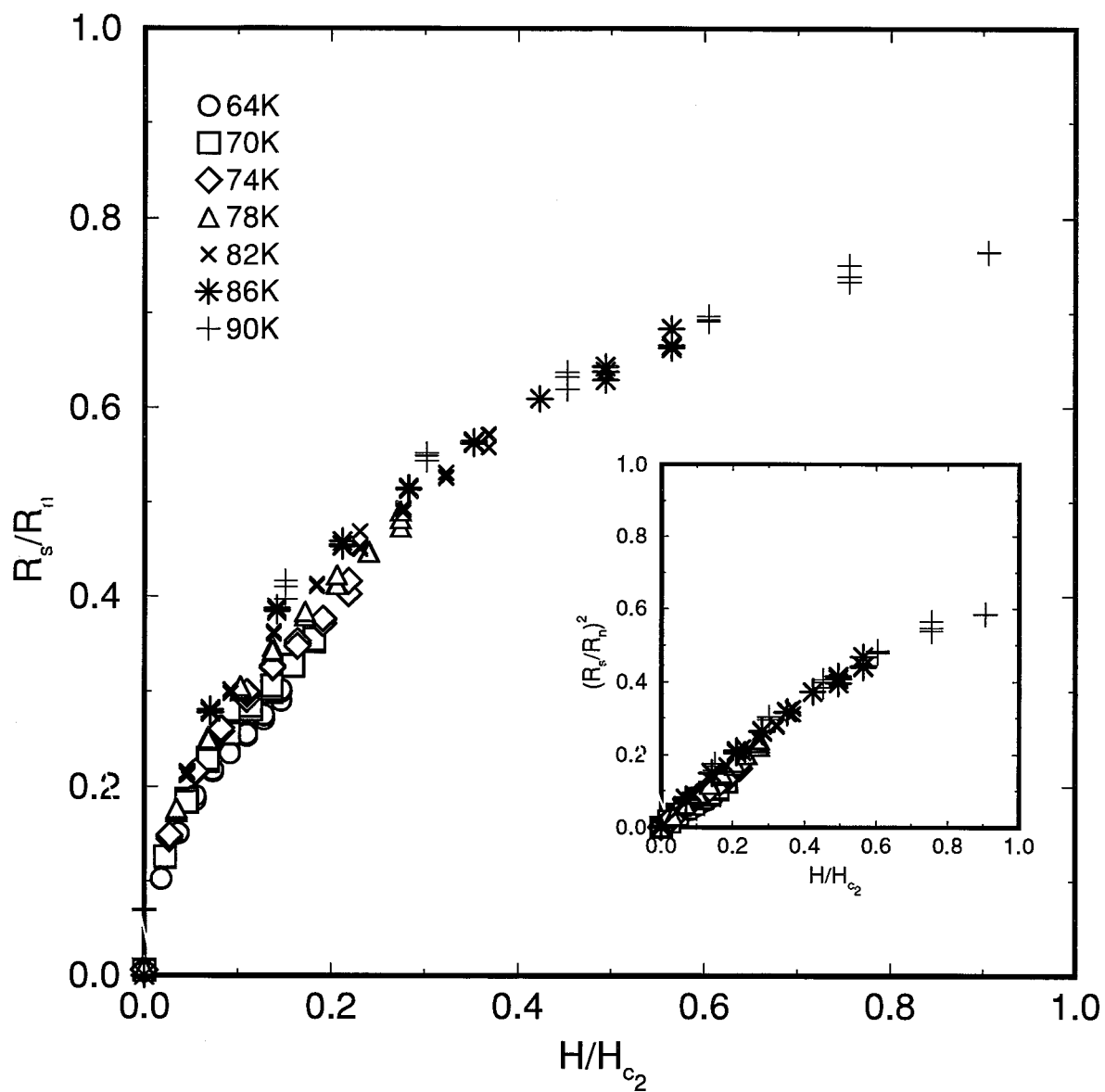
Figure 6.5: Normalized R_s versus reduced field at 27 GHz. This scaling does a reasonable job of mapping the data onto a universal curve

27 and 35 GHz cylindrical cavities we place the sample into perpendicular $\mathbf{h}_{rf}$ fields. To solve this problem in general is quite complicated (involving demagnetizing factors etc.) but we do know the qualitative solution to the problem. The $\mathbf{h}_{rf}$ fields will bend around the sample and the current distribution will be non-uniform and concentrated principally around the edges of the sample on the top and bottom surfaces near to the edges (see Appendix B). The current is distributed so as to screen the $\mathbf{h}_{rf}$ field or, equivalently, to maintain the boundary condition that $\mathbf{h}_{rf}$ be always parallel to the surface. So as far as the physics of the material is concerned, the two geometries are equivalent; it is the current distribution which is different. We argue that this non-uniform current distribution does not produce different physics for the following reasons: the screening currents all run in the a-b plane and the relevant quantity is the a-b plane penetration depth — c-axis currents are not involved; the single crystals are of high quality and the superconducting properties are not expected to vary over the surface of the sample (this has been explicitly verified in numerous zero-field experiments on many different crystals — in addition Kuan Zhang, Walter Hardy and Saied Kamal[72] have measured R_s with $\mathbf{h}_{rf}$ tangential to the surface and similar results are always observed); the surface resistance has been found to be independent of power for the range of low power used in these experiments, and so the varying power in the surface currents near and around the edge of the sample should always give the same value for the surface impedance (which, after all, is just the ratio of the $\mathbf{e}_{rf}$ and $\mathbf{h}_{rf}$ at the surface).

One other point that must be mentioned is that on the edges of the sample the vortices are parallel to the surface while on the top and bottom surfaces the vortices are perpendicular. However, we noted in Chapter 3 that Coffey and Clem have shown that these two situations give rise to the same expression for the surface impedance. Not included in the Coffey-Clem calculation is the possibility of vortex bending. We assume that this does not play a role. Given the anisotropic nature of high-T_c superconductors

and the small displacements of the vortices from their equilibrium position with very high frequency currents, this is probably not a bad assumption.

Equation 6.1, for the surface impedance has four unknowns: λ_L, σ_n, η, and κ_p. λ_L is the London penetration depth, and for this we use the penetration depth of Hardy et al measured on single crystals made with the same technique (assuming $\lambda_L(0) = 1500\mathring{A}$). For the field dependence we use the Ginzburg Landau expression $\lambda_L(B) = \lambda_L(0)/\sqrt{1 - B/B_{c_2}}$. σ_n is the real part of the conductivity for the quasiparticles in the normal fluid in the bulk of the superconductor. This can be simply extracted from the zero-field R_s versus T curve using $\lambda_L(T)$ (see discussion of the zero field data of Bonn et al in Chapter 2). We do this for only one frequency although it is likely the σ_n is mildly frequency dependent in the range 5 to 35 GHz. Such details are in fact almost irrelevant. The value of σ_n only enters in the denominator as part of the expression $1 + 2i\lambda_L^2/\delta_n^2$ which approximately equal to 1 until we are within a degree of T_c (where λ_L diverges). We are thus left with two unknowns: η and κ_p. We can write the surface impedance expression in terms of η and $\omega_p = \kappa_p/\eta$ (see equation 6.1) and we choose to do the fitting in terms of these parameters.

The remaining question is then how to do the fitting. However, before we discuss the fits in detail, our perspective on this whole process should be reiterated: we are really only interested in ω_p or κ_p to the extent that it affects our ability to reliably extract the flux-flow resistivity. The pinning strengths and frequencies are very likely to be sample dependent and influenced by factors such as twin density and impurity concentration. Also, the concept of a single pinning frequency is itself highly questionable since in general we might expect a distribution of pinning strengths and frequencies. ω_p should be regarded as an *effective* pinning frequency. It represents our best effort, given the limited frequency information available, at modelling the pinning and removing its effects from the data. Thus our discussion of the pinning strengths and frequencies will

be restricted to qualitative features and orders of magnitude.

6.2.2 Fitting with a field dependent η and ω_p

We expect both η and ω_p to be temperature dependent. The nature of any field dependence is less clear; however, assuming a field independent η, for example, is equivalent to enforcing a flux-flow resistivity that depends linearly on the field and given the previous experiments on other superconductors this hardly seems justified, (there is no compelling precedent for assuming ω_p to be independent of field either). It seems reasonable to assume that both η and ω_p are independent of frequency. Indeed, the whole phenomenology of ac effects in the mixed state makes this assumption. Thus for every field and temperature at which we have three frequency points, we can fit for η and ω_p. For $B > 4T$, and certain temperatures such as 20K and 78K $< T <$ 90K, data at all three frequencies is not available; in fact, at some fields and temperatures there is only one frequency point (the most complete data set was obtained at 27 GHz). At 20K, we simply solve for ω_p and η using the 27 and 35 GHz points while for $T > 78$ K, the pinning frequency is small enough (see figure) that we can just set it to zero and use the 27 GHz point to determine η.

The fits were performed using the MINUIT fitting program and are given in figures 6.6 – 6.12. The error bars on the data points result almost entirely from the uncertainty in the overall calibration constants used at each of the three frequencies. As described in Chapter 5, the 27 and 35 GHz data were both calibrated by using the classical skin effect formula and assuming a dc resistivity at 100K typical of the U.B.C. $YBa_2Cu_3O_{6.95}$ single crystals. There is a variation from crystal to crystal of $\sim \pm 10\%$ in $\rho_{dc}(100K)$[17]. The 5.4 GHz data was calibrated using a reference sample whose dc resistivity was known. There is thus an uncertainty of at least $\sim \pm 10\%$ in the relative value of R_s at 5.4 GHz with respect to R_s at 27 and 35 GHz. Because the 27 and 35 GHz data were calibrated
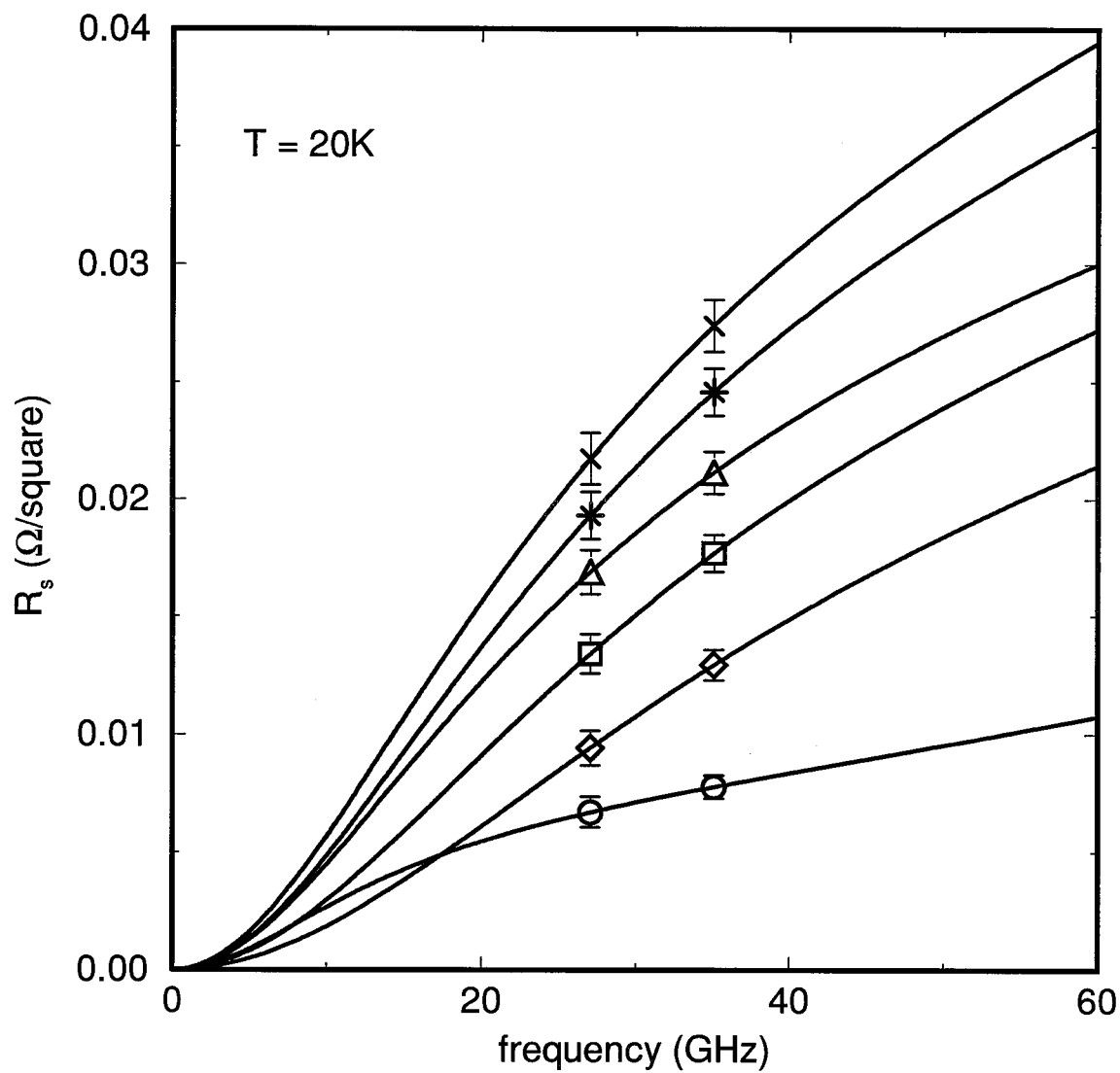
Figure 6.6: Frequency fits at 20 K. $\bigcirc$: 1T; $\diamondsuit$: 2T; $\square$: 3T; $\triangle$: 4T; $*$: 5T; $\times$: 6T. In fact, these are not fits but solutions of the Coffey-Clem expression for the two parameters η and ω_p using the two frequency points at each field.
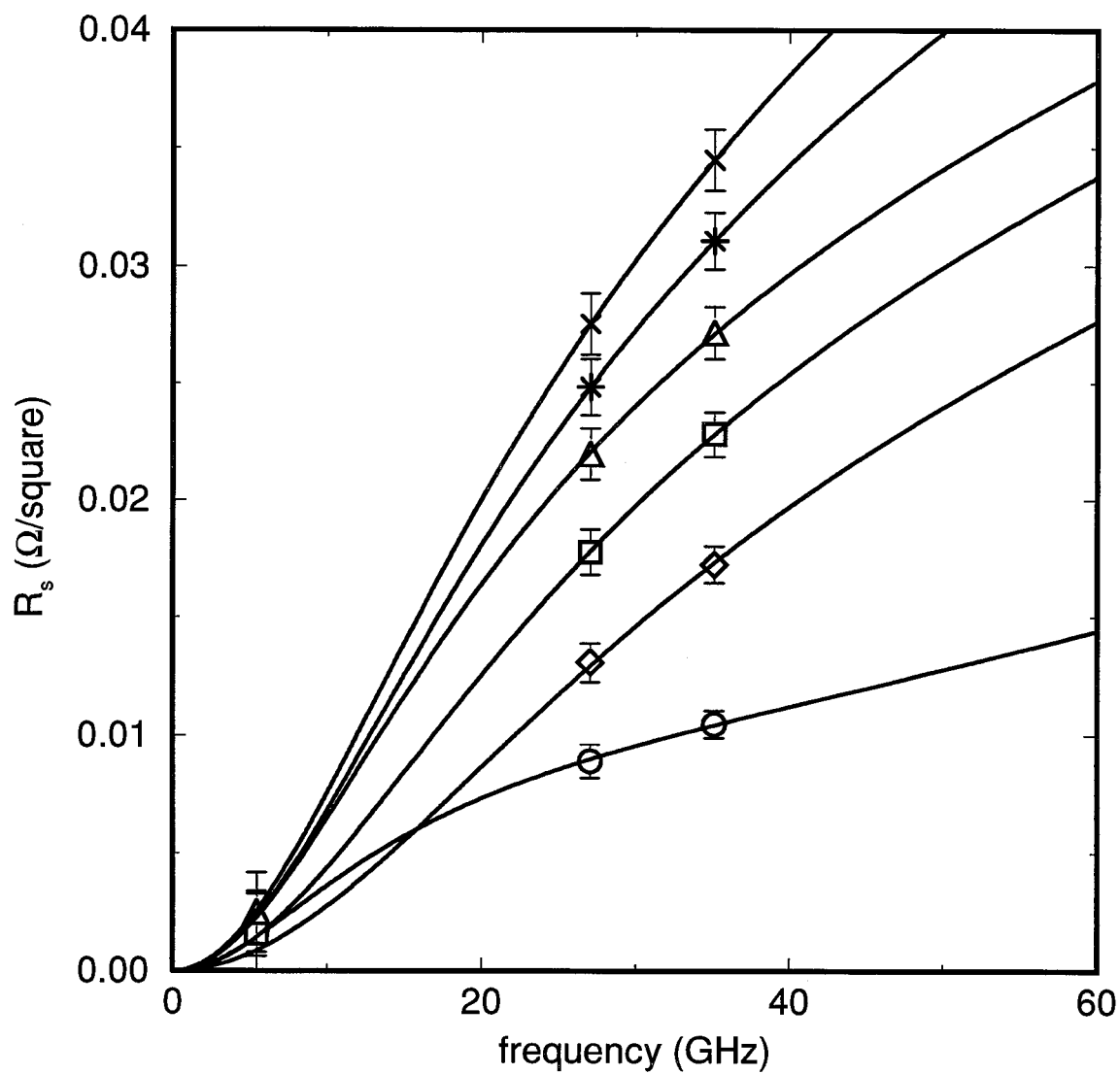
Figure 6.7: Frequency fits at 30 K. $\bigcirc$: 1T; $\Diamond$: 2T; $\square$: 3T; $\triangle$: 4T; $*$: 5T; $\times$: 6T. These fits allow both η and ω_p to be field dependent.
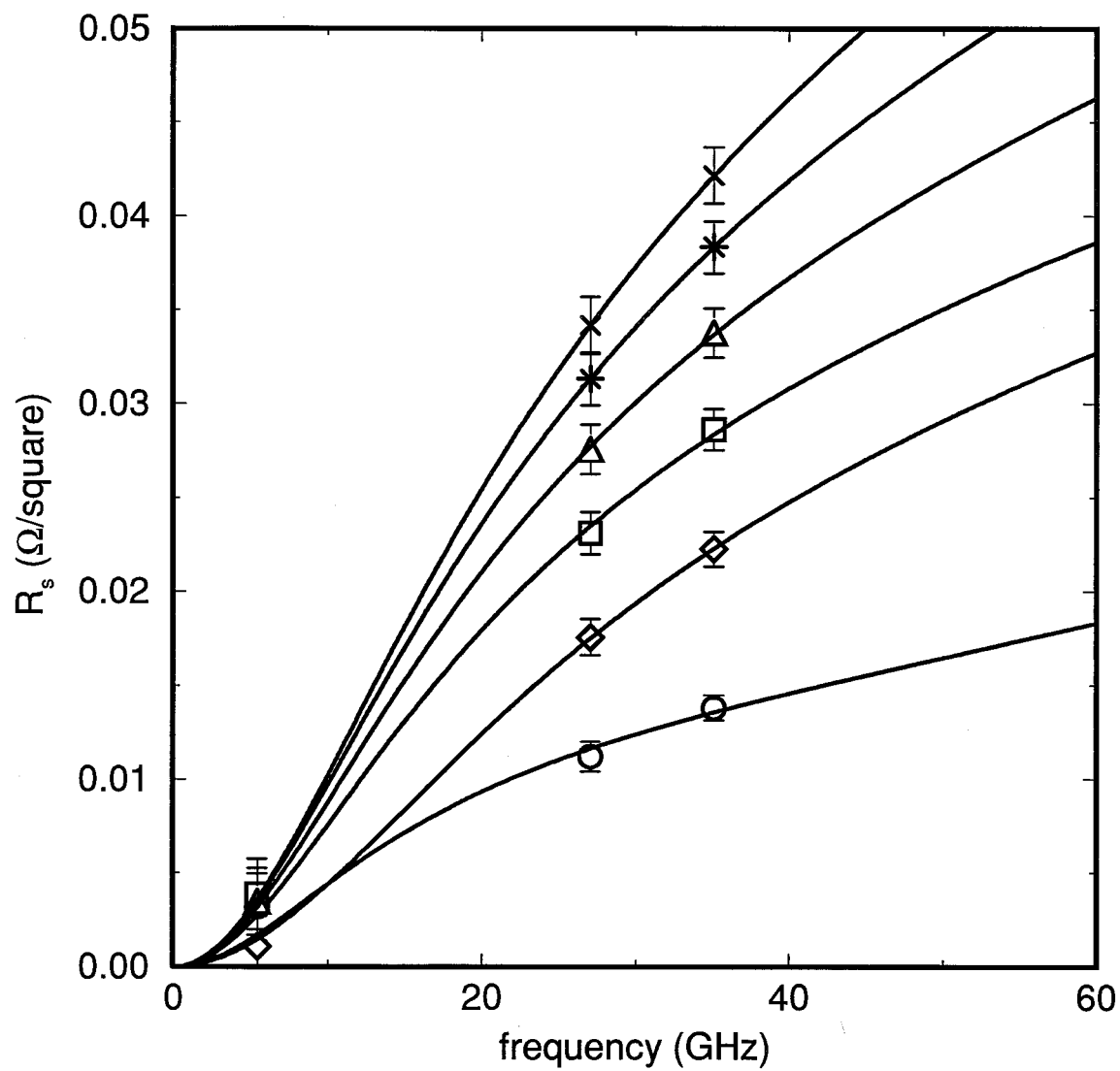
Figure 6.8: Frequency fits at 40 K. $\bigcirc$: 1T; $\Diamond$: 2T; $\square$: 3T; $\triangle$: 4T; $*$: 5T; $\times$: 6T. These fits allow both η and ω_p to be field dependent.

Figure 6.9: Frequency fits at 50 K. $\bigcirc$: 1T; $\diamondsuit$: 2T; $\square$: 3T; $\triangle$: 4T; $*$: 5T; $\times$: 6T. These fits allow both η and ω_p to be field dependent.
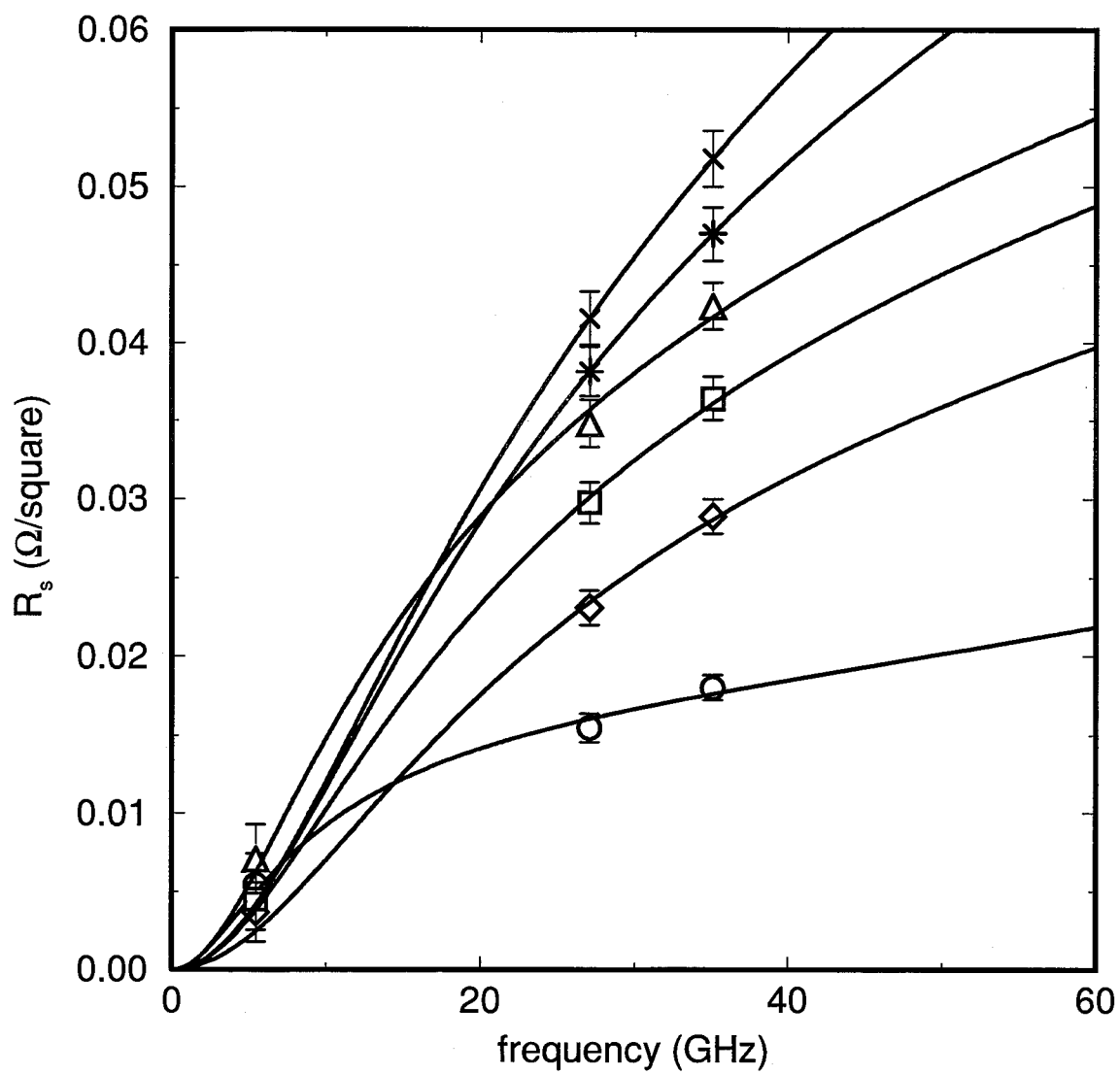
Figure 6.10: Frequency fits at 60 K. $\bigcirc$: 1T; $\diamondsuit$: 2T; $\square$: 3T; $\triangle$: 4T; $*$: 5T; $\times$: 6T. These fits allow both η and ω_p to be field dependent.

Figure 6.11: Frequency fits at 70 K. $\bigcirc$: 1T; $\diamondsuit$: 2T; $\square$: 3T; $\triangle$: 4T; $*$: 5T; $\times$: 6T. These fits allow both η and ω_p to be field dependent.
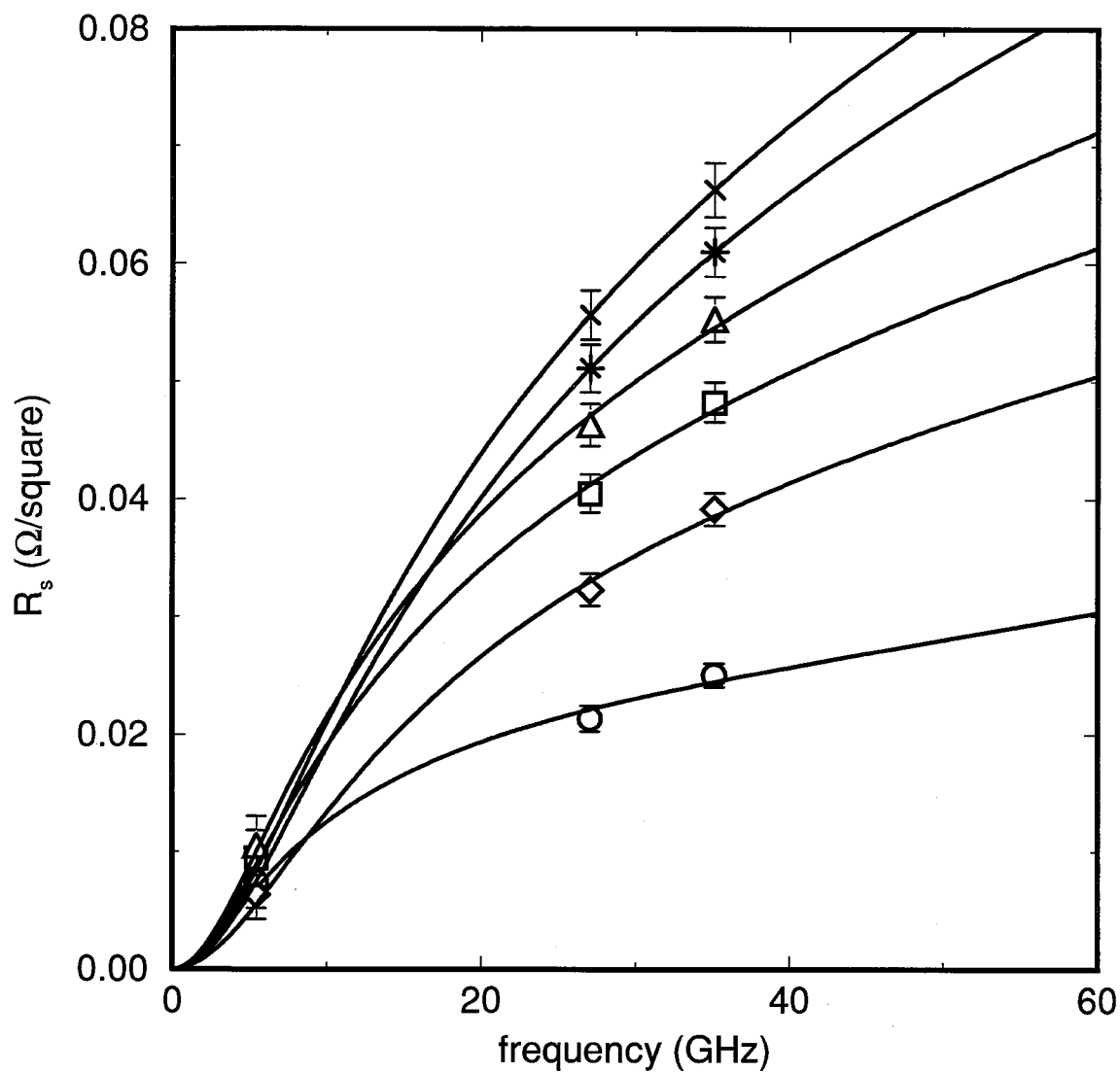
Figure 6.12: Frequency fits at 78 K. ◯: 1T; ◇: 2T; □: 3T; △: 4T; *: 5T; ×: 6T. These fits allow both η and ω_p to be field dependent.
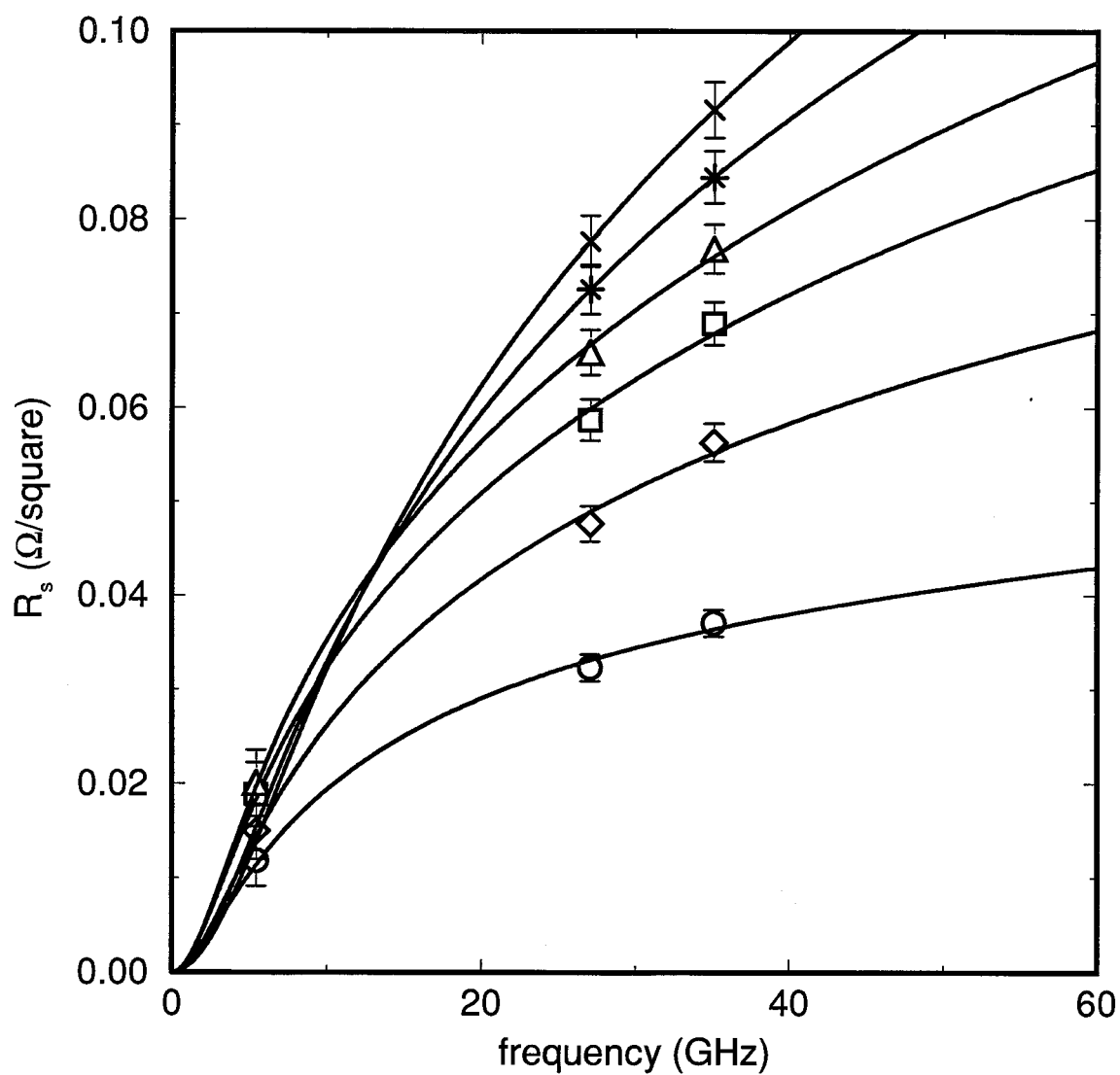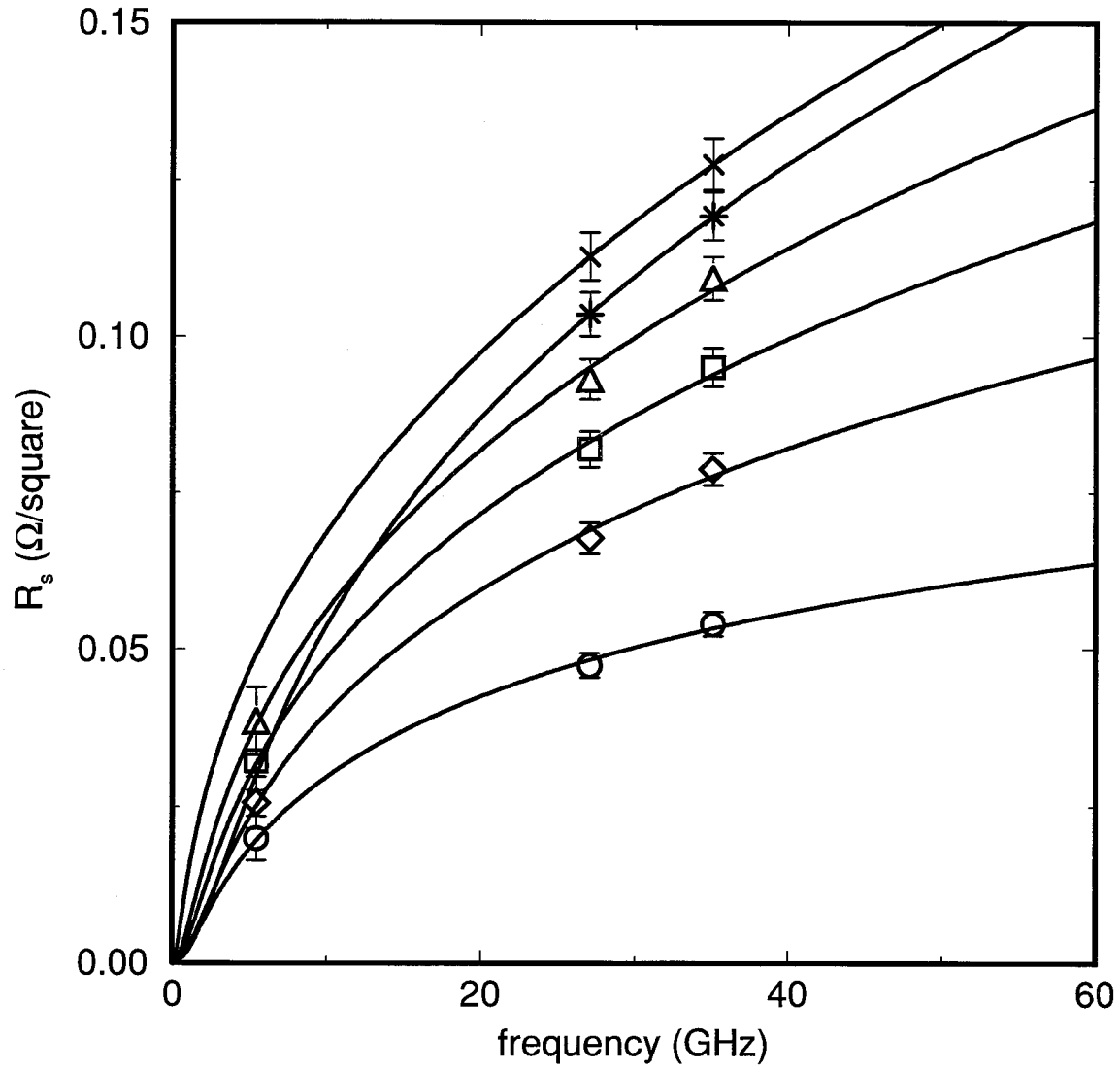
assuming the same value for $\rho_{dc}(100K)$ they are not subject to this $\pm 10\%$ uncertainty - we estimate their relative uncertainties to be $\pm 3\%$. To represent these uncertainties in the absolute value of the surface resistance we have put $\pm 10\%$ error bars on the 5.4 GHz data and $\pm 3\%$ error bars on the 27 and 35 GHz data. Given these error bars, the fits to the data are satisfactory. It should be kept in mind that an error in any one of the calibration constants has the potential to globally affect the look of the fits.

The field dependence of the fitted vortex viscosity values at a given temperature are typified by figure 6.13 which shows η vs B at 82K. At 82K, the pinning frequency is close to zero and so this curve is derived from only the 27 GHz data. However, it is fairly representative of the field dependence at all the temperatures (except possibly for $T < 40K$ where we can fit the data reasonably well with a field independent η — see section 6.2.3): it changes most quickly at low fields and levels off at the higher fields. This suggests the possibility of a genuinely field independent η at higher fields. It also raises the possibility that insufficient knowledge of the London penetration depth and its magnetic field dependence is affecting, at low fields, the quality of the fits and the resultant fitted values of η. At low fields, we are most sensitive to errors in λ_L since the flux-flow term in the numerator is proportional to B whereas the λ_L^2 term probably increases more slowly. Thus, at higher fields, the flux flow term dominates. For example, at 82K, λ_L^2 is 9.7×10^{-14} and the flux-flow term is 13.9×10^{-14} at 1T (still comparable) while at 8T, the ρ_{ff} term becomes 111×10^{-14}. The effect of a field dependent η on ρ_{ff} is to introduce curvature in its field dependence at low fields, gradually straightening out as the field increases. Typically, we expect a linear ρ_{ff} (or field independent η) for fields, $B \ll B_{c_2}$ with η being solely a property of an isolated vortex and independent of the density of vortices. To show the temperature dependence of ω_p and η or ρ_{ff} we will use the 4T data as representative of all fields. It will become evident that the field dependence of η and ω_p is a relatively small effect compared to their temperature
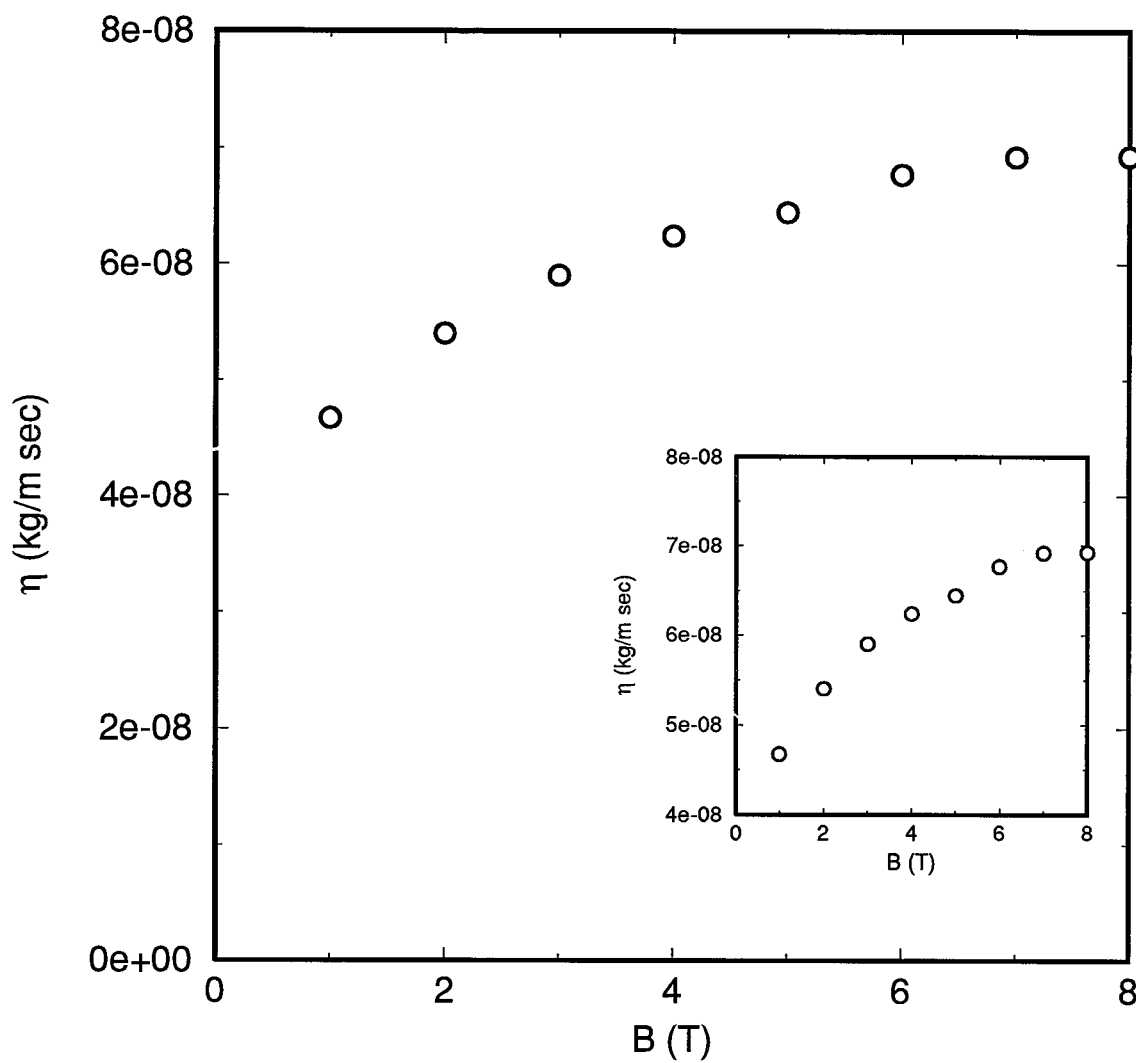
Figure 6.13: Field dependence of the vortex viscosity at 82K. Inset: close-up. η appears to level off as the field increases.

dependence. We will address this issue once again in section 6.2.3.

Figure 6.14 shows ω_p as a function of temperature for $B = 4$T and this curve is representative of the temperature dependence at all fields (with the possible exception of 1T). This is the result which we anticipated in the qualitative overview of the data given in section 6.1. The error bars were generated by the MINUIT fitting program after having been provided with the experimental uncertainties on the individual frequency points. The error bars are large because there are only three data points and the 27 and 35 GHz points are providing information mainly about the flux-flow resistivity. Nearly all the information on the pinning frequency comes from the overall difference in R_s between low and high frequency. We see that the pinning frequency is of the order of 20 GHz at 20K and goes to zero at $T \sim 80K$. Thus at low temperature, all three frequencies are affected by pinning: the 27 and 35 GHz data are slightly reduced from what they would have been in the absence of pinning and the 5.4 GHz data is almost totally suppressed. As the temperature is increased the surface resistance at the two higher frequencies quickly become only slightly affected by pinning while at 5.4 GHz the surface resistance experiences a transition from a flux pinned to a flux-flow regime.

Figure 6.15 shows the temperature dependence of the flux-flow resistivity at 4T. It is highly temperature dependent especially above 50K where it increases rapidly towards its value near T_c . It is not hard to understand how this curve comes out of the fitting given the high frequency R_s curves. Since $R_s \sim \rho_{ff}^{1/2}$, it is clear that this curve mirrors the surface resistance except for the fact that the pinning has been removed. We can substitute this ρ_{ff} back into the Coffey-Clem equation to generate the R_s that we would have measured in the absence of pinning. This is shown in figure 6.16 for $B = 4$T at 27 GHz. We can see that higher loss would have been measured at low temperatures if it hadn't been for pinning effects.

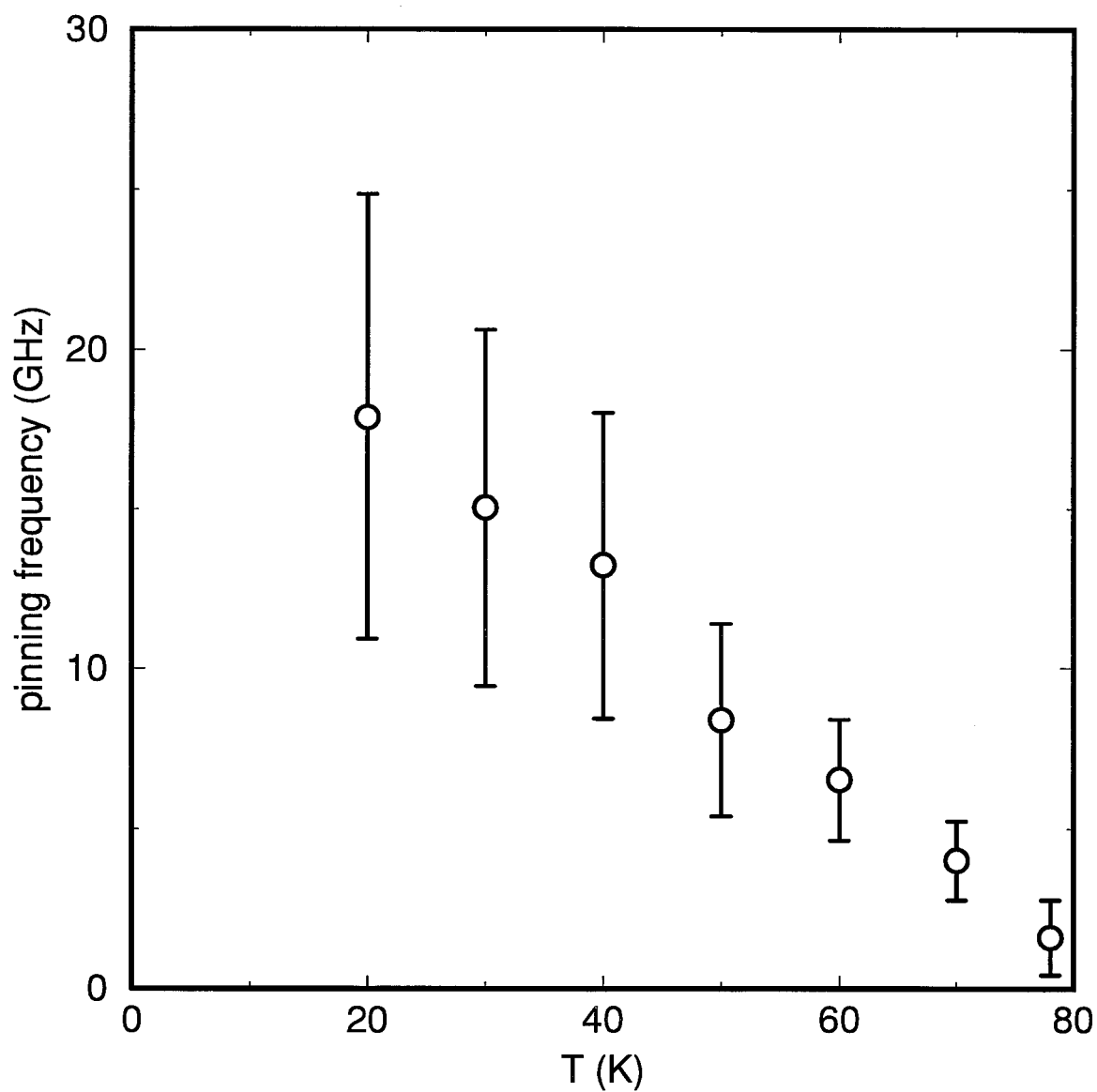In figure 6.17, we have plotted ρ_{ff} against B for the whole range of temperatures

Figure 6.14: Temperature dependence of the pinning frequency at 4 T. At temperatures much above 80 K, we are seeing almost pure flux-flow at all frequencies
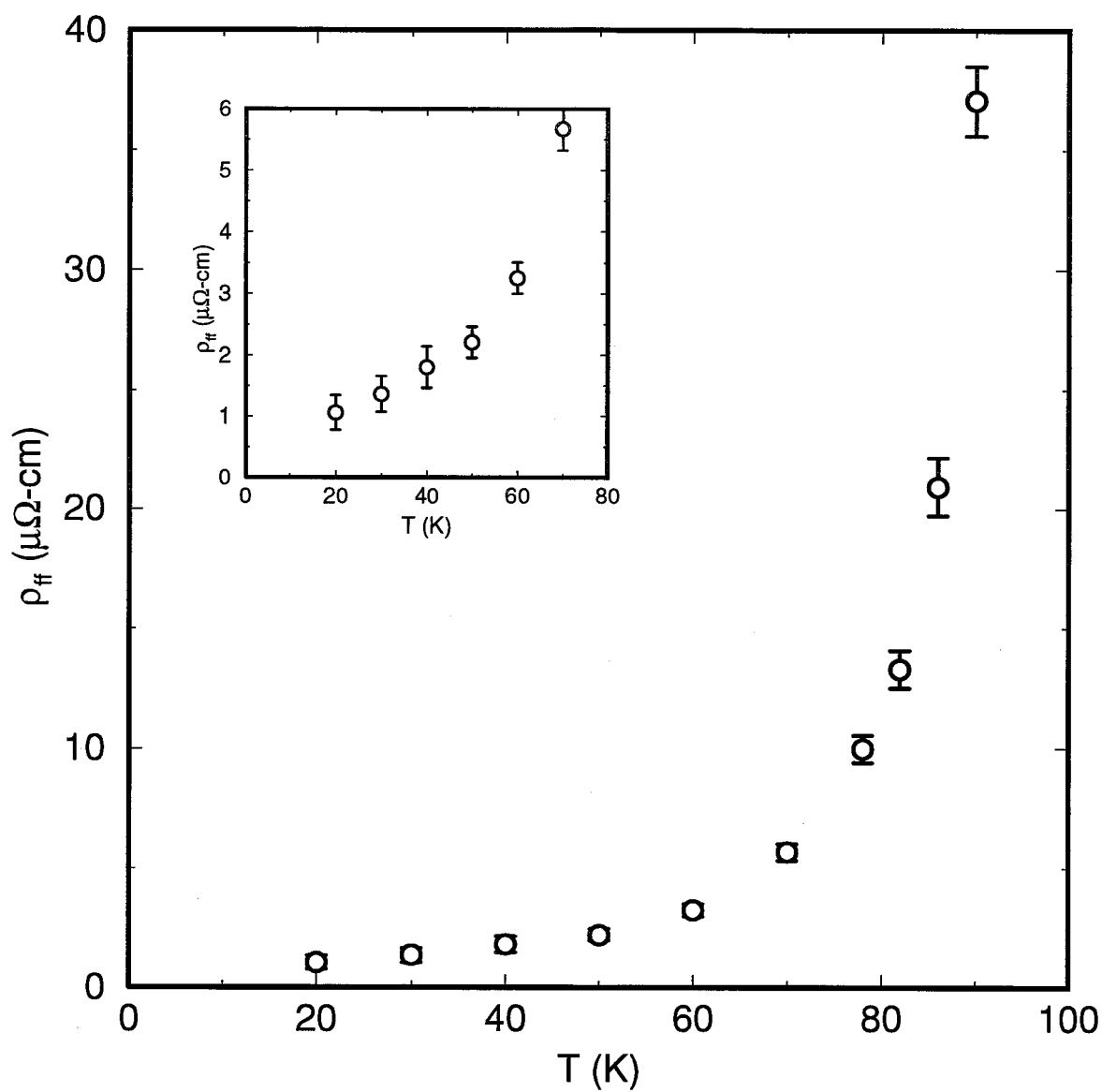
Figure 6.15: Temperature dependence of the flux-flow resistivity at 4 T. Inset: a close-up of the low temperature behaviour.
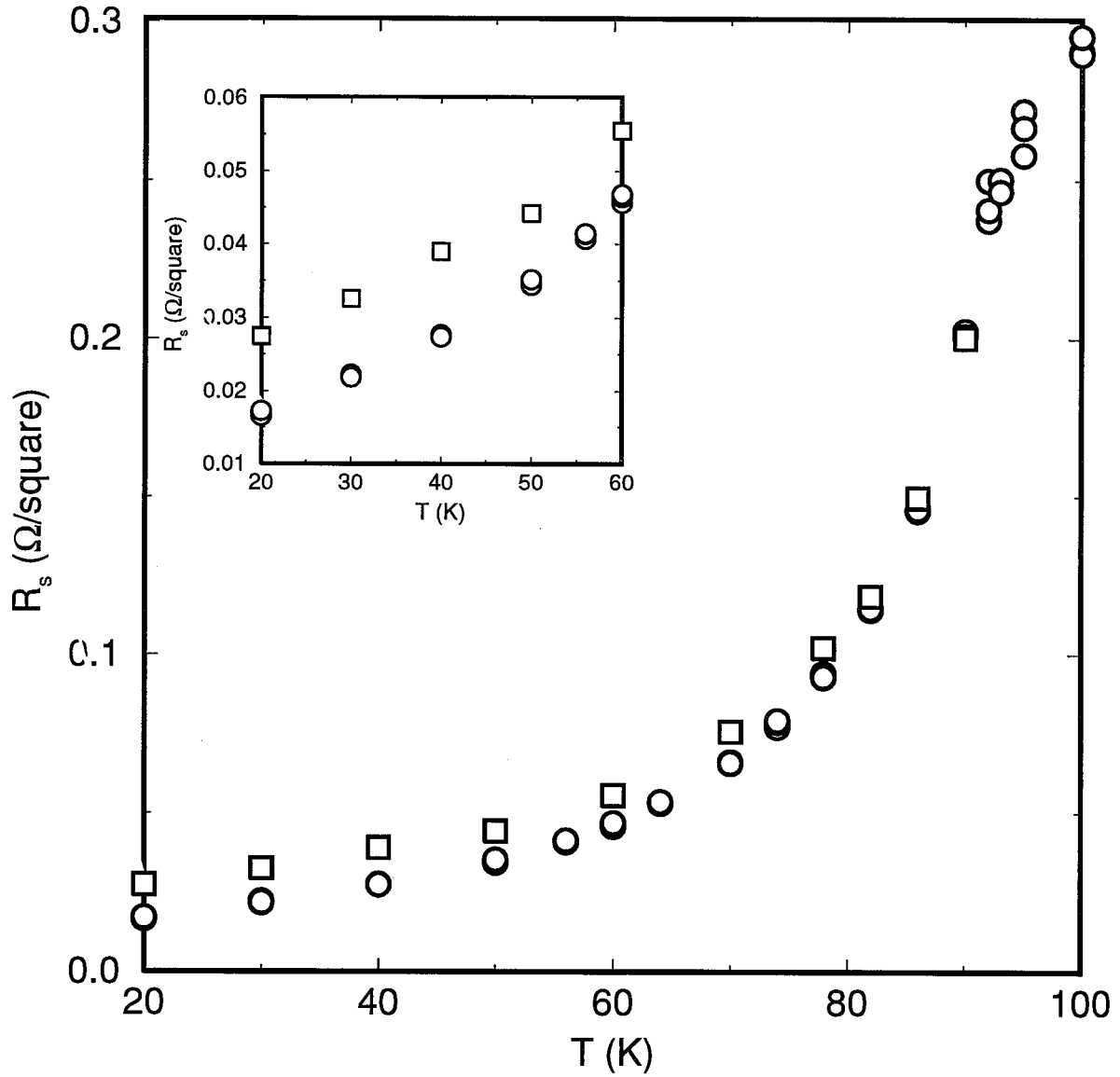
Figure 6.16: Effect of pinning on R_s at 27 GHz in a 4T field. R_s is not affected at high temperature but at low temperature it is suppressed by pinning. The circles show the curve as measured. The squares are R_s generated from the ρ_{ff} data so that the effect of the pinning has been removed and this curve is what we would have measured if there had been no pinning.

studied in these experiments. We can see from these sets of curves that not only is the flux-flow resistivity highly temperature dependent but that it is so in a manner very different from that observed by Kim et al[1] (see figure 3.3). In their data, they only saw temperature dependence once they departed from the low-field linear region. Our data compares better with that of Fogel[3] (see figure 3.4).

6.2.3 Fitting with a frequency and field independent η and ω_p

The problem, of course, with fitting to three data points with two parameters is that we are extremely sensitive to error in any given data point (as we have seen in the previous section especially with the low field data). It is instructive to try fitting the data at all three frequencies and all fields at a given temperature in terms of a frequency and field independent vortex viscosity and pinning frequency. In this situation, we are much less sensitive to fluctuations in the individual data points: at temperatures where we have information at all three frequencies, 22 data points can be included in the fitting in terms of only two parameters. The fits at temperatures 20 - 82 K are shown in figures 6.18–6.25.   At the lowest temperatures, 20 and 30 K, the fits are reasonably good and this gives us some more confidence that the Coffey-Clem model is applicable to our data. At low temperatures, we might indeed expect to fit in terms of a field independent vortex viscosity (equivalently, a flux-flow resistivity that is linear in the magnetic field) especially for $B \ll B_{c_2}$. Note that this good fit in terms of field independent parameters means that the model is correctly describing the characteristic knee in the R_s^2 versus B curve that we have seen in figure 6.4 and that we discussed also in Chapter 3. This is the signature of the λ_L^2 term and would seem to indicate that our value for $\lambda_L(0)$ is not too far off. This further strengthens our conviction that the Coffey-Clem expression is doing a good job of describing the data at these temperatures.

However, the fits are not as good at the higher temperatures. It is important at this
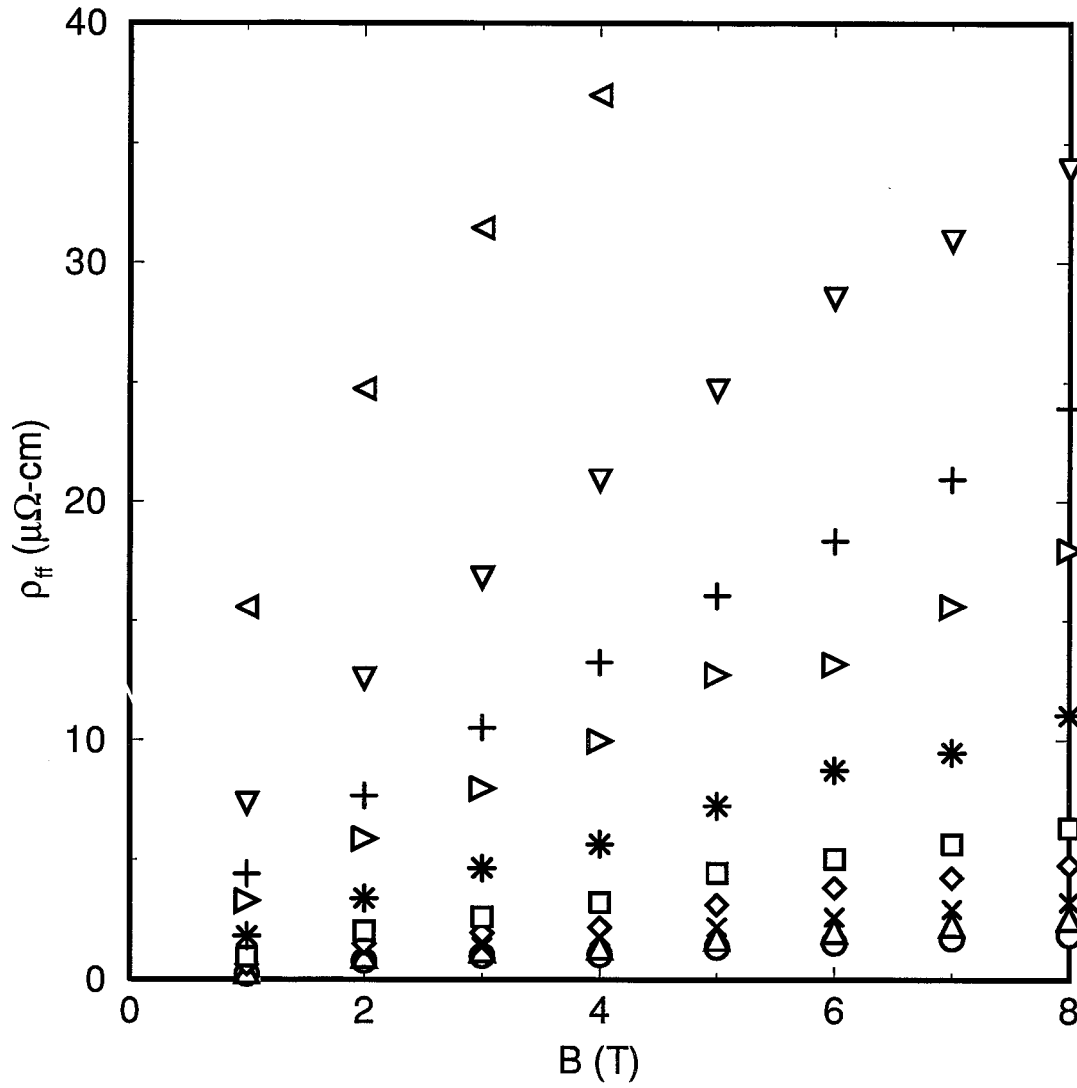
Figure 6.17: Field dependence of the flux-flow resistivity at all temperatures. ◯: 20K; △: 30K; ×: 40K; ◇: 50K; □: 60K; *: 70K; ▷: 78K; + : 82K; ▽: 86K; ◁: 90K. There is strong temperature dependence even at low fields.
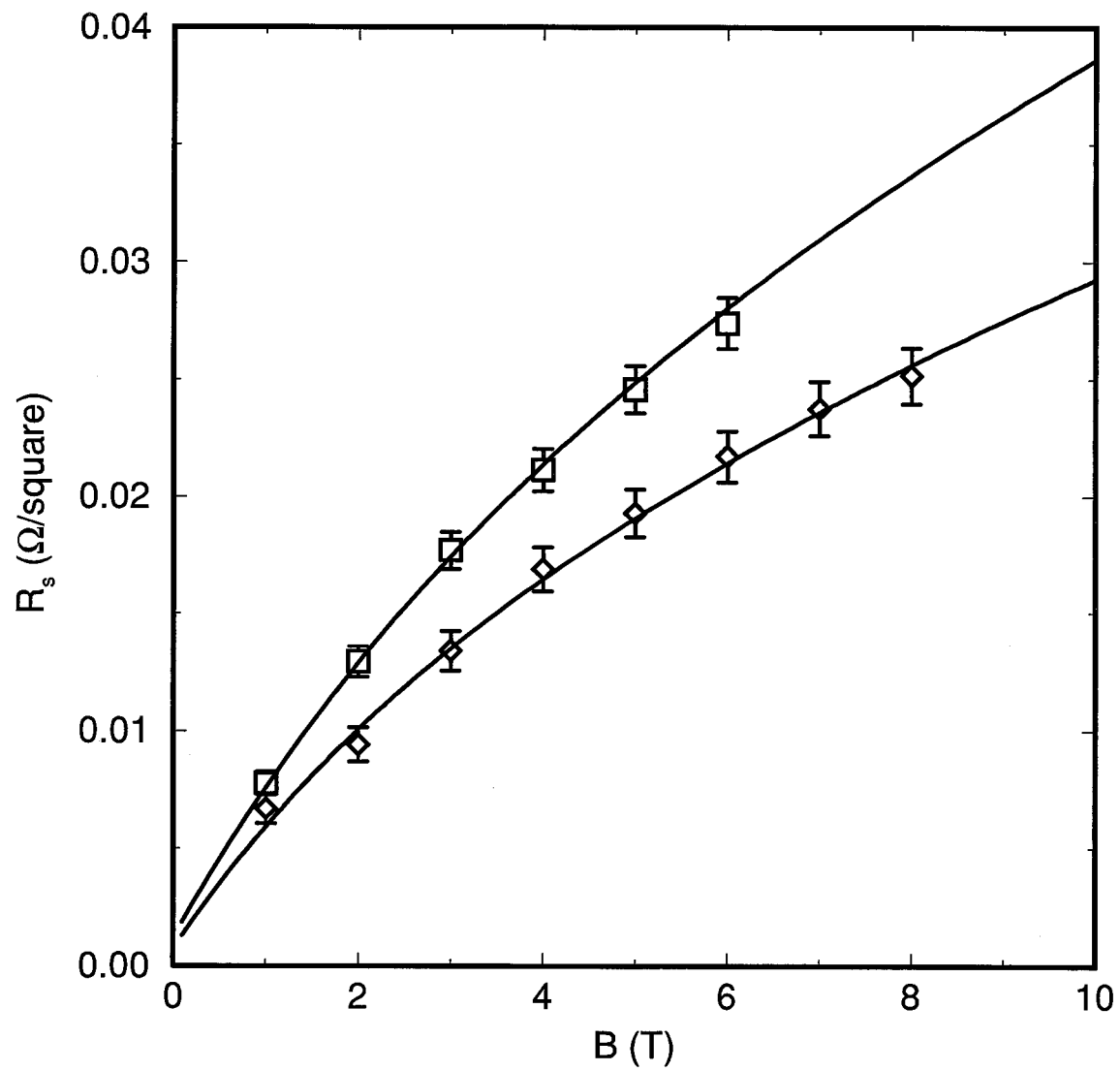
Figure 6.18: Fitting as a function of frequency and field at 20K. $\Diamond$: 27 GHz; $\Box$: 35 GHz. Both η and ω_p are field independent.
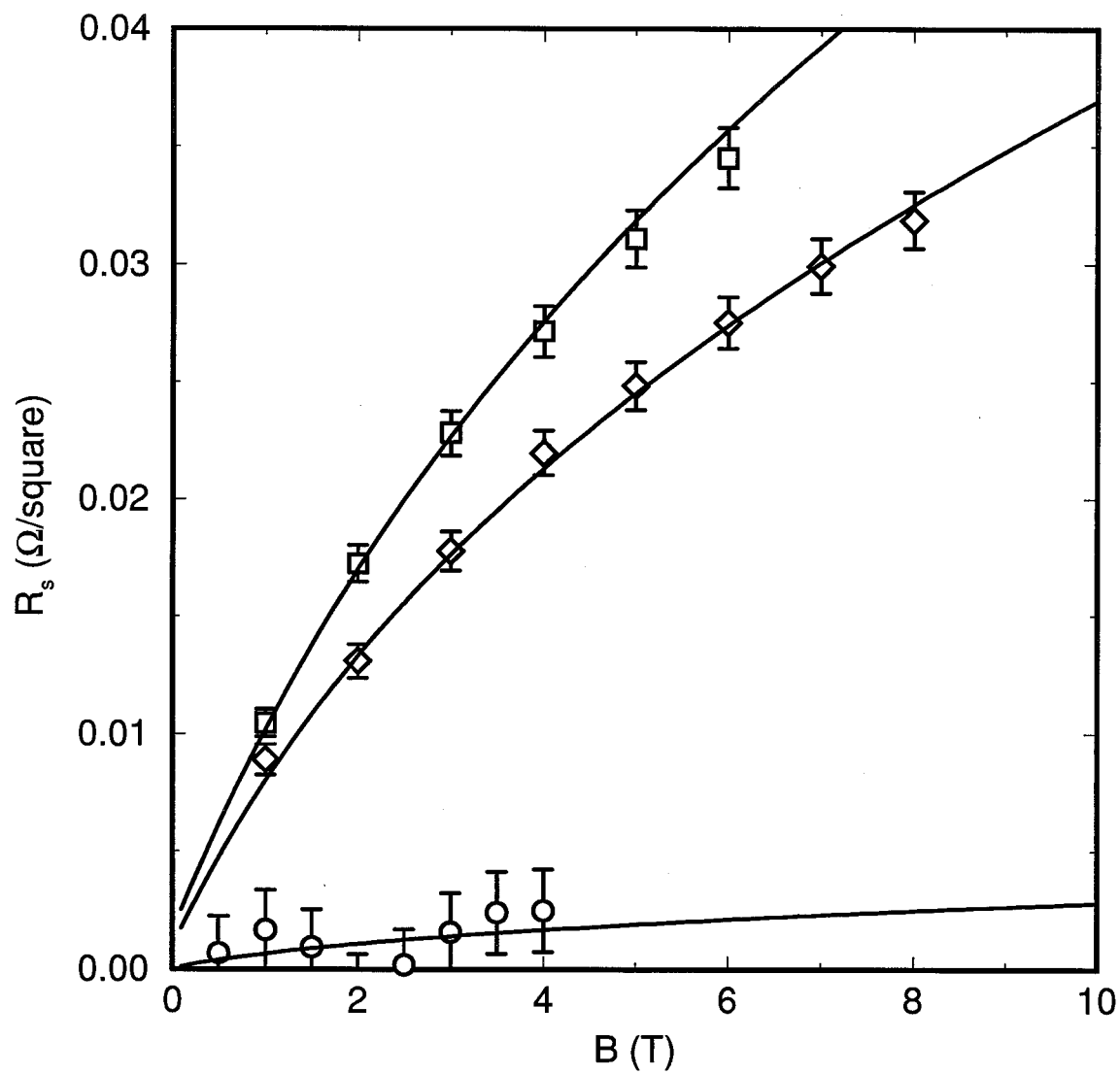
Figure 6.19: Fitting as a function of frequency and field at 30K. ○: 5.4 GHz; ◇: 27 GHz; □: 35 GHz. Both η and ω_p are field independent.
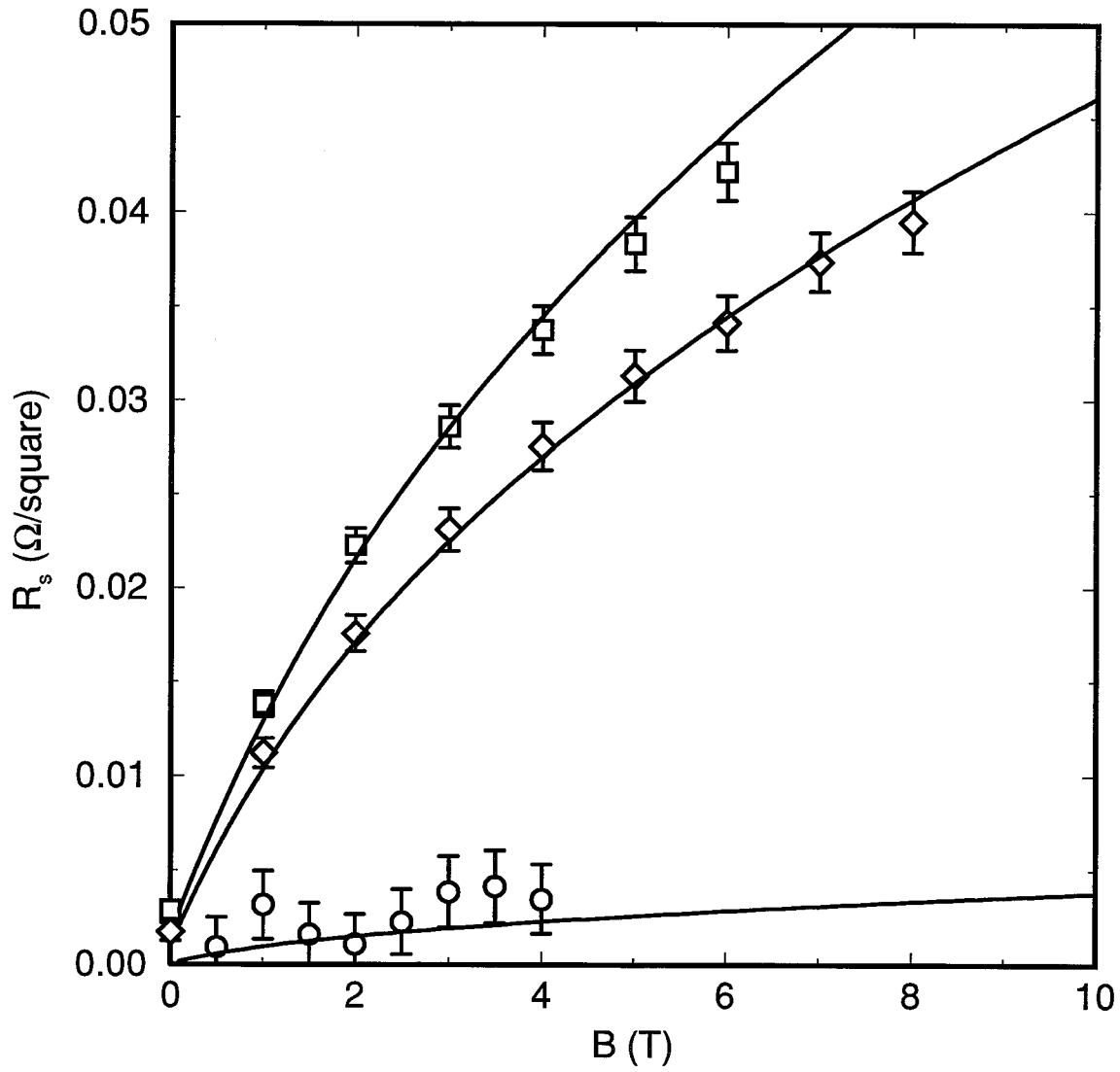
Figure 6.20: Fitting as a function of frequency and field at 40K. $\bigcirc$: 5.4 GHz; $\Diamond$: 27 GHz; $\square$: 35 GHz. Both η and ω_p are field independent.
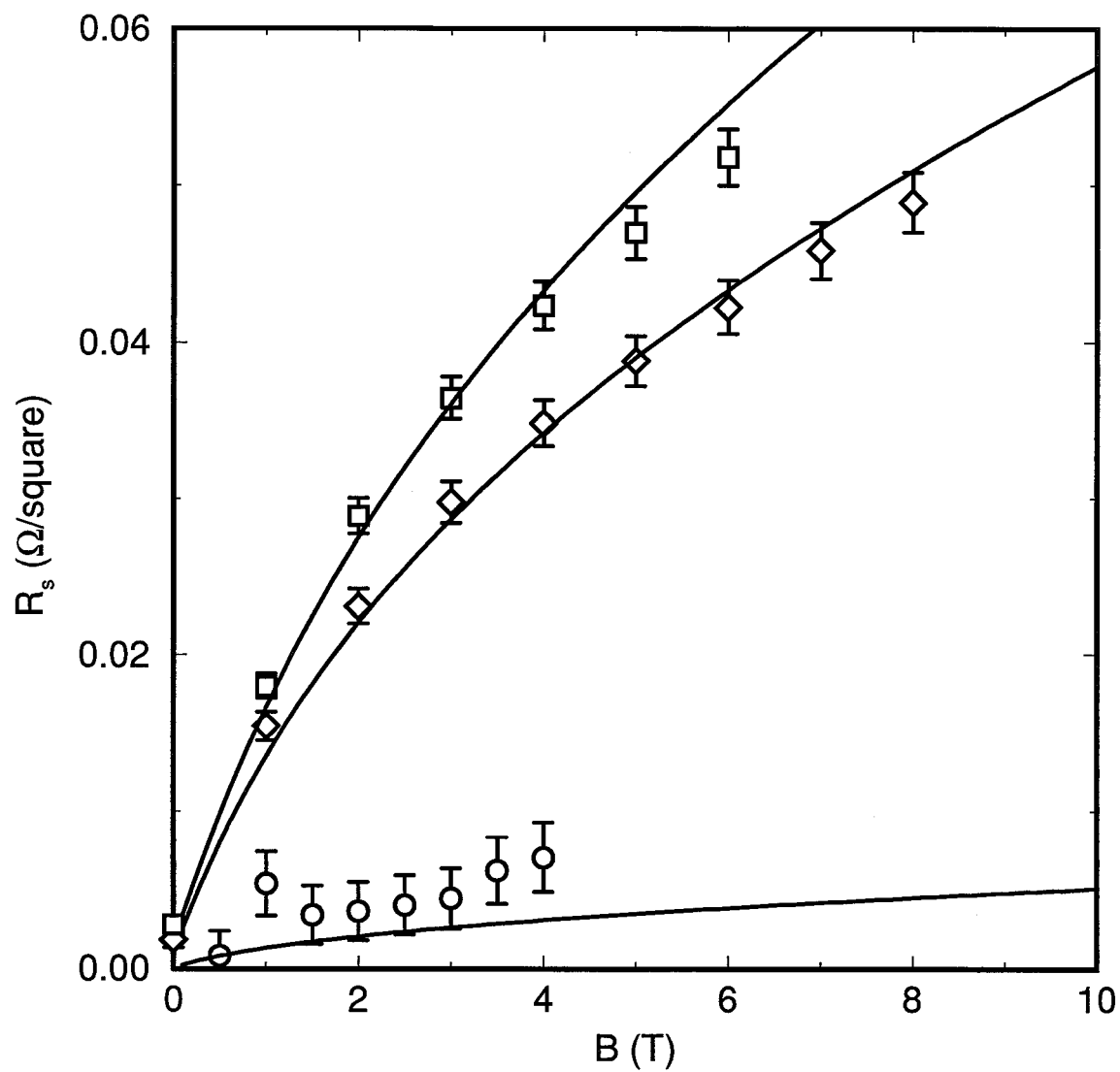
Figure 6.21: Fitting as a function of frequency and field at 50K. $\bigcirc$: 5.4 GHz; $\Diamond$: 27 GHz; $\square$: 35 GHz. Both η and ω_p are field independent.

Figure 6.22: Fitting as a function of frequency and field at 60K. $\bigcirc$: 5.4 GHz; $\diamondsuit$: 27 GHz; $\square$: 35 GHz. Both η and ω_p are field independent.

Figure 6.23: Fitting as a function of frequency and field at 70K. $\bigcirc$: 5.4 GHz; $\Diamond$: 27 GHz; $\Box$: 35 GHz. Both η and ω_p are field independent.

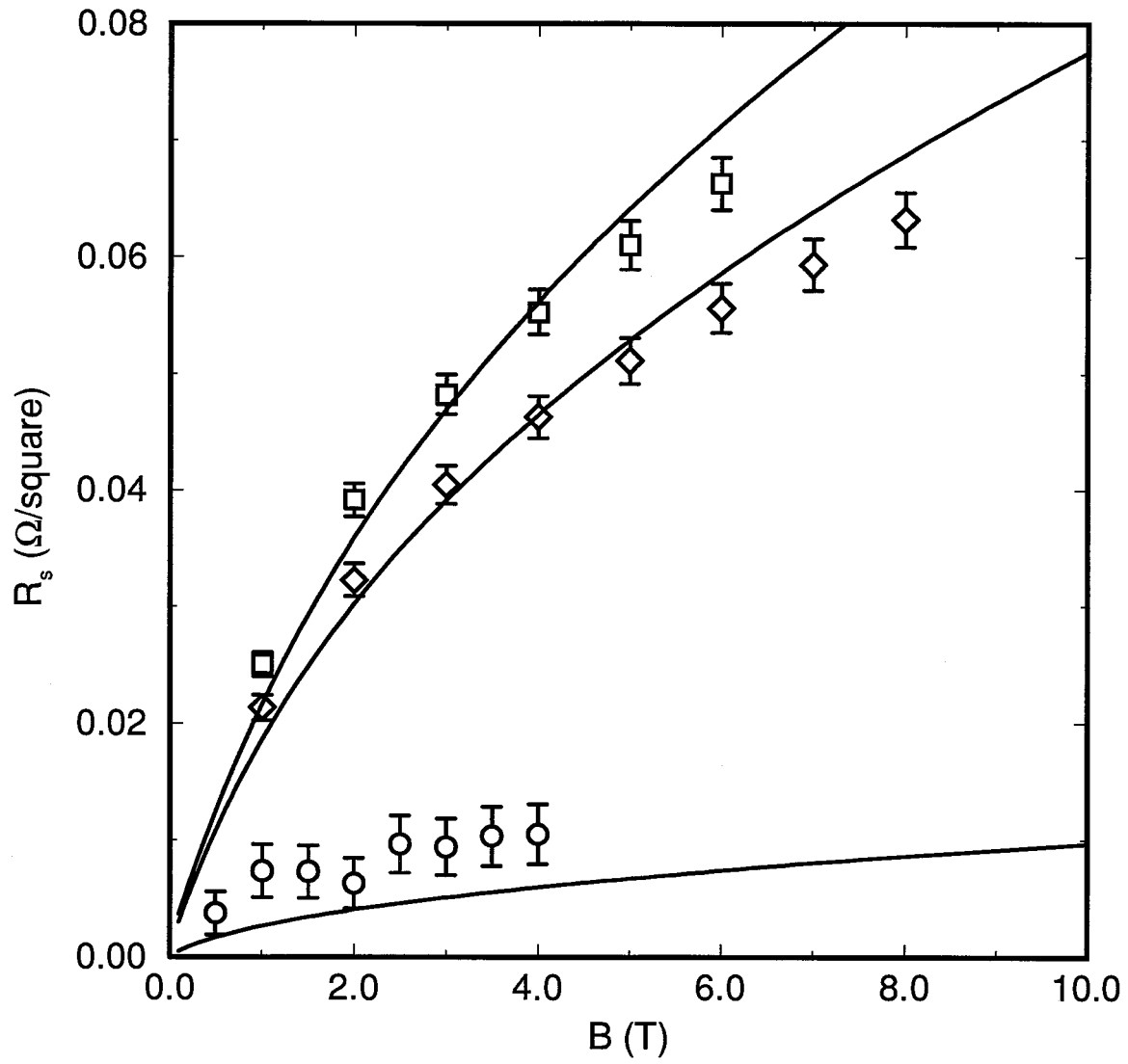Figure 6.24: Fitting as a function of frequency and field at 78K. ◯: 5.4 GHz; ◇: 27 GHz; □: 35 GHz. Both η and ω_p are field independent.
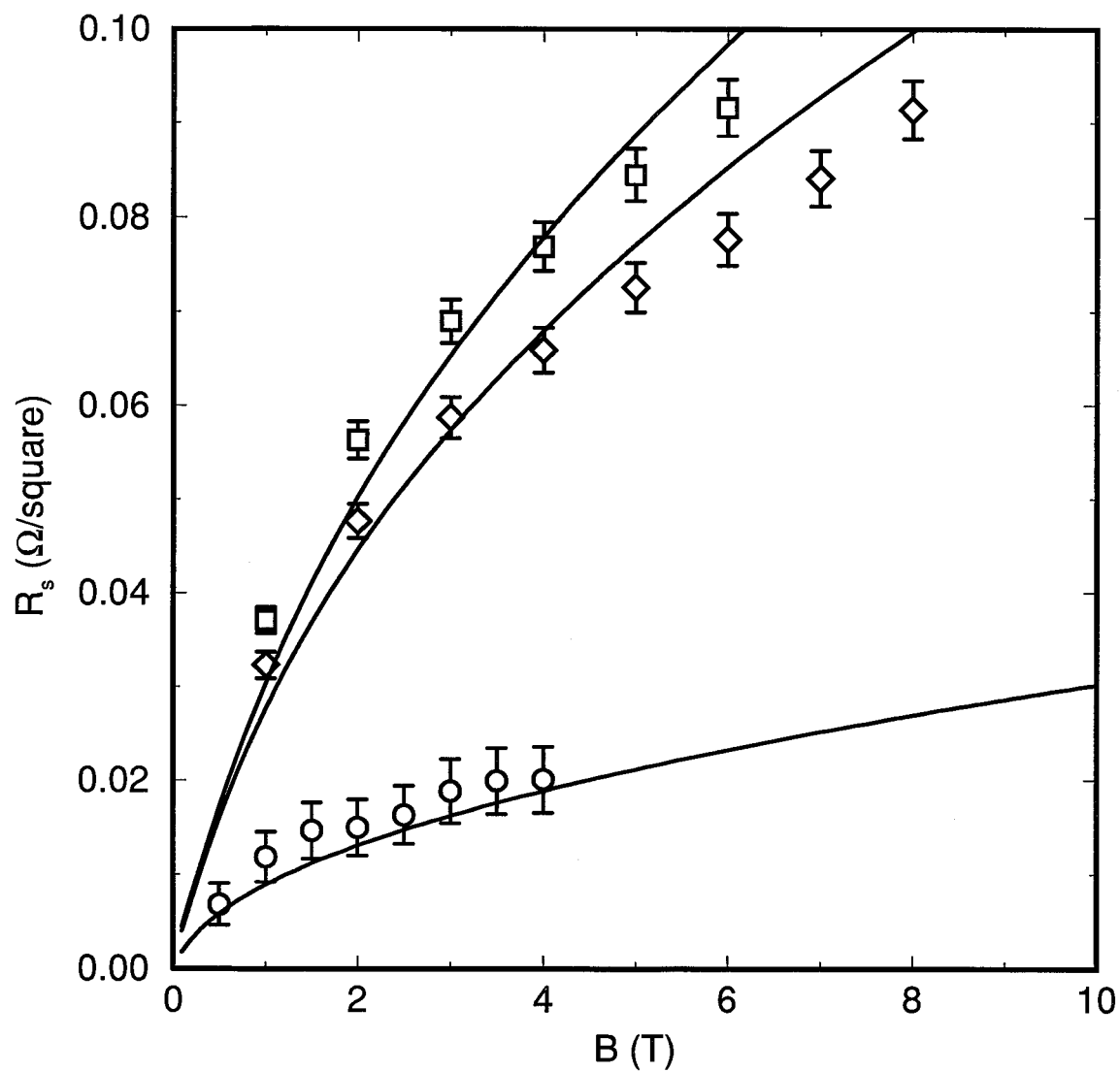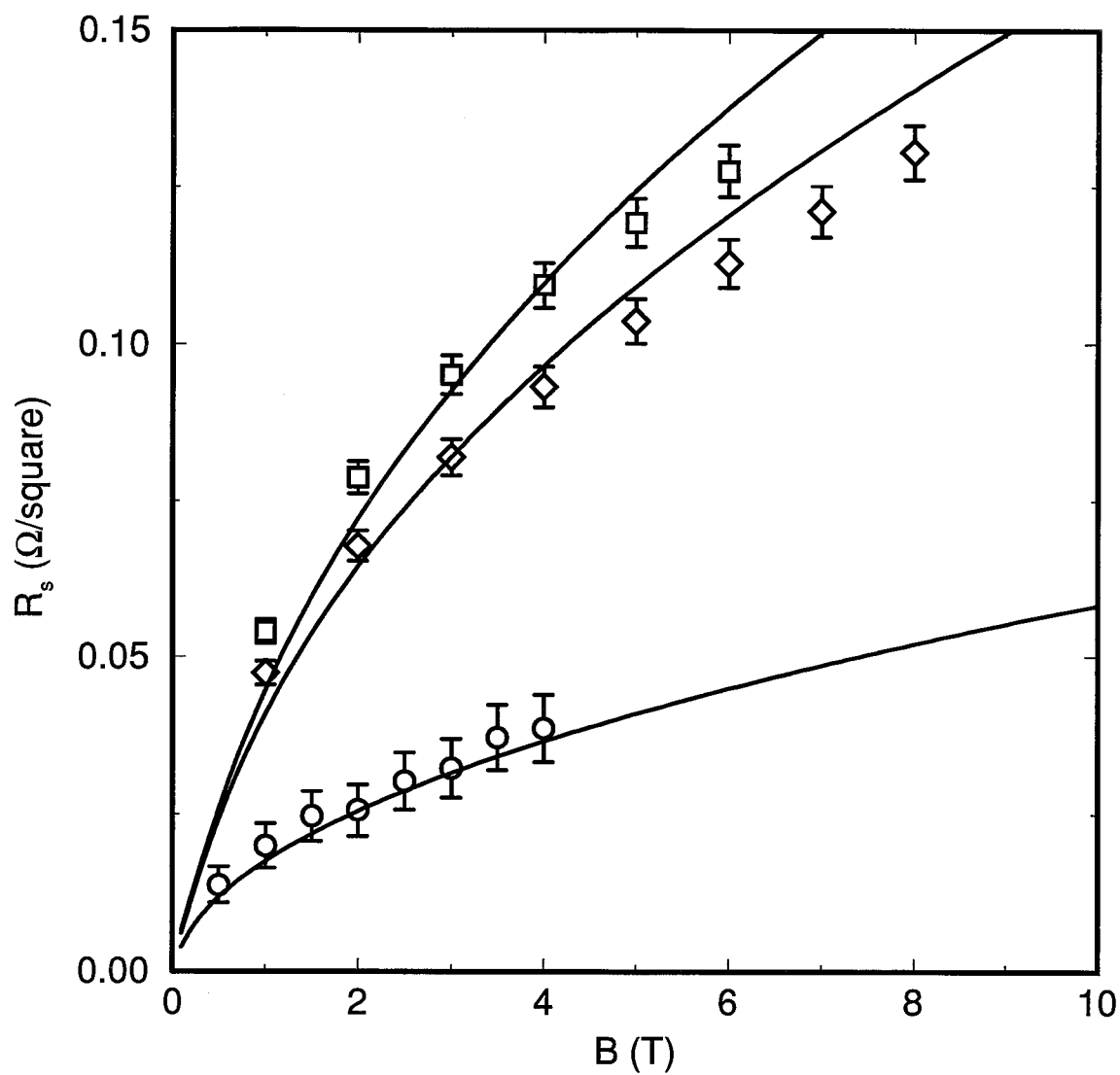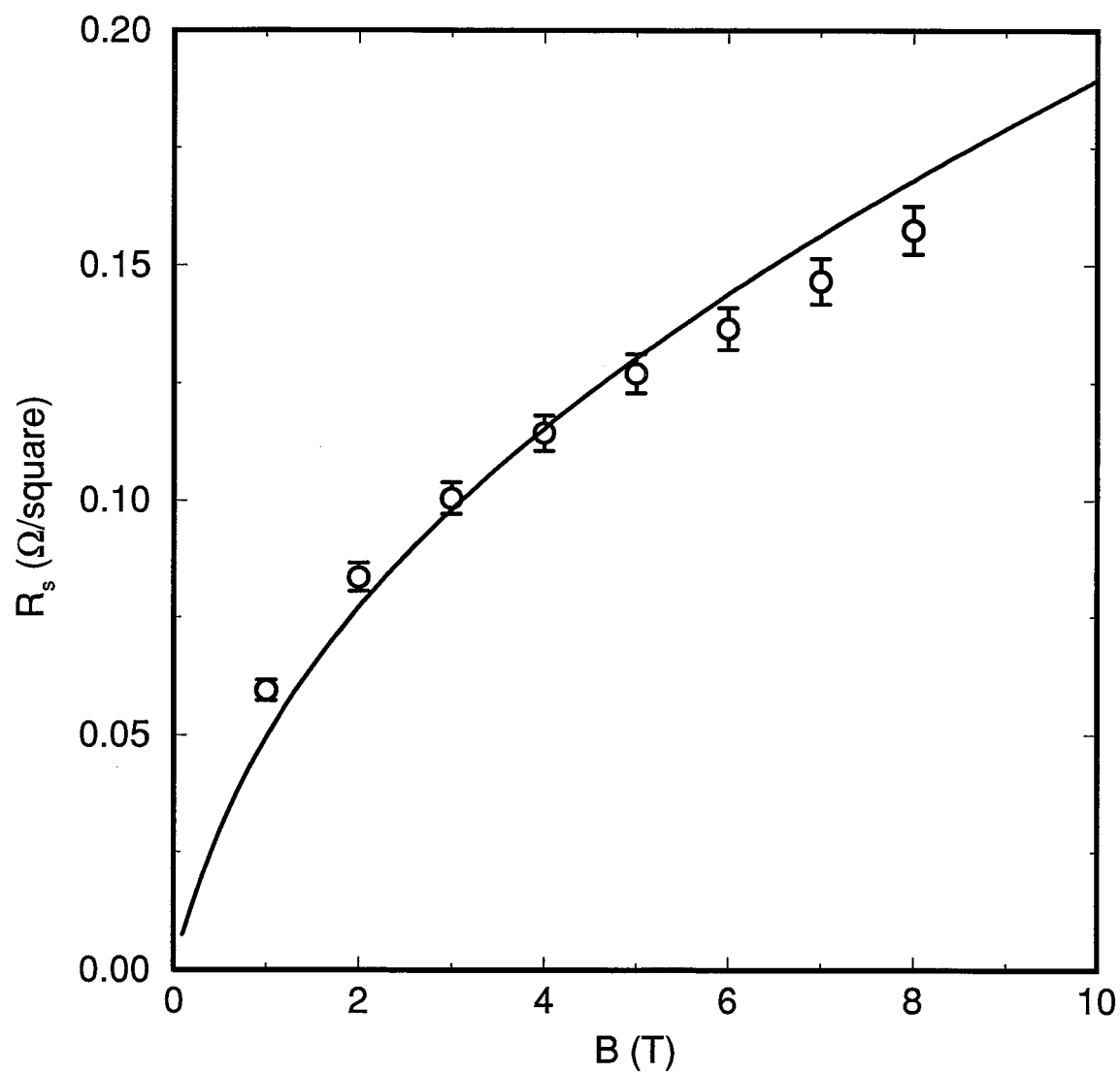
Figure 6.25: Fitting as a function of field at 82K and 27 GHz. η is field independent, and ω_p has been set to zero

point to distinguish between two separate issues: first, the poor overall fit to the 5.4 GHz data at intermediate temperatures; second, the poor fit to the field dependence of, in particular, the high frequency data. The first point is most probably due to limitations of the single pinning frequency model. At low temperatures, the pinning frequency is large compared to 5.4 GHz and at high temperatures it starts to be small compared to 5.4 GHz. At these temperatures, therefore, we are less sensitive to the shape of the crossover from the flux-pinned to the flux-flow regime. At the intermediate temperatures where the pinning frequency is comparable to 5.4 GHz is where we are most sensitive to the exact shape of the crossover: it will be relatively sharp for a single pinning frequency model but broadened out if there is a distribution of pinning frequencies. The second point is more difficult and one about which we will be able to come to no definite conclusion. It is unclear whether or not the shape of the field dependence and its systematic deviation from the fitted curve is due to genuine field dependence of η or perhaps ω_p (certainly, ω_p cannot alone be responsible because the anomalous field dependence persists even after ω_p has become very small) or our lack of knowledge about the true field dependence of the London penetration depth. Comparing the 78 K field profiles of the 35, 27 and 5.4 GHz data, figure 6.24, suggests the possibility of an answer. The field dependence of the 5.4 GHz profile is not inconsistent with the fit whereas the 27 and 35 GHz curves clearly deviate systematically from the fitted curves. Since we expect η and ω_p to be frequency independent, we might therefore conclude that field dependence of these parameters is not responsible for the systematic deviations at the higher frequencies. The *effect* of the λ_L^2 term on the other hand is quite frequency dependent; as we have already seen, at low frequencies its importance is diminished because of the ω in the denominator of the flux-flow skin depth. However, the large error bars on the 5.4 GHz data preclude any definite conclusions based on the shape of this curve. It is also quite possible that field dependence of the vortex viscosity due to interactions or a non-zero Hall effect could be

responsible. It is interesting to note that a good fit to the data at, for example, 70 K can be obtained by setting $\lambda_L(0)$ to effectively zero as in figure 6.26. In other words, the field profiles are almost purely square-root like at this temperature. However, figure 6.27 shows the same procedure tried at 20 K only here the fit is poor. Evidently, at least at low temperature, the presence of the λ_L^2 term is reflected in the data.

Figure 6.28 compares the temperature dependence of ρ_{ff} at 4T obtained by the field dependent and field independent fitting procedures. The curves are qualitatively similar, the largest discrepancies occurring at intermediate temperatures (see inset) — an effect anticipated by our previous discussion. It is clear that on the scale of the changes observed as a function of temperature, the field dependence is a minor effect. When we discuss the temperature dependent scaling of the data in the next section, we will use the ρ_{ff} curves obtained in section 6.2.2 and shown in figure 6.17. This is more appropriate for an overall discussion of the data because close to T_c and H_{c_2} we have already seen that the field dependence of the surface resistance is affected by fluctuations.

6.3 Scaling the Data

In order to try and uncover the mechanism that gives rise to the data set, the obvious starting point is to try scaling the data by ρ_n and H_{c_2} as was done in the experiments on conventional superconducting alloys. We face two immediate problems. First, in scaling with H_{c_2} , do we use the temperature dependent $H_{c_2}(T)$ or its zero temperature value $H_{c_2}(0)$. Second, what should we use for ρ_n ? This is perhaps the most fundamental question that we will address in this thesis because this is equivalent to asking about the scattering time for the electrons in and possibly around the cores. In other words, we are trying to deduce information about the nature of dissipation in the moving vortex cores. With the possibility of discrete, widely spaced electronic levels in the cores, is
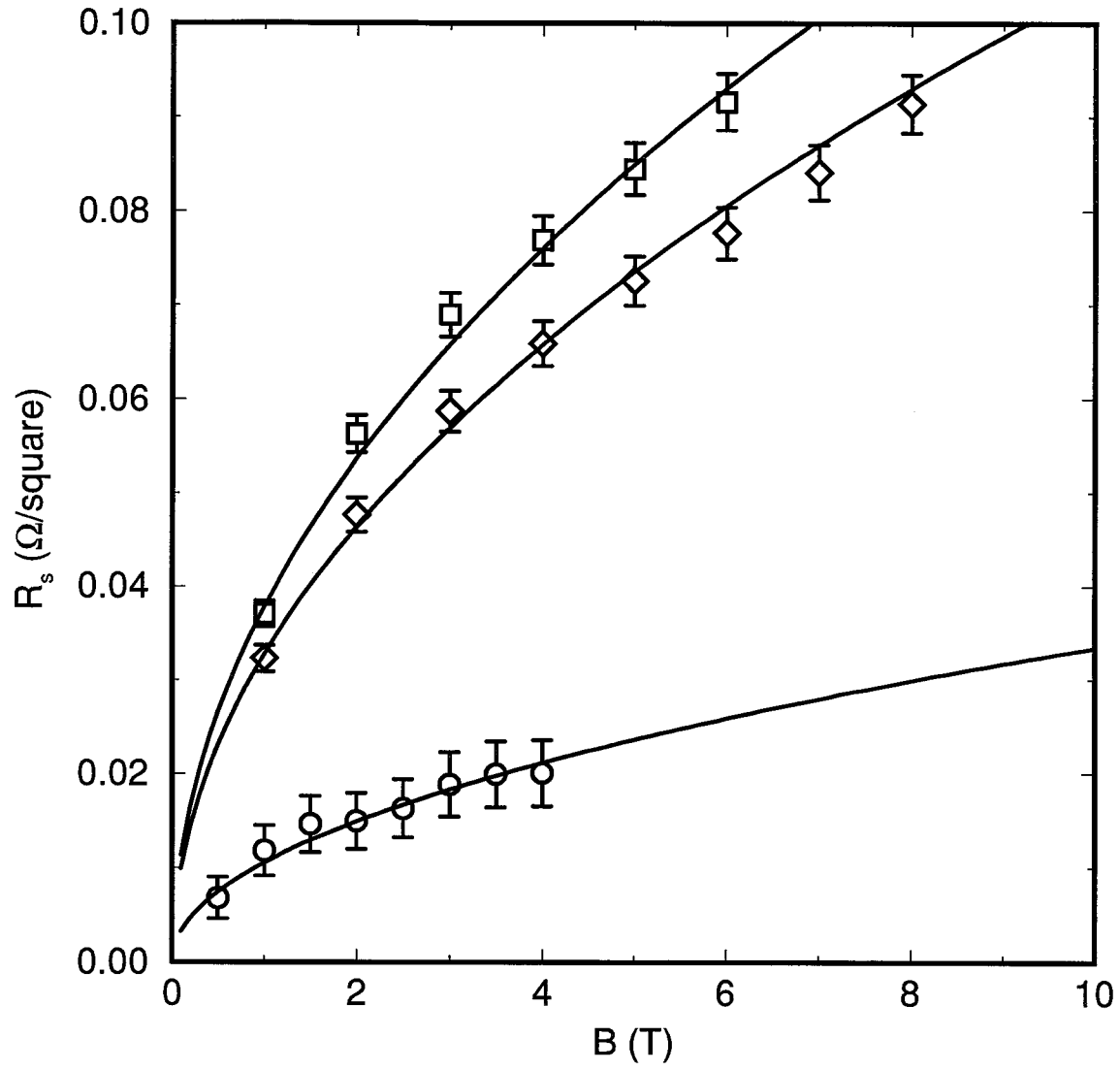
Figure 6.26: Fitting as a function of frequency and field at 70K, $\lambda_L(0) \sim 0$. $\bigcirc$: 5.4 GHz; $\diamondsuit$: 27 GHz; $\square$: 35 GHz. Both η and ω_p are field independent.
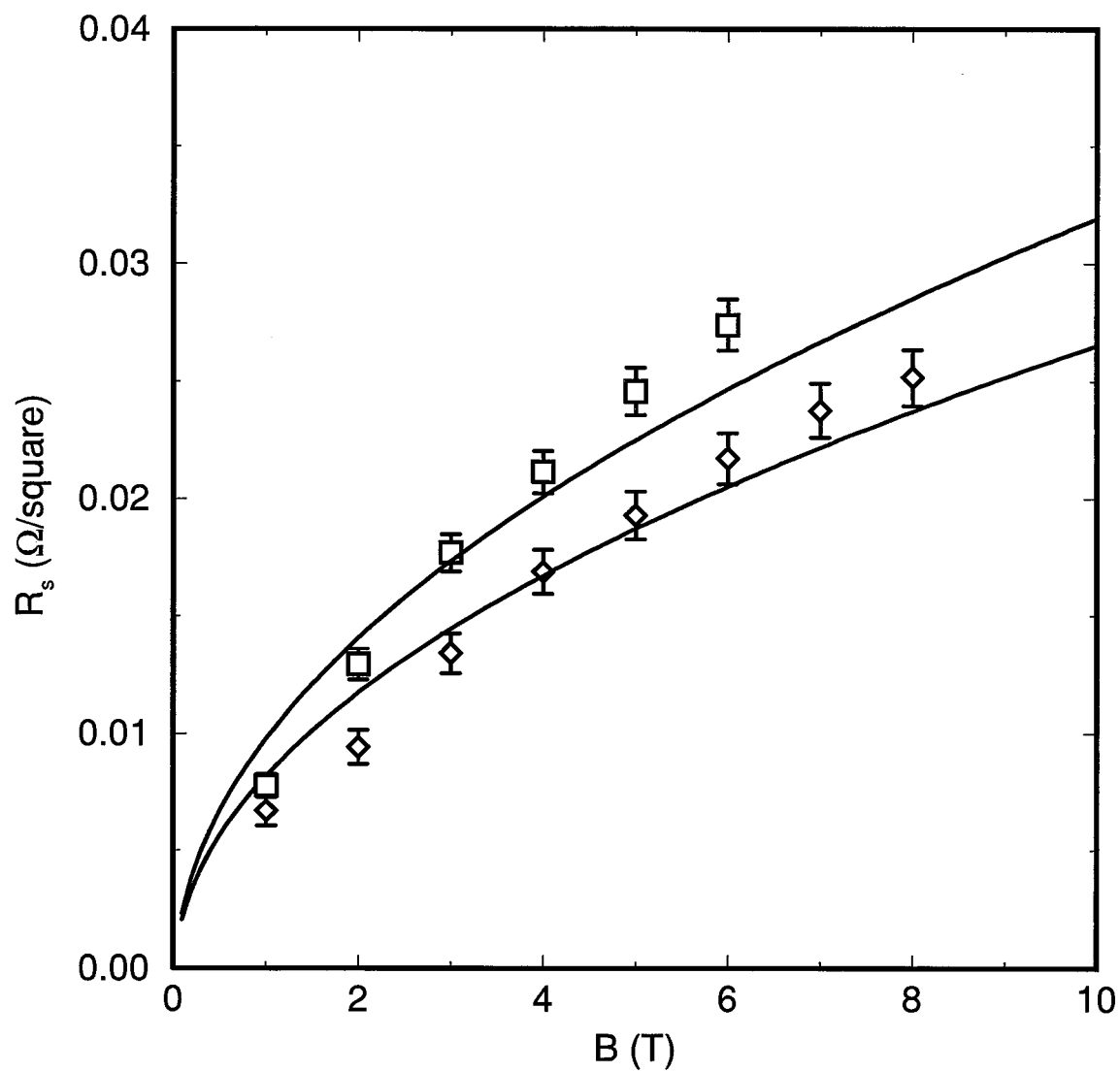
Figure 6.27: Fitting as a function of frequency and field at 20K, $\lambda_L(0) \sim 0$. $\Diamond$: 27 GHz; $\Box$: 35 GHz. Both η and ω_p are field independent.
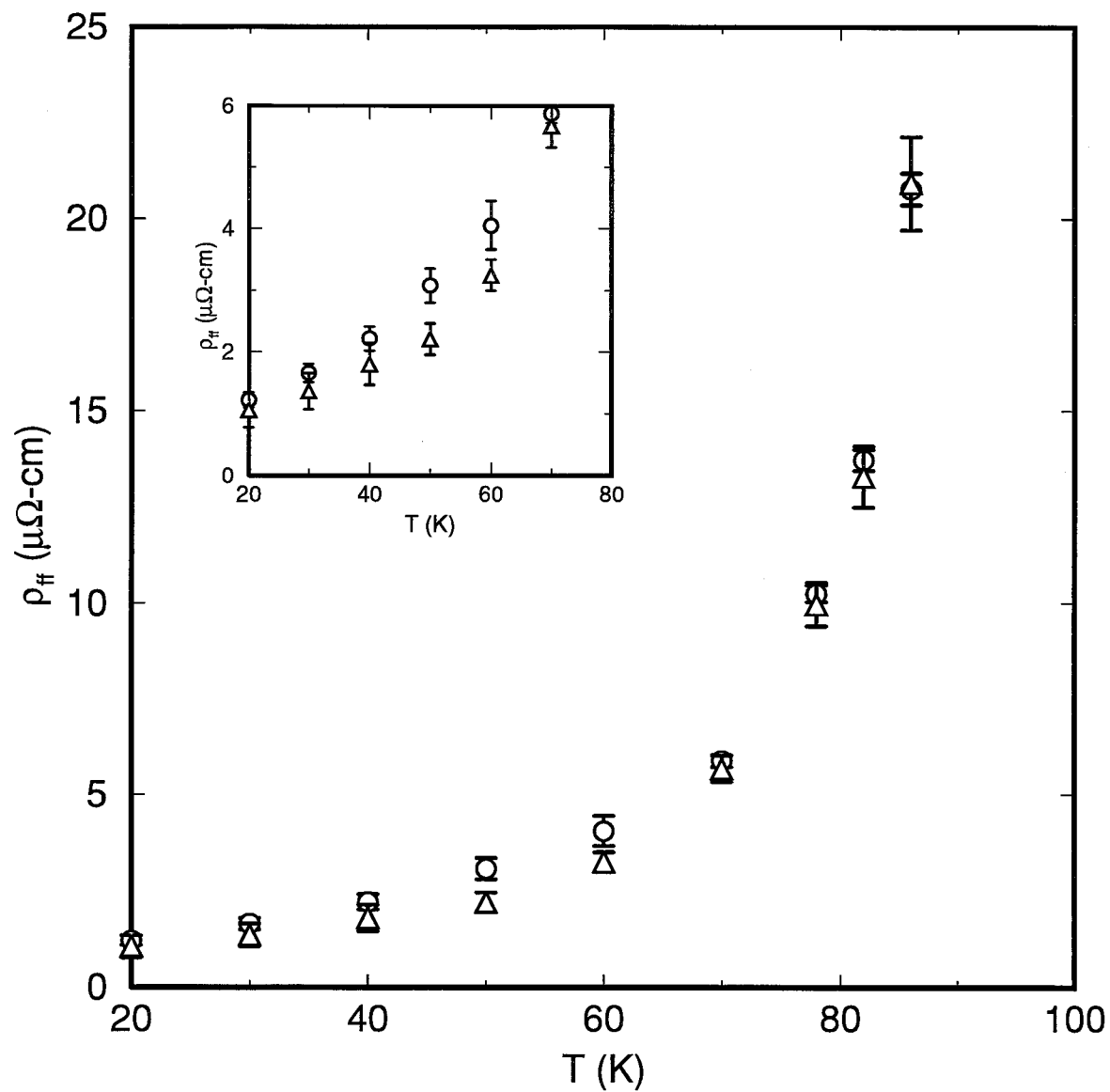
Figure 6.28: Comparison of different fitting procedures. The circles were generated by the field dependent fits and the triangles by field independent fits. Inset: a close-up of intermediate temperatures where there is a slight discrepancy.

it even appropriate to think of a core as a normal material with an effective normal resistivity ? How would the picture change if the gap has d-wave symmetry and is thus effectively gapless ? In conventional superconducting alloys, the ρ_n used was the temperature independent impurity limited value. For $YBa_2Cu_3O_{6.95}$, the normal state resistivity above T_c is not constant but linearly decreasing until fluctuations set in about 20-30K above T_c . As a first attempt at a guess for ρ_n, we will use an extrapolation of the linear portion of ρ_n from above T_c :

$$\rho_n(T) = 0.869\,T + 0.85\mu\Omega-cm \ . \tag{6.2}$$

This was obtained from dc resistivity data[17] and is consistent with the dc resistivity value used to calibrate the surface resistance ($\rho_{dc}(100K) = 77.8\mu\Omega$–cm). The vortex core is thus being treated like a region of normal material: its resistivity is determined by the normal state properties with a linear scaling factor to take into account the temperature variation. We would not expect the core resistivity to be affected by the fluctuation contribution to the resistivity because over most of the temperature range of interest, it is well away from T_c (except possibly when H gets close to H_{c_2}). Scaling ρ_{ff} by just this linear ρ_n and a temperature independent $H_{c_2}(0)$ gives the set of curves shown in figure 6.29. Comparing with figure 3.3 from Kim et al[1] shows that we are seeing qualitatively different behaviour i.e. a law of corresponding states as given by equation 3.53 does not fit the data.

If we use the $H_{c_2}(T)$ function given in Chapter 2 (equation 2.2) to scale the magnetic field we get the result shown in figure 6.30. It is clear that this scaling of the flux flow resistivity and the magnetic field does a reasonable job of bringing all the field curves together onto a universal curve suggesting the relation

$$\frac{\rho_{ff}}{\rho_n(T)} = \frac{H}{H_{c_2}(T)} \tag{6.3}$$
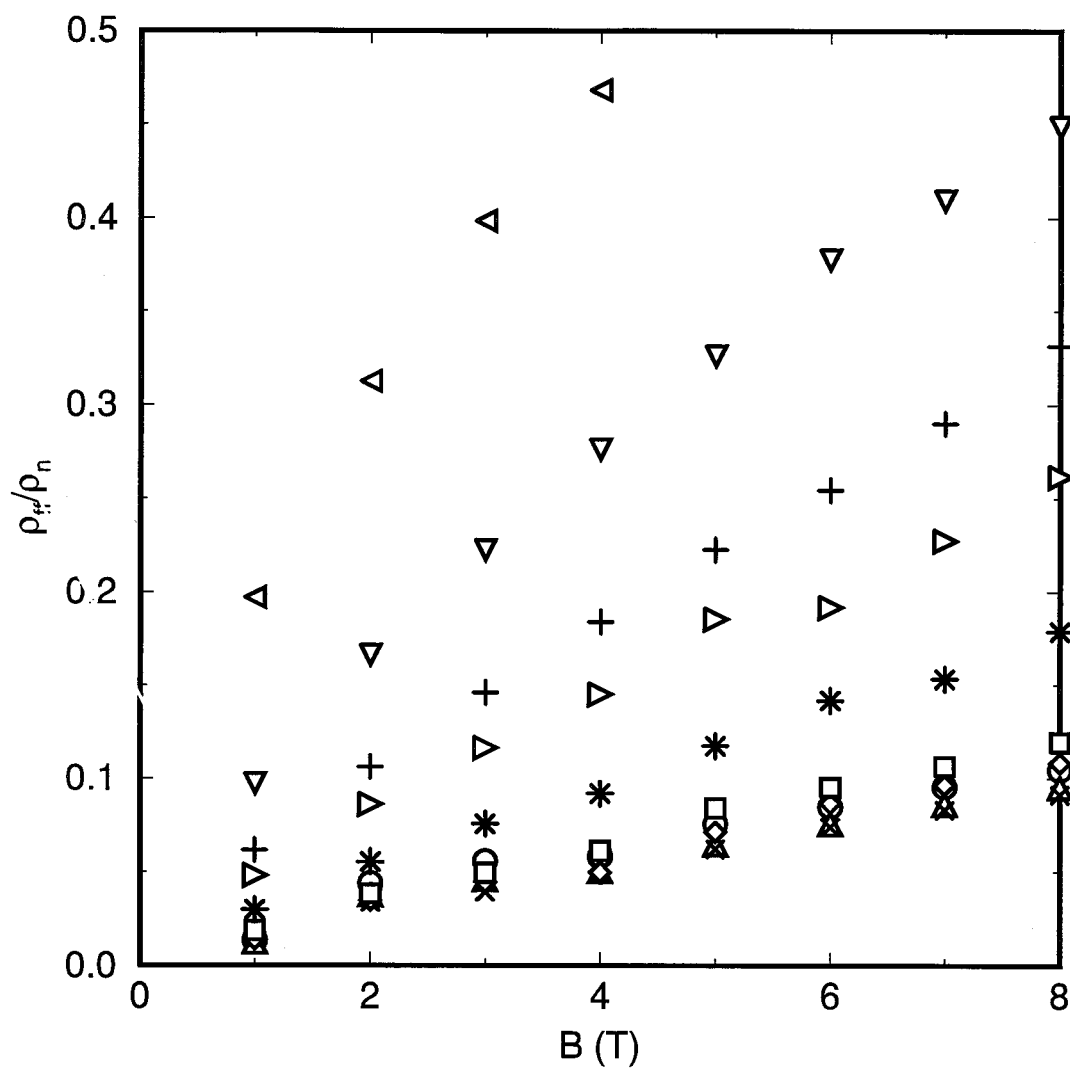
Figure 6.29: Field dependence of $\rho_{ff}/\rho_n(T)$. $\bigcirc$: 20K; $\triangle$: 30K; $\times$: 40K; $\diamondsuit$: 50K; $\square$: 60K; $*$: 70K; $\triangleright$: 78K; $+$: $82K$; $\triangledown$: 86K; $\triangleleft$: 90K. $\rho_n(T)$ is given by a linear extrapolation of the normal state resistivity from above T_c : $\rho_n(T) = 0.869T + 0.85\mu\Omega$-cm.
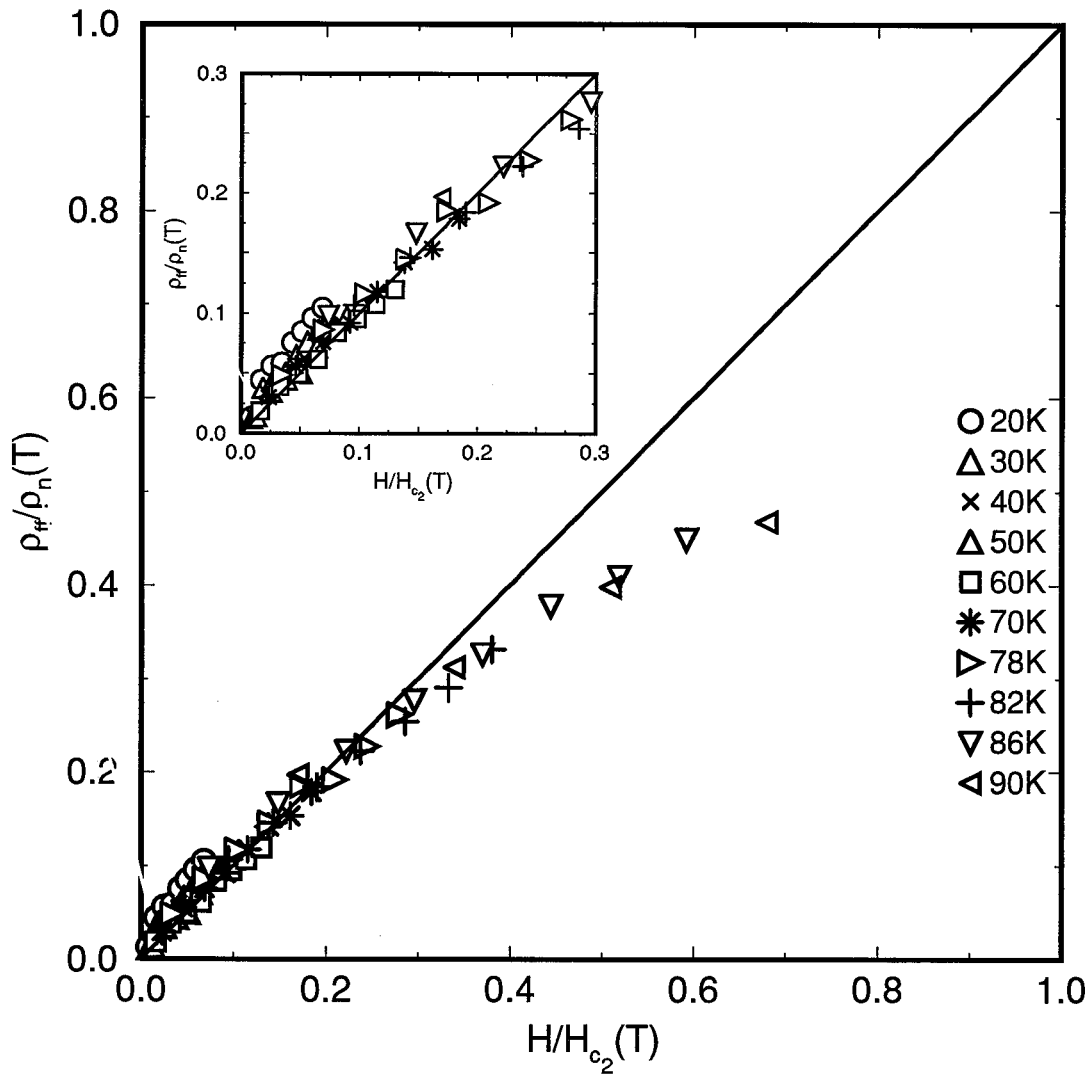
Figure 6.30: $\rho_{ff}/\rho_n(T)$ as a function of the reduced field H/H_{c_2}. $\rho_n(T)$ is again given by the linear extrapolation of the normal state resistivity from above T_c as in figure 6.29 and $H_{c_2}(t)$ is given by the empirical expression of Chapter 2.

This would favour a picture in which the amount of dissipation is proportional to the volume fraction of normal material. It is also more in line with the behaviour observed by Fogel[3] in his experiments on PbIn. Again we see that for H close to H_{c_2}, ρ_{ff} begins to curve over as it become contaminated by the fluctuation effects that affect the surface resistance close to T_c and H_{c_2} (see the discussion in section 6.1).

We can get a better appreciation for how well this empirical expression is describing the data by assuming that it holds and using the ρ_{ff} data and say a linear ρ_n to predict $H_{c_2}(T)$. Alternatively, we can assume an equation for $H_{c_2}(T)$ and predict $\rho_n(T)$. The results are shown in figure 6.31 and figure 6.32. The picture seems to hold down to about 50K, but, below that, significant deviations occur. The flux-flow resistivity is not decreasing fast enough at low temperatures to maintain consistency with equation 6.3.

One possibility that might account for the above discrepancy is that our formula for $H_{c_2}(T)$ is using an inflated value for $H_{c_2}(0)$. Indeed, there is some experimental support for this possibility. Two different Japanese groups[73, 74], using pulsed magnetic fields, have reported values of about 40T for $H_{c_2}(0)$ (field parallel to the c-axis) in $YBa_2Cu_3O_{7-\delta}$ single crystals. The reason for the discrepancy between this value and the one estimated from theory is not well understood. In any event, such a value for $H_{c_2}(0)$ would mean that ρ_{ff} is below what we would expect from this formula.

It is also possible that the low temperature behaviour in figure 6.31 has something to do with Pauli spin paramagnetic limiting of H_{c_2} as discussed in section 3.5 in connection with the flux flow resistivity measurements of Kim et al[1] on high field superconducting alloys such as Ti-V. For conventional type-II superconducting alloys in the dirty limit, Werthamer et al[32] calculated how Pauli spin paramagnetism competed with another effect — spin-orbit impurity scattering[1] — in its effect on H_{c_2}. They found that

---

[1]Spin-orbit scattering refers to a process whereby an electron (due its spin-orbit interaction) can scatter off an impurity in the superconductor with a flip of its spin.
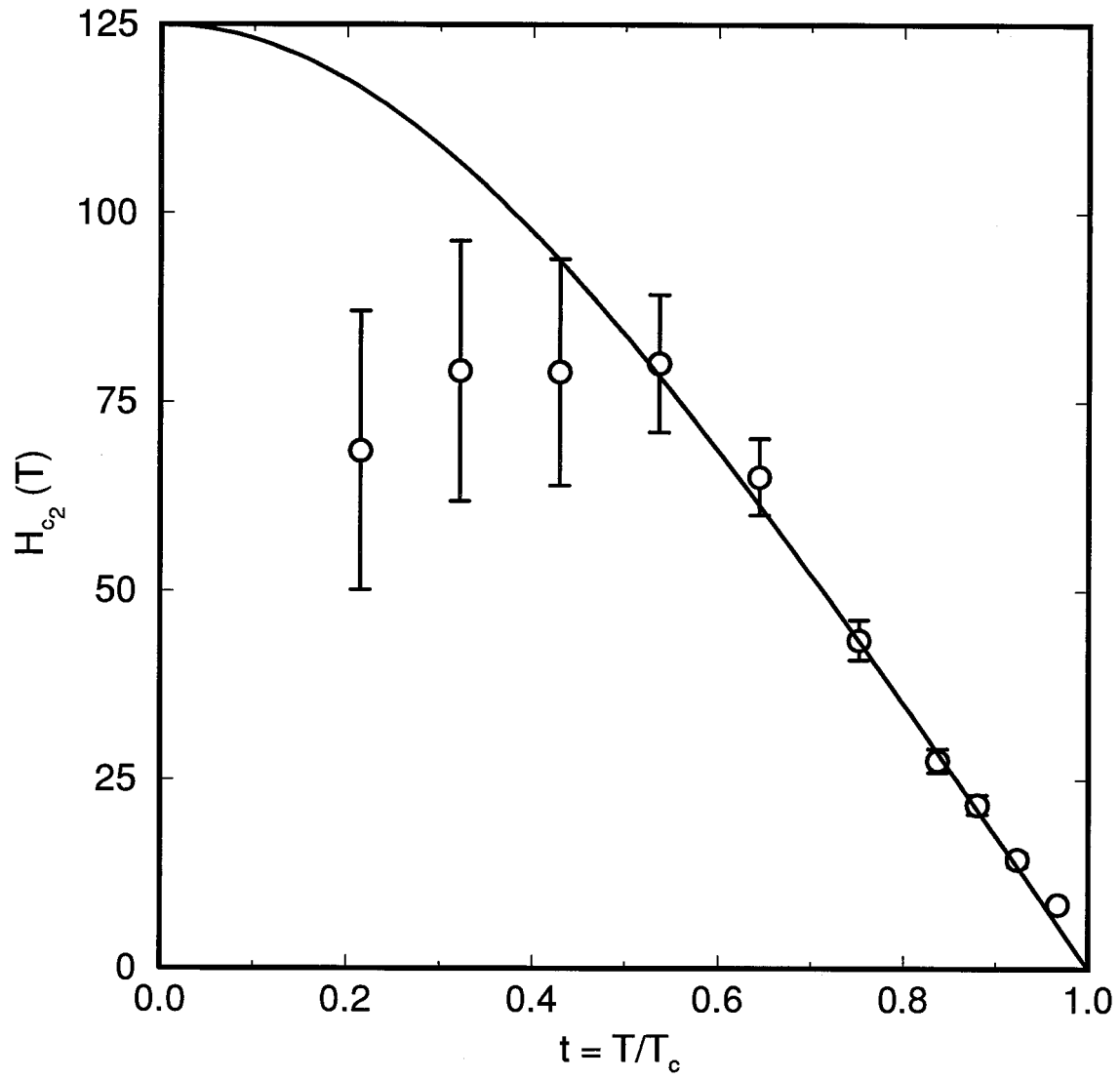
Figure 6.31: Predicted H_{c_2} using ρ_{ff} data. Equation 6.3 was used along with the expression for $\rho_n(T)$ used in figures 6.29 and 6.30 to calculate H_{c_2} from ρ_{ff}.
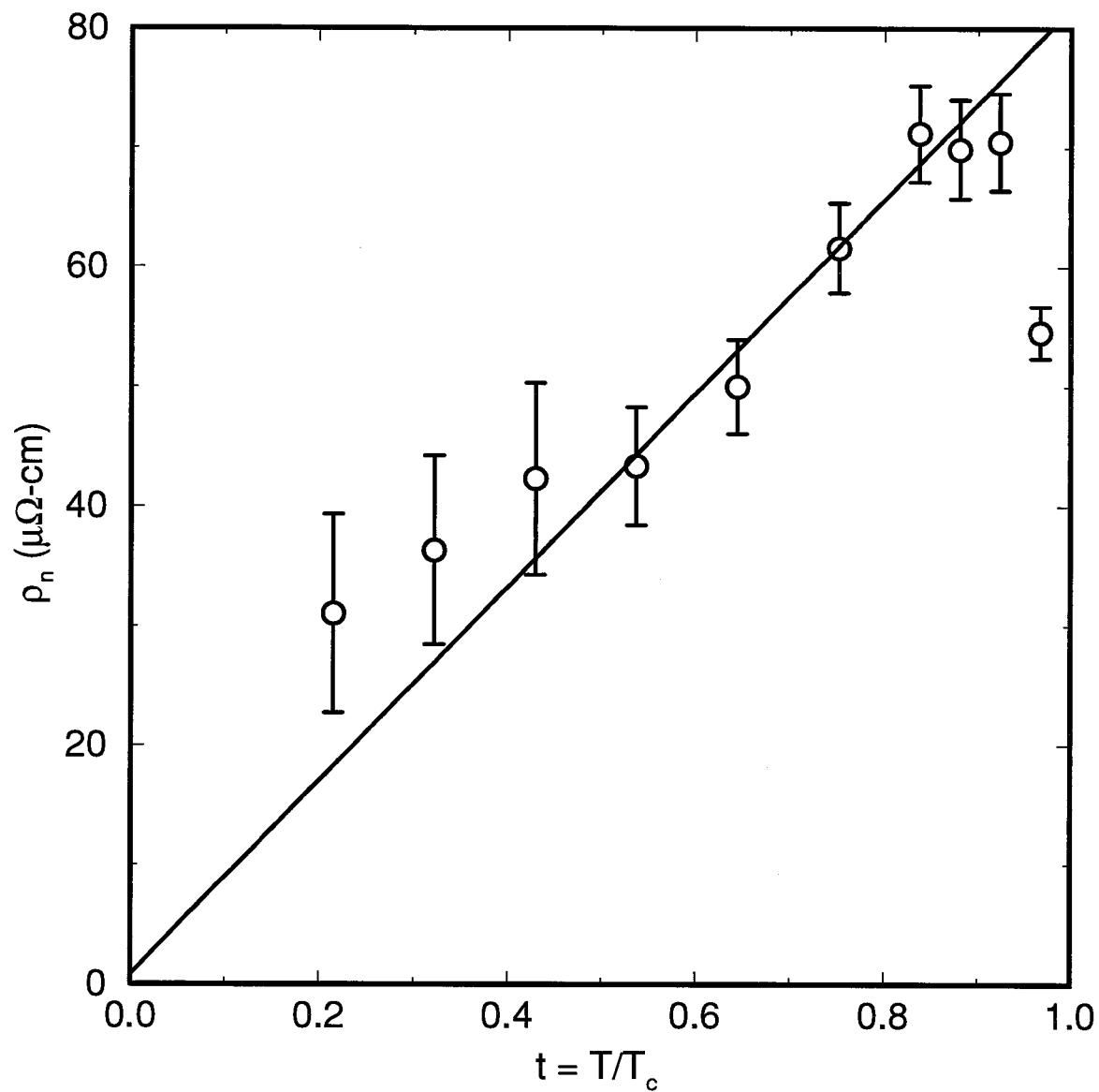
Figure 6.32: Predicted $\rho_n(T)$ using ρ_{ff} data. Equation 6.3 was used along with the expression for H_{c_2} used in figure 6.30 to calculate $\rho_n(T)$ from ρ_{ff}.

spin-orbit scattering renders the spin paramagnetism less effective in reducing H_{c_2} . In YBa$_2$Cu$_3$O$_{6.95}$, which is in the clean limit, this scattering mechanism is presumably less important than in dirty, conventional type-II superconductors, and thus we might expect Pauli spin paramagnetism to be an important factor in limiting H_{c_2} at low temperatures in this material. However, it is difficult to quantify this because the standard calculations for the reduction of H_{c_2} due to paramagnetic limiting are for BCS s-wave superconductors in the dirty limit rather than the clean limit. Another important consideration is that, as we saw in section 3.5, Kim et al[1] found that the flux-flow resistivity at low fields and temperatures was related not to the paramagnetically limited H_{c_2} but rather to the expected value ignoring paramagnetic effects — the volume fraction of normal material being the physically relevant quantity. If we adopt a similar position with regards the flux flow resistivity in YBa$_2$Cu$_3$O$_{6.95}$, then we would not expect a value of H_{c_2} based on ρ_{ff} to contain information about paramgnetic limiting.

Chapter 7

Discussion and Conclusions

Based on the temperature dependence of the flux flow resistivity and a reasonable esti-
mate for $H_{c_2}(T)$, we conclude that the temperature dependence of the scattering rate of
the charge carriers in the vortex cores below T_c is qualitatively similar to a continuation
of the linearly decreasing normal state resistivity from above T_c . This is suggestive
that the the picture of a vortex as having a 'normal' core has some applicability for
$YBa_2Cu_3O_{6.95}$.

Using the Bardeen-Stephen formula[9] at 20K with $H_{c_2}(20K) \sim 120T$ and the flux
flow resistivity determined from the microwave surface resistance, we obtain a value of
$\rho_n(20K) \sim 30\mu\Omega$–cm — a decrease of a factor of $\sim$2–3 from its value in the normal
state above T_c . This is in sharp contrast to the rapid decrease in the scattering rate of
the quasiparticles in the normal fluid of the bulk superconductor away from the vortices.
The surface resistance data in zero field measured on similar $YBa_2Cu_3O_{6.95}$ single crystals
by Bonn et al[18, 19] indicate a drop in this normal quasiparticle scattering rate by a
factor of $\sim$50–100 between T_c and 20K. That there is qualitative similarity between the
temperature dependence of this scattering rate and that of the flux flow resistivity is
probably misleading. It seems more likely that the rapid drop in ρ_{ff} is associated with
the steeply rising H_{c_2} with decreasing temperature below T_c . In fact, we have found
that, for $T > 50K$, the flux-flow resistivity is in reasonable agreement with the equation

$$\frac{\rho_{ff}}{\rho_n(T)} = \frac{H}{H_{c_2}(T)} \qquad (7.1)$$

136

where we use an extrapolation of the linear dc resistivity from above T_c given by

$$\rho_n(T) = 0.869\,T + 0.85\mu\Omega-cm \qquad (7.2)$$

and a temperature dependence for H_{c_2} given by

$$\mu_0 H_{c_2}(T) = 125\frac{(1-t^2)}{(1+t^2)^{1/2}}\,. \qquad (7.3)$$

This is in qualitative agreement with Kunchur et al[25] in their high current dc measurements of $YBa_2Cu_3O_{7-\delta}$ epitaxial films, although in our measurements the surface resistance (and thus the determination of ρ_{ff}) is affected by fluctuations close to T_c and H_{c_2} . To the extent that ρ_{ff} seems to scale with the inverse of the *temperature dependent* H_{c_2} , our results are also similar to Fogel's[3] ρ_{ff} obtained from measurements of the dc resistivity of a PbIn alloy. However, our results differ markedly from those of Kim et al[1] and others[2] who find that ρ_{ff} can be described by

$$\frac{\rho_{ff}}{\rho_n} = \frac{H}{H_{c_2}(0)}\,. \qquad (7.4)$$

If we try to adopt equation 7.4 to describe our data by incorporating all of the temperature dependence of ρ_{ff} into a rapidly temperature dependent ρ_n, this leads to absurdly large values of $\rho_n(T)$ ($\gg \rho_n(T_c)$) at higher temperatures. Therefore, the picture of the vortex dynamics, at least for $T > 50K$, seems to be a conventional one: the cores are regions of normal material with a scattering rate for the charge carriers given by a simple linear extrapolation of the normal state material from above T_c ; the resistivity of the material is given by approximately the volume fraction of the material in this 'normal state' ($H/H_{c_2}(T)$) multiplied by the resistivity of the normal material. However, it should be appreciated that this is at best an incomplete picture. In the Bardeen-Stephen model[9], the transition region outside the normal core contributes as much to the dissipation as the normal core itself. In conventional superconducting alloys, the scattering rate is

characterized in both regions by the same $1/\tau$ (because the scattering is in the impurity limit). For $YBa_2Cu_3O_{6.95}$, we might expect different scattering rates for the two regions because in the transition region it is possible that the normal fluid quasiparticle scattering rate is a factor. It is not obvious therefore that a simple Bardeen-Stephen like model of vortex motion should make sense in such a situation.

Below 50K, ρ_{ff} is larger than what we would expect on the basis of equation 7.1 and our estimates of $\rho_n(T)$ (equation 7.2) and $H_{c_2}(T)$ (equation 7.3). Although a large Hall angle can affect the flux flow resistivity,

$$\rho_{ff} = \frac{\Phi_0 \, B}{\eta} \ \rightarrow \ \frac{\Phi_0 \, B}{\eta \, (1 + \alpha^2/\eta^2)} \tag{7.5}$$

(see equation 3.17), the result would be to decrease, not increase ρ_{ff} . The possibility that a value of 125T is in fact an overestimate of $H_{c_2}(0)$ has been discussed. Given this uncertainty in $H_{c_2}(0)$ it is possible that the validity of equation 7.1 can be extended to low temperatures.

It is worth reiterating at this point that, at low temperatures, the data analysis is most sensitive to the limitations of a single pinning frequency model. The pinning frequencies obtained from the fits, while consistent with estimates [75] for high-T_c superconductors and with the data of Owliaei et al[62] (see figure 3.8— their surface resistance at 10 GHz is greatly suppressed by 70K indicating a pinning frequency greater than 10 GHz at lower temperatures), should not be taken too seriously. At lower temperatures, when the pinning frequency is a substantial fraction of 27 or 35 GHz, we are most sensitive to errors in ρ_{ff} caused by the possible inability of the model to properly fit the shape of the crossover from the flux pinned to the flux flow state. We can certainly conclude (as above) that the ρ_{ff} data at low temperature is inconsistent with a rapidly decreasing scattering rate. However, given the limitations of the model used to fit the data, the uncertainty in $H_{c_2}(0)$ and the uncertainty in the exact form for $\rho_n(T)$, it is probably

unwise to make any other definitive statements about the low temperature behaviour of ρ_{ff} .

We are able to get good fits in terms of a field *independent* η and ω_p at 20 and 30K. At these temperatures, we are fitting the data at all frequency and field in terms of just two parameters. This reinforces our faith in the applicability of the Coffey-Clem solution[28, 29] to our data. A field independent η corresponds to a linear dependence of ρ_{ff} on the magnetic field and this is what we might expect at low temperature and field. The functional dependence of the R_s field profiles deviate from a simple square-root like behaviour because of the presence of the screening term, λ_L^2, in the expression for the surface impedance. The effect of this term is made quite apparent by plotting R_s^2 versus B: at low fields, there is non-linear behaviour which gradually gives way to a linear dependence at higher fields where the flux flow contribution dominates. At higher temperatures, it is difficult to fit in terms of a field independent η. Its field dependence is strongest at low fields where the effect of the λ_L^2 term is most important. This suggests the possibility that our lack of knowledge of the field dependence of λ_L is affecting the fitted value of η. Other sources for the field dependence of η could be interactions with other vortices or possibly Hall effects. While it is not possible to resolve these issues at present, we should remember that these are relatively minor effects compared to the scale of the temperature dependence of η or ρ_{ff} . Our conclusions based on this temperature dependence are unaffected by the above discussion.

It is unclear what bearing the large spacing between the energy levels of the quasi-particle states in the core of the vortex have on our results. The main effects of the discrete nature of the energy spectrum happen, according to Hsu[22, 23], at a frequency corresponding to the level spacing, Δ^2/E_F, which is ~ 200–300 GHz for high-T_c super-conductors. It is possible that we are in some sense in the low frequency limit of his theory in which, in the clean limit, he recovers an expression like that of Bardeen and

Stephen[9].

At present, it is unknown what effect the existence of a d-wave instead of an s-wave ground state might have on the picture of moving vortices. We have seen that, with some reasonable assumptions, the flux flow resistivity, at least in a qualitative sense, can be understood in $YBa_2Cu_3O_{6.95}$ within the same framework used for conventional s-wave superconductors. A better understanding of the vortex core energy level spectrum within the context of d-wave superconductivity is needed before the possible relevance of either to the flux flow resistivity can be ascertained.

In summary, then, the central conclusions of this work are as follows:

- The Bardeen-Stephen like expression, equation 7.1, is in reasonable agreement with the data down to at least 50K using a linear extrapolation of the normal state resistivity from above T_c for $\rho_n(T)$ and an estimate of $H_{c_2}(T)$ based on magnetization measurements and theoretical estimates from the literature.

- The rapidly temperature dependent normal fluid quasiparticle scattering rate observed in zero field microwave measurements on the same crystal is not the relevant scattering rate for charge carriers in the vortex core.

- The fact that a linear extrapolation of the normal state resistivity from above T_c is consistent with the data in our analysis is perhaps suggestive that the idea of a 'normal' vortex core is valid for $YBa_2Cu_3O_{6.95}$.

Of great interest would be to extend these measurements to even higher frequencies. This would push the flux dynamics further into the high frequency, flux flow limit and make the analysis less sensitive to any uncertainty incurred by fitting to the fairly crude, single pinning frequency model. A study of the sensitivity of the pinning frequency to the density of twin boundaries would also be useful. It is possible that by measuring

nearly twin-free crystals, experiments performed at the existing frequencies could better probe the high frequency limit.

Appendix A

The Surface Impedance of Metals and Superconductors

We consider a material subject to a time dependent magnetic field at its surface. The material occupies the half space $x > 0$ and we apply the field in the z-direction along its surface

$$\mathbf{H} = H_0 \, e^{i\omega t} \, \hat{\mathbf{z}}. \qquad (A.1)$$

The material has conductivity $\tilde{\sigma}$ which is in general complex.

We start by taking the curl of the Maxwell equation

$$\nabla \times \mathbf{H} = \mathbf{J} + \epsilon_0 \frac{\partial \mathbf{E}}{\partial t} \qquad (A.2)$$

we get

$$\nabla \times \nabla \times \mathbf{H} = \nabla \times \mathbf{J} + \epsilon_0 \frac{\partial}{\partial t}(\nabla \times \mathbf{E}). \qquad (A.3)$$

Using the Maxwell equation

$$\nabla \times \mathbf{E} = -\frac{\partial \mathbf{B}}{\partial t} \qquad (A.4)$$

and the vector identity

$$\nabla \times \nabla \times \mathbf{H} = \nabla(\nabla \cdot \mathbf{H}) - \nabla^2 \mathbf{H} = -\nabla^2 \mathbf{H} \qquad (A.5)$$

$(\nabla \cdot \mathbf{H} = (1/\mu_0)\nabla \cdot \mathbf{B} = 0)$ and

$$\mathbf{J} = \tilde{\sigma} \, \mathbf{E}, \qquad (A.6)$$

equation A.3 becomes

$$\nabla^2 \mathbf{H} = \mu_0 \tilde{\sigma} \frac{\partial \mathbf{H}}{\partial t} + \epsilon_0 \, \mu_0 \frac{\partial^2 \mathbf{H}}{\partial t^2}. \qquad (A.7)$$

Substituting equation A.1 into equation A.7, we have

$$\frac{\partial^2 H_z}{\partial x^2} = i\,\mu_0\,\omega\,\tilde{\sigma}\,H_z - \epsilon_0\,\mu_0\,\omega^2\,H_z \tag{A.8}$$

The second term on the RHS of equation A.8 is the well-known displacement current term and is negligible at our frequencies provided that $|\tilde{\sigma}| \gg \sim 2~(\Omega m)^{-1}$ ($\sigma_n(100K) \sim 10^6~(\Omega m)^{-1}$ for $YBa_2Cu_3O_{6.95}$). If we let

$$\frac{1}{\tilde{\lambda}^2} = i\,\mu_0\,\omega\,\tilde{\sigma}, \tag{A.9}$$

then the solution to equation A.8 (having dropped the displacement current term) can be written

$$H_z = H_0\,e^{-x/\tilde{\lambda}}. \tag{A.10}$$

The surface impedance is defined by

$$Z_s = \frac{E_0}{\int_0^\infty J_y\,dx} \tag{A.11}$$

where E_0 is the value of the tangential electric field at the surface of the material (y-direction). That the electric field and the current density are both in the y-direction can easily be seen from the Maxwell equation A.2 (after dropping the displacement current term) which can be written

$$\left(\frac{\partial H_z}{\partial x}\right)_y = J_y = \tilde{\sigma}\,E_y \tag{A.12}$$

(we know that $\partial H_z/\partial y$ is zero by symmetry). By integrating equation A.12 we can also get that

$$\int_0^\infty J_y\,dx = H_z\,|_{x=0} = H_0 \tag{A.13}$$

and so equation A.11 can be written

$$Z_s = \frac{E_0}{H_0} \tag{A.14}$$

We can express E_0 in terms of H_0 using the Maxwell equation A.4 which, with our boundary conditions, becomes

$$\frac{\partial E_y}{\partial x} = -\mu_0 \frac{\partial H_z}{\partial t}. \tag{A.15}$$

Integrating this equation and setting $x = 0$ to give the fields at the surface, we find

$$E_0 = i \, \mu_0 \, \omega \, \tilde{\lambda} \, H_0 \tag{A.16}$$

and so the surface impedance can be written

$$Z_s = \frac{E_0}{H_0} = i \, \mu_0 \, \omega \, \tilde{\lambda}. \tag{A.17}$$

Since $\tilde{\lambda}$ is related to $\tilde{\sigma}$ by equation A.9, the surface impedance can be written in terms of the complex conductivity as

$$Z_s = \left(\frac{i \, \mu_0 \, \omega}{\tilde{\sigma}} \right)^{1/2}. \tag{A.18}$$

The surface impedance is often written

$$Z_s = R_s + i \, X_s \tag{A.19}$$

where the real and imaginary parts are referred to as the surface resistance and surface reactance respectively. To get a better feeling for R_s we can calculate the power dissipated per unit area of the surface. This is given simply by the magnitude of the time averaged Poynting vector

$$|\mathbf{S_{av}}| = \frac{1}{2} \, |\text{Re} \, (\mathbf{E} \times \mathbf{H}^*)| \tag{A.20}$$

evaluated at the surface ($x = 0$). Substituting for $\mathbf{E}$ and $\mathbf{H}$ in equation A.20 using equation A.14 gives

$$S_{av} = \frac{1}{2} \text{Re} \, (E_0 \, H_0^*) = \frac{1}{2} \text{Re} \, (Z_s \, H_0 \, H_0*) = \frac{1}{2} \, (\text{Re} \, Z_s) \, |H_0|^2 = \frac{1}{2} \, R_s \, |H_0|^2. \tag{A.21}$$

Thus the power per unit area dissipated is proportional to the surface resistance.

We conclude this appendix by deriving the expressions for the surface resistance of a normal metal and a superconductor (for the case of local electrodynamics).

In a normal metal the conductivity is purely real and given by $\tilde{\sigma} = \sigma_n$ where σ_n is the usual conductivity of a metal and $\rho_n = 1/\sigma_n$ is the resistivity. Substituting for $\tilde{\sigma}$ in equation A.18 gives

$$Z_s = \left(i\,\mu_0\,\rho_n\,\omega\right)^{1/2} = (1+i)\left(\frac{\mu_0\,\rho_n\,\omega}{2}\right)^{1/2} \tag{A.22}$$

and so the surface resistance for a normal metal is

$$R_s = \left(\frac{\mu_0\,\rho_n\,\omega}{2}\right)^{1/2}. \tag{A.23}$$

By substituting $\tilde{\sigma} = \sigma_n$ into equation A.9, we find

$$\frac{1}{\tilde{\lambda}} = \frac{1+i}{\delta_n} \tag{A.24}$$

where

$$\delta_n = \left(\frac{2}{\mu_0\,\sigma_n\,\omega}\right)^{1/2}. \tag{A.25}$$

From equation A.10, we can see that this is the characteristic decay length for the **H** field in the metal. Equation A.25 is, of course, the familiar expression for the skin depth in a metal.

In a superconductor, the total current density has both a normal and a superfluid component

$$\mathbf{J} = \mathbf{J}_n + \mathbf{J}_s. \tag{A.26}$$

The normal component is given by

$$\mathbf{J}_n = \sigma_1\,\mathbf{E} \tag{A.27}$$

where σ_1 is the conductivity of the normal fluid. The superfluid component is determined by the first London equation

$$\mathbf{E} = \mu_0\,\lambda_L^2\,\mathbf{J}_s \tag{A.28}$$

which gives (assuming an $e^{i\omega t}$ time dependence for the supercurrent)

$$\mathbf{J}_s = -i\,\sigma_2\,\mathbf{E} \quad ; \quad \sigma_2 = \frac{1}{\mu_0\,\omega\,\lambda_L^2} \; . \tag{A.29}$$

Therefore the total conductivity is complex and given by

$$\tilde{\sigma} = \sigma_1 - i\,\sigma_2 = \sigma_1 - \frac{i}{\mu_0\,\omega\,\lambda_L^2} \; . \tag{A.30}$$

To calculate the surface resistance for a superconductor, we substitute equation A.30 into equation A.18 and take the real part. Except very close to the transition temperature, $\sigma_1/\sigma_2 \ll 1$, and so we do the calculation to first order in σ_1/σ_2. Equation A.18 then becomes

$$Z_s = \left(\frac{\mu_0\,\omega}{\sigma_2}\right)^{1/2} \left(-1 + i\,\frac{\sigma_1}{\sigma_2}\right)^{1/2} \; . \tag{A.31}$$

To take the real part we use the identity

$$\mathrm{Re}\,(A + i\,B) = \frac{1}{\sqrt{2}} \left(\sqrt{A^2 + B^2} + A\right)^{1/2} \; . \tag{A.32}$$

The real part of equation A.31 is then

$$R_s = \left(\frac{\mu_0\,\omega}{2\,\sigma_2}\right)^{1/2} \left(-1 + \sqrt{1 + \frac{\sigma_1^2}{\sigma_2^2}}\right)^{1/2} \; . \tag{A.33}$$

Expanding the square root to first order and substituting for σ_2 we finally get the approximate form valid for $\sigma_1 \ll \sigma_2$,

$$R_s = \frac{1}{2}\,\mu_0^2\,\sigma_1\,\omega^2\,\lambda_L^3 \; . \tag{A.34}$$

Similarly, we find that the surface reactance for a superconductor is given by

$$X_s = \mu_0\,\omega\,\lambda_L \tag{A.35}$$

in the limit $\sigma_1 \ll \sigma_2$.

Appendix B

Rf Current Distribution in Samples

We wish to find the current distribution in a thin, plate-like, metallic or superconducting sample in an rf magnetic field applied perpendicular to its broad face in the limit that the skin depth or penetration depth is much less than the thickness. A sample of this shape with thickness $2c$ can be well approximated by an oblate spheroid with $a \sim b \gg c$ where a, b and c are the lengths of the semi-axes. The rf current distribution in such an ellipsoid can be determined by analogy with the magnetostatic problem of a perfectly diamagnetic ellipsoid in a uniform magnetic field, $\mathbf{H_{ext}}$, applied parallel to its minor axis (of length $2c$). The boundary conditions for the two situations are approximately the same: for the magnetostatic case, the magnetic field inside the sample, $\mathbf{B}_{int}$, is zero everywhere, and for the rf case, $\mathbf{B}_{int}$ is zero except in a thin layer (characterized by either the skin depth or the penetration depth) near the surface. Thus, in the magnetostatic case,

$$\mathbf{B}_{int} = k_m \, \mu_0 \, \mathbf{H_{int}} = 0 \qquad (B.1)$$

because $k_m = 0$ for a perfect diamagnet. For the internal $\mathbf{H}$ field, we have

$$\mathbf{H_{int}} = \frac{\mathbf{H_{ext}}}{1 + (k_m - 1) \, N} = \frac{\mathbf{H_{ext}}}{1 - N} \qquad (B.2)$$

where N is the demagnetizing factor. Therefore, the internal magnetization $\mathbf{M_{int}}$ is

$$\mathbf{M_{int}} = \frac{B_i}{\mu_0} - \mathbf{H_{int}} = -\frac{\mathbf{H_{ext}}}{1 - N} \, , \qquad (B.3)$$
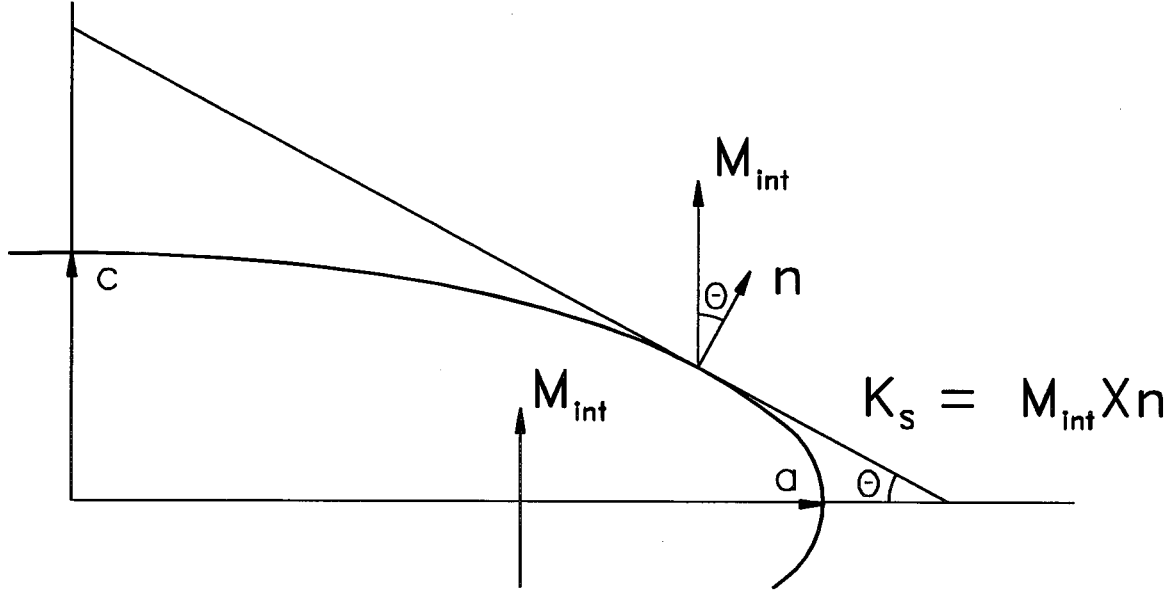
147

Figure B.1: Surface current distribution in uniformly magnetized ellipsoid.

i.e. $\mathbf{M_{int}}$ is uniform and everywhere antiparallel to $\mathbf{H_{ext}}$. The surface current density, $\mathbf{K_s}$ (current per unit length perpendicular to the direction of flow) is given by

$$\mathbf{K_s} = \mathbf{M_{int}} \times \hat{n} = M_{int}\sin\theta \qquad (B.4)$$

where $\hat{n}$ is a unit vector perpendicular to the surface, see figure B.1. It is clear from the diagram that the surface current runs in concentric rings centred about the minor axis (of length $2c$) of the ellipsoid. The sample used for the measurements described in this thesis corresponds to a ratio $a/c \sim 150$; therefore, for a sample of this shape most of the current runs very close to the edges of the crystal where $\sin\theta \sim 1$. Thus, we have determined the corresponding rf current distribution for a metal or a superconductor and also, therefore, for a superconductor in the mixed state. The latter is threaded by a vortex lattice, but to the rf fields these are just regions where the material looks more like a normal metal as opposed to a superconductor – the macroscopic current distribution is virtually unchanged.

To summarize, then, an rf H field applied parallel to the c-axis of a $YBa_2Cu_3O_{6.95}$ single crystal (in the normal, superconducting or mixed state) will induce only a–b plane screening currents that run mostly near the edges of the crystal.

Bibliography

[1] Y.B. Kim, C.F. Hempstead, and A.R. Strnad. Flux-flow resistance in type-II super-conductors. *Phys. Rev.*, **139**(4A):A1163, (1965).

[2] W.F. Vinen and A.C. Warren. Flux flow resistivity in type II superconductors I. experimental results. *Proc. Phys. Soc.*, **91**:399, (1967).

[3] N. Ya. Fogel. Temperature dependence of the viscosity coefficient in type-II super-conductors. *Sov. Phys. JETP*, **36**(4):725, (1973).

[4] Jonathan I. Gittleman and Bruce Rosenblum. Radio-frequency resistance in the mixed state for subcritical currents. *Phys. Rev. Lett.*, **16**(17):734, (1966).

[5] Jonathan I. Gittleman and Bruce Rosenblum. The pinning potential and high-frequency studies of type-II superconductors. *J. Appl. Phys.*, **39**(6):2617, (1968).

[6] J. le G. Gilchrist. Microwave surface resistance of type-II superconductors. *Proc. R. Soc. A*, **295**:399, (1966).

[7] J. le G. Gilchrist and P. Monceau. The pinning frequency of type-II superconductors. *Phil. Mag.*, **18**:237, (1968).

[8] J. le G. Gilchrist and P. Monceau. Flux flow resistivity by surface resistance measurements. *J. Phys. C: Solid St. Phys.*, **3**:1399, (1970).

[9] John Bardeen and M.J. Stephen. Theory of the motion of vortices in superconductors. *Phys. Rev.*, **140**(4A):A1197, (1965).

[10] Christiane Caroli and Kazumi Maki. Fluctuations of the order parameter in type-II superconductors. I. dirty limit. *Phys. Rev.*, **159**(2):306, (1967).

[11] Christiane Caroli and Kazumi Maki. Fluctuations of the order parameter in type-II superconductors. II. pure limit. *Phys. Rev.*, **159**(2):316, (1967).

[12] Christiane Caroli and Kazumi Maki. Motion of the vortex structure in type-II superconductors in high magnetic field. *Phys. Rev.*, **164**(2):591, (1967).

[13] Kazumi Maki. Resistive states in type-II superconductors. *Phys. Rev.*, **169**(2):381, (1968).

[14] Chia-Ren Hu and Richard S. Thompson. Dynamic structure of vortices in superconductors. II. $H \ll H_{c_2}$. *Phys. Rev. B*, **6**(1):110, (1972).

[15] L.P. Gor'kov and N.B. Kopnin. Vortex motion and resistivity of type-II superconductors in a magnetic field. *Sov. Phys.-Usp.*, **18**(7):496, (1976).

[16] L.P. Gor'kov and N.B. Kopnin. Viscous flow of vortices in type-II superconducting alloys. *Sov. Phys. JETP*, **38**(1):195, (1974).

[17] D.J. Baar. Private communication.

[18] D.A. Bonn, P. Dosanjh, Ruixing Liang, and W.N. Hardy. Evidence for rapid suppression of quasiparticle scattering below T_c in $YBa_2Cu_3O_{7-\delta}$. *Phys. Rev. Lett.*, **68**:2390, (1992).

[19] D.A. Bonn, Ruixing Liang, T.M. Riseman, D.J. Baar, D.C. Morgan, Kuan Zhang, P. Dosanjh, T.L. Duty, A. MacFarlane, G.D. Morris, J.H. Brewer, W.N. Hardy, C. Kallin, and A.J. Berlinsky. Microwave determination of the quasiparticle scattering time in $YBa_2Cu_3O_{6.95}$. *Phys. Rev. B*, **47**:11314, (1993).

[20] P. Nozières and W.F. Vinen. The motion of flux lines in type II superconductors. *Phil. Mag.*, **14**:408, (1966).

[21] C. Caroli, P.G. De Gennes, and J. Matricon. Bound fermion states on a vortex line in a typeII superconductor. *Phys. Lett.*, **9**(4):307, (1964).

[22] Theodore C. Hsu. Absence of dipole transitions in vortices of type II superconductors. *Phys. Rev. B*, **46**(6):3680, (1992).

[23] Theodore C. Hsu. Frequency dependent conductivity of vortex cores in type II superconductors. *Physica C*, **213**:305, (1993).

[24] Catherine Kallin and A. John Berlinsky. Are the high-T_c superconductors d-wave? In *Proceedings of the μSR-93 conference in Maui*, (1993).

[25] Milind N. Kunchur, David K. Christen, and Julia M. Phillips. Observation of free flux flow at high dissipation levels in $YBa_2Cu_3O_{7-\delta}$ epitaxial films. *Phys. Rev. Lett.*, **70**(7):998, (1993).

[26] U. Welp, W.K. Kwok, G.W. Crabtree, K.G. Vandervoort, and J.Z. Liu. Magnetic measurements of the upper critical field of $YBa_2Cu_3O_{7-\delta}$ single crystals. *Phys. Rev. Lett.*, **62**(16):1908, (1989).

[27] T.T.M. Palstra, B. Batlogg, R.B. van Dover, L.F. Schneemeyer, and J.V. Waszczak. Dissipative flux motion in high-temperature superconductors. *Phys. Rev. B*, **41**(10):6621, (1990).

[28] Mark W. Coffey and John R. Clem. Unified theory of effects of vortex pinning and flux creep upon the rf surface impedance of type-II superconductors. *Phys. Rev. Lett.*, **67**(3):386, (1991).

[29] Mark W. Coffey and John R. Clem. Theory of rf magnetic permeability of type-II superconductors in slab geometry with an oblique applied static magnetic field. *Phys. Rev. B*, **45**(18):10527, (1992).

[30] Ruixing Liang, P. Dosanjh, D.A. Bonn, D.J. Baar, J.F. Carolan, and W.N. Hardy. *Physica C*, **195**:51, (1992).

[31] Alain Junod. Specific heat of high temperature superconductors: A review. In Donald M. Ginsberg, editor, *Physical Properties of High Temperature Superconductors II*, page 13. World Scientific, 1990.

[32] N.R. Werthamer, E. Helfand, and P.C. Hohenberg. Temperature and purity dependence of the superconducting critical field, H_{c_2} . III. electron spin and spin-orbit effects. *Phys. Rev.*, **147**(1):295, (1966).

[33] E. Helfand and N.R. Werthamer. Temperature and purity dependence of the superconducting critical field, H_{c_2} . II. *Phys. Rev.*, **147**(1):288, (1966).

[34] Michael Tinkham. *Introduction to Superconductivity*. McGraw-Hill, 1st edition, 1975.

[35] J.M. Pond, K.R. Carroll, J.S. Horowitz, D.B. Chrisey, M.S. Osofsky, and V.C. Cestone. *Appl. Phys. Lett.*, **59**:3033, (1991).

[36] D.N. Basov, A.V. Puchkov, T. Strach, T. Timusk, D.A. Bonn, Ruixing Liang, and W.N. Hardy. *submitted to Phys. Rev. Lett.*

[37] A. Umezawa, G.W. Crabtree, J.Z. Liu, T.J. Moran, S.K. Malik, L.H. Nunez, W.L. Kwok, and C.H. Sowers. *Phys. Rev. B*, **38**:2843, (1988).

[38] Ruixing Liang, P. Dosanjh, D.A. Bonn, and W.N. Hardy. Lower critical fields in an ellipsoidal-shaped $YBa_2Cu_3O_{6.95}$ single crystal. *submitted to Phys. Rev. Lett.*

[39] D.A. Bonn. Private communication.

[40] W.N. Hardy, D.A. Bonn, D.C. Morgan, Ruixing Liang, and Kuan Zhang. Precision measurements of the temperature dependence of λ in $YBa_2Cu_3O_{6.95}$: Strong evidence for nodes in the gap function. *Phys. Rev. Lett.*, **70**(25):3999, (1993).

[41] P.W. Anderson. Theory of flux creep in hard superconductors. *Phys. Rev. Lett.*, **9**(7):309, (1962).

[42] Y.B. Kim, C.F. Hempstead, and A.R. Strnad. Flux creep in hard superconductors. *Phys. Rev.*, **131**(6):2486, (1963).

[43] P.L. Gammel, L.F.Schneemeyer, J.V. Waszczak, and D.J. Bishop. Evidence from mechanical measurements for flux-lattice melting in single-crystal $YBa_2Cu_3O_7$ and $Bi_{2.2}Sr_2Ca_{0.8}Cu_2O_8$. *Phys. Rev. Lett.*, **61**(14):1666, (1988).

[44] David R. Nelson and H. Sebastion Seung. Theory of melted flux liquids. *Phys. Rev. B*, **39**(13):9153, (1989).

[45] U. Welp, S. Fleshler, W.K. Kwok, R.A. Klemm, V.M. Vinokur, J. Downey, B. Veal, and G.W. Crabtree. High-field scaling behaviour of thermodynamic and transport quantities of $YBa_2Cu_3O_{7-\delta}$ near the superconducting transition. *Phys. Rev. Lett.*, **67**(22):3180, (1991).

[46] M. Tinkham. Viscous flow of flux in type-II superconductors. *Phys. Rev. Lett.*, **13**(26):804, (1964).

[47] R.G. Jones, E.H. Rhoderick, and A.C. Rose-Innes. On the origin of resistance in the mixed state of type-II superconductors. *Phys. Lett.*, **15**(3):214, (1965).

[48] B.D. Josephson. Potential difference in the mixed state of type II superconductors. *Phys. Lett.*, **16**(3):242, (1965).

[49] Wolfgang K.H. Panofsky and Melba Phillips. *Classical Electricity and Magnetism.* Addison-Wesley Publishing Company, Inc., 2nd edition, 1962.

[50] P.G. de Gennes and J. Matricon. *Rev. Mod. Phys.*, **36**:45, (1964).

[51] P.H. Borcherds, C.E. Gough, W.F. Vinen, and A.C. Warren. *Phil. Mag.*, **10**:349, (1964).

[52] John Bardeen. Motion of quantized flux lines in superconductors. *Phys. Rev. Lett.*, **13**(25):747, (1964).

[53] V.M. Vinokur, V.B. Geshkenbein, M.V. Feigel'man, and G. Blatter. Scaling of the hall resistivity in high-t_c superconductors. *Phys. Rev. Lett.*, **71**(8):1242, (1993).

[54] John R. Clem. Local temperature-gradient contribution to flux-flow viscosity in superconductors. *Phys. Rev. Lett.*, **20**(14):735, (1968).

[55] P.B. Miller. *Phys. Rev.*, **121**:445, (1961).

[56] L.P. Gor'kov and G.M. Eliashberg. *Sov. Phys. JETP*, **27**:328, (1968).

[57] A. Schmid. *Phys. Kondens. Mat.*, **5**:302, (1968).

[58] H. Suhl. Inertial mass of a moving fluxoid. *Phys. Rev. Lett.*, **14**(7):226, (1965).

[59] Ernst Helmut Brandt. Penetration of magnetic ac fields into type-II superconductors. *Phys. Rev. Lett.*, **67**(16):2219, (1991).

[60] Mark W. Coffey and John R. Clem. Vortex inertial mass for a discrete type-II superconductor. *Phys. Rev. B*, **44**(13):6903, (1991).

[61] Mark W. Coffey and Zhidong Hao. Dipolar electric field induced by a vortex moving in an anisotropic superconductor. *Phys. Rev. B*, **44**(10):5230, (1991).

[62] J. Owliaei, S. Sridhar, and J. Talvacchio. Field-dependent crossover in the vortex response at microwave frequencies in $YBa_2Cu_3O_{7-\delta}$ films. *Phys. Rev. Lett.*, **69**(23):3366, (1992).

[63] R. Marcon, R. Fastampa, M. Guira, and E. Silva. Vortex-motion dissipation in high-T_c superconductors at microwave frequencies. *Phys. Rev. B*, **43**(4):2940, (1991).

[64] Hui Wu, N.P. Ong, and Y.Q. Li. Frequency dependence of the vortex–state resistivity in $YBa_2Cu_3O_{7-\delta}$. *Phys. Rev. Lett.*, **71**(16):2642, (1993).

[65] R.H. Koch, V. Foglietti, W.J. Gallagher, G. Koren, A. Gupta, and M.P.A. Fisher. *Phys. Rev. Lett.*, **63**:1511, (1989).

[66] P.L. Gammel, L.F. Schneemeyer, and D.J. Bishop. *Phys. Rev. Lett.*, **66**:953, (1993).

[67] M.P.A. Fisher. *Phys. Rev. Lett.*, **62**:1415, (1989).

[68] Daniel S. Fisher, Matthew P.A. Fisher, and David A. Huse. *Phys. Rev. B*, **43**:130, (1991).

[69] W.N. Hardy and L.A. Whitehead. Split-ring resonator for use in magnetic resonance from 200–2000 MHz. *Rev. Sci. Instrum.*, **52**(2):213, (1981).

[70] D.A. Bonn, D.C. Morgan, and W.N. Hardy. Split-ring resonators for measuring microwave surface resistance of oxide superconductors. *Rev. Sci. Instrum.*, **62**(7):1819, (1991).

[71] David G. Blair, HoJung Paik, and Robert C. Taber. How to make high critical current joints in nb-ti wire. *Rev. Sci. Instrum.*, **46**(8):1130, (1975).

[72] Kuan Zhang, W.N. Hardy, and S. Kamal. Private communication.

[73] N. Miura. Solid state research in megagauss fields. *Physica B*, **164**(1):97, (1990).

[74] M. Date. Advances in high field magnetism. *Physica B*, **164**(1):108, (1990).

[75] N.-C. Yeh. High-frequency vortex dynamics and dissipation of high-temperature superconductors. *Phys. Rev. B*, **43**(1):523, (1991).